Dissertation der Graduate School of Systemic Neurosciences
der Ludwig-Maximilians-Universität München

Graduate School of
Systemic Neurosciences
LMU Munich

Comparative cortical connectomics: three-layered cortex in mouse and turtle

Philipp Alexander Bastians

supervised by Prof. Moritz Helmstaedter
at the Max Planck Institute for Brain Research

März 26, 2018

Supervisor:	**Prof. Moritz Helmstaedter**
Second reviewer:	**Prof. Ilona Grunwald Kadow**
Third reviewer:	**Prof. Zoltan Molnar**
Date of oral defense:	**27.09.2018**

Contents

Acronyms

2P two photon microscopy. 36

AIS axon initial segment. 39, 57, 59–61, 72, 73, 75, 76, 80–82, 98

ATUM automated tape collecting ultra microtome. 30–32

CCD charge-coupled device. 29

CCK cholecystokinin. 26

ChaT choline acetyltransferase. 26

DVR dorsal ventricular ridge. 14

EM electron microscopy. 27, 29, 31–33, 36, 41, 48, 50, 52, 54–56, 71, 86, 93, 101, 103, 104

ExM expansion microscopy. 36

FIBSEM focused ion beam scanning electron microscope. 30, 33

fMRI functional magnetic resonance imaging. 28, 37

IN interneuron. 18, 22–24, 93, 94, 96–98

IQR interquartile range. 53

LGN lateral geniculate nucleus. 22, 91

LOT lateral olfactory tract. 17–19, 25

MEC medial entorhinal cortex. 95

MPCtx mouse piriform cortex. 16, 18, 23, 41, 54, 57, 58, 60–62, 67, 93

MRI magnetic resonance imaging. 37

mSEM multi-beam scanning electron microscope. 32

NPY neuropeptide Y. 26

OB olfactory bulb. 17, 19, 100

PALM photo-activated localization microscopy. 28

PC pyramidal cell. 18, 21–25, 55–57, 81, 86, 95–98

PCtx piriform cortex. 16–19, 22, 95, 97

PLASS path-length-dependent axonal synapse sorting. 4, 95

rfMRI resting-state fMRI. 37

RT room temperature. 43, 44

SBEM serial block-face electron microscopy. 32, 33, 44, 45, 47, 51, 55, 56, 60, 83, 85, 94, 104–106, 136

SD standard deviation. 58, 63, 66–68, 70–73, 76, 78, 81, 86, 89, 93, 98

SEM scanning electron microscope. 30–32, 53, 55, 56, 75, 82

SL semilunar. 18, 24, 25, 80–82, 97, 98

SP substance P. 26

SST somatostatin. 26

ssTEM serial section transmission electron microscope. 29, 83, 86, 87, 106

STED stimulated emission depletion microscopy. 28

STORM stochastic optical reconstruction microscopy. 28

STP serial two photon tomography. 36

TDCtx turtle dorsal cortex. 16, 19, 21–23, 41, 54, 57, 60, 61, 63, 64, 71

TEM transmission electron microscope. 29–31, 49, 84, 86, 106, 136, 137

TEMCA transmission electron microscopy camera array. 29–31

VIP vasoactive intestinal peptide. 26

1 Summary

Understanding the mammalian brain mechanistically is one of the most fundamental challenges in neuroscience. To this end, one approach is to study species which are expected to possess similar but less complex brains and thereby making it easier to decipher its functional implementation. This insight can then be compared to evolutionary younger and probably more advanced nervous systems and may also reveal how brain structures and neural circuits evolved.

One of the hallmarks of highly developed neural systems are layered cerebral cortices. They developed over 320 million years ago in amniotes and are maintained until today in reptilians and mammals. Studies [Fournier et al., 2015] suggest that the underlying circuits may be similar partially due to functional features observed in cortices of both classes, e.g. feedforward and feedback inhibition. Therefore, the identification of the structural and functional similarities between the mammalian piriform and reptilian dorsal cortex may further help to reveal common organizational and computational principles. However, the underlying neuronal circuit connectivity has not been studied in detail partly due to technical challenges.

In this work, three-dimensional serial block-face scanning electron microscopy was used to study the local inhibitory connectomes of the three-layered turtle dorsal and mouse piriform cortex. A total of four nanoliter scale datasets were acquired at a resolution high enough to identify single synapses; one dataset from each layer in the turtle dorsal

cortex and one taken from layer 2 of the mouse piriform cortex. A total axonal path length of 134 mm was reconstructed and more than 10.000 synapses were annotated.

Axons in the mouse piriform cortex showed specific innervation of cell bodies, axon initial segments, dendritic spine heads, and shafts. The axons in the turtle dorsal cortex, however, were found to show none of these highly specific innervations. Instead, postsynaptic structures were innervated with no apparant preference. Furthermore, boutons of turtle cortical axons were frequently observed to enwrap dendritic spines completely similar to mossy fibers in the mammalian hippocampus and axons of retinal ganglion cells in the mammalian thalamus.

Structurally similar boutons are not found in the isocortex and might be lost during its evolutionary development. However, they are still present in the mammalian hippocampus, an evolutionarily ancient brain region. Furthermore, the data indicates that the cortical subcellular-specific inhibitory wiring is a unique feature of mammalian cortices and may have been developed after the evolutionary deviation from reptiles. This work suggests that despite the similarities in structure and function of three-layered cortices, the innervation mechanism at the subcellular level can be substantially different between species.

2 Introduction

The brain is controlling all functions in a vertebrate's body and is considered to be the most complex organ. In humans, the brain contains approximately 86 billion neurons. Each neuron is connected by synapses to several thousand other neurons [Herculano-Houzel, 2009]. One function of the brain is create a cognitive image of the environment, which is based on the sum of all sensory signals sent to the brain. The brain processes the sensory signals, selects the relevant pieces of information and utilizes that information to generate behavioral responses which enable living beings to interact with the world. The outer and evolutionary youngest part of the brain, the cerebral cortex, constitutes about 82% of the brain's mass in humans [Herculano-Houzel, 2009]. It is involved in both sensory processing as well as behavioral responses but we are still far from understanding how the majority of the processing is done. One approach to increase our knowledge about the cerebral cortex is provided by the field of comparative biology which is fundamentally based on the theory of evolution indicating the gradual change of species which gave rise to the vast diversity of living animals [Hall et al., 2008]. This comparative approach is summarized by observing a variety of species, classifying the individual findings and use this data to formulate general principles [Nelson, 1970].

2.1 Comparative neurobiology

The primary goal of comparative neurobiology is to gain knowledge about the structure, the function, and the evolution of nervous systems by studying a variety of species focusing on differences and similarities [Bullock, 1984]. The basic knowledge about the nervous system was derived by researching species like lampreys (cellular basis of motor behavior reviewed by [Grillner, 2003]), crabs and lobsters (cellular and circuit mechanisms generating rhythmic motor patterns reviewed by [Marder and Bucher, 2007]) and marine mollusks (reflex circuits reported by [Frost et al., 1985]) which represent an inset of examples. Using a wide biological diversity is an attempt to find model systems of the brain that are simpler and/or more accessible for studying and dissecting neural circuits [Hale, 2014]. Another motivation for using a diversity of model systems is an important feature of comparative biology in general and best described with Krogh's principle, which suggests that for any question in biology there exists a specialized animal ideally suited for the experimental discovery of the answer [Krogh, 1929]. Barn owls, for instance, possess superb hunting abilities using auditory cues and are being used as a model system to identify a neural mechanism which calculates the location of prey with auditory delay lines [Jeffress, 1948]. In hindsight, it seems unlikely that such a discovery would have been made without the barn owl (reviewed by [Ashida and Carr, 2011] and [Grothe et al., 2010]). These findings suggest that certain animals are better candidates than others for understanding the implementation principles based on their superb specializations. These principles may then be used as a template for comparing or predicting the underlying neuronal implementation across species. Continuing the barn owl example, sound localization is also studied extensively in mammals and studies comparing both systems indicate that the neural implementation might be rather different in mammals missing the systemic arrangement of axon conduction delays which are crucial in the barn owl auditory system

[McAlpine and Grothe, 2003]. The visual system of mice and flies is another comparative example reviewed by [Borst and Helmstaedter, 2015]. Although, their visual organs are structurally different (e.g. facette eye vs. lens eye), there are similarities in the functional processing of visual stimuli (e.g. splitting, parallel processing and consecutively merging of visual ON- and OFF-streams [Masu et al., 1995] and [Joesch et al., 2010]). Comparative findings build a fundament for discussions about how natural evolution found similar and dissimilar solutions implemented by neural circuit structures and functions. In addition, the evolutionary history of species may be used to find similarities which are more likely when two species share a common ancestor [Northcutt, 1981]. This was observed for example in studies investigating the auditory sound localization of chicks sharing the same implementation mechanisms like owls although the cranial challenges are more comparable to rodents [Köppl and Carr, 2008]. Discoveries in non-mammalian animals about neural structures, mechanisms and patterns of activity shape our knowledge of mammals and humans [Hildebrand and Shepherd, 1997].

2.1.1 Reptiles and mammals

The typical characteristics found in the reptilian class, e.g. ectothermic body temperature, epidermal scales and egg-laying reproduction, separates them from mammals. The reptilian class is not a monophyletic group since birds are direct descendants of the dinosaurs and belong evolutionarily to the reptiles. Together birds and nonavian reptiles form a group called the sauropsids. Here, the focus is on nonavian reptiles which from this point on are called 'reptiles'.

Reptiles and mammals are both amniotes and they share a common ancestor (see Figure 2.1). The mammalian evolution deviated from reptiles 320-340 million years ago [Naumann and Laurent, 2017] and the mammalian brain is considered to be more sophisticated but little is known how brains evolved from their common origin.

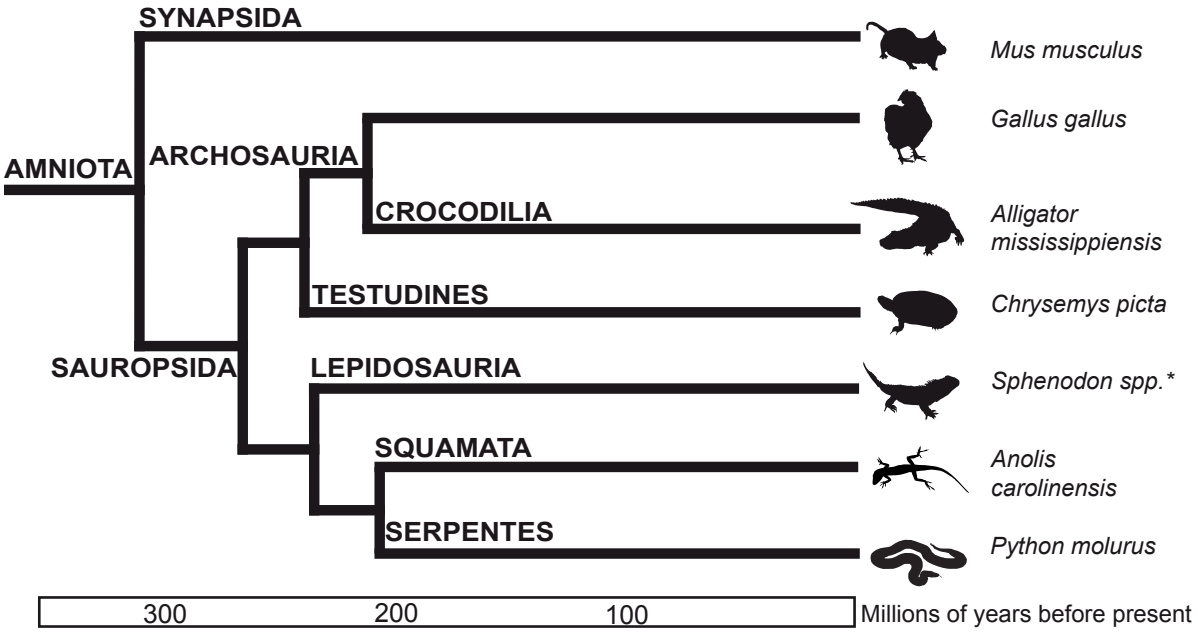

Fig. 2.1: **Simplified evolutionary filiations of amniotes.**
The amniote phylogeny which was derived using complete genome sequences. For each model organism on the right, there is a complete genome available. The names of important vertebrate groups are given at the nodes in the phylogeny (e.g. Synapsida, Sauropsida, and Archosauria). The only extant lineage of the Synapsida is the mammals. *Currently, there is no complete genome available for Sphenodon.
Figure modified from [Tollis et al., 2015] with permission.

Since brains degrade long before an animal is fossilized, research focuses on investigating contemporary related species to derive characteristics that might have been shared by their common ancestor. Turtles represent a subgroup of reptiles and they are considered to have changed little since the Triassic (200 - 250 million years ago) [Naumann and Laurent, 2017].

Phylogeny of turtles

In the amniote phylogeny derived by genome sequencing, turtles (order Testudines) are placed as a sister group of Archosauria which includes Crocodilia and Birds [Tollis et al., 2015]. Turtles evolved to its modern form in the Triassic (200 - 250 MY ago) which is based on anatomically characteristics like the shell [Li et al., 2008]. Besides their unique body plan, turtles do not possess any temporal opening at their skull, whereas most reptiles and mammals possess temporal openings (synapsid and diapsid conditions which refers to one and two temporal openings respectively) [Naumann and Laurent, 2017]. With respect to the brain, the innervation and organization of the cerebral cortex likely emerged early in the evolution of amniotes and deviated substantially during the evolutionary development of extant mammals and reptiles.

2.2 Pallium

In the field of comparative neurobiology, one of the most compelling question is how the mammalian cerebral cortex evolved [Butler, 1994]. One important step towards answering this question is to identify the affiliation of the cerebral cortex within the vertebrate brain structures. The telencephalon belongs to the rostral-most part of the forebrain and is further divided into the pallium (mantle) and the subpallium which contains the basal ganglia, the preoptic area, and parts of septum and amygdala. In

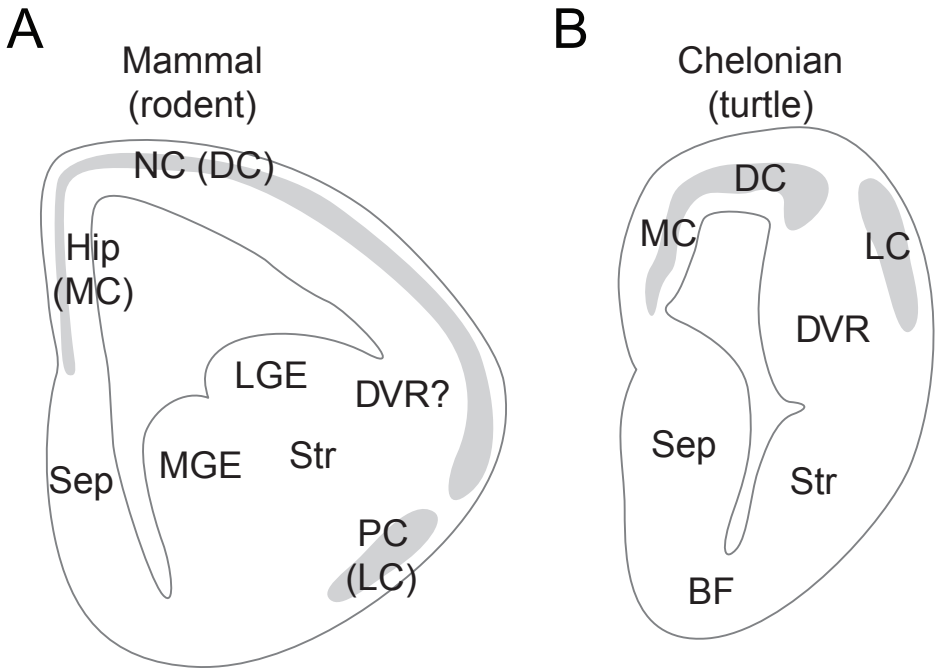

Fig. 2.2: **Simplified cerebral cortex organization in mammals and chelonians.** Sketch of the dorsal embryonic telencephalon (frontal sections) shows the organization of the brain in **(A)** mammals and **(B)** chelonians. Abbreviations: BF = basal forebrain; DC = dorsal cortex; DVR = dorsal ventricular ridge; Hip = hippocampus; LC = lateral cortex; LGE = lateral ganglionic eminence; MC = medial cortex; MGE = medial ganglionic eminence; NC = neocortex; Rh = rhinencephalon; Sep = septal nuclei; Str = striatum; Wu = avian Wulst.
Figure modified from [Bar et al., 2000] with permission.

mammals, the pallium contains the cortex, a number of cortical nuclei, and parts of the amygdala [Puelles et al., 2013] and in reptiles it contains the dorsal cortex and the dorsal ventricular ridge (DVR), as well as olfactory, hippocampal, and pallial amygdala regions [Jarvis, 2009]. The pallium is further divided into four parts: medial, dorsal, lateral and ventral pallium (see Figure 2.2).

The ventral pallium has been characterized recently using the expression patterns of the Tbr-1 and the absence of the Emx-1 gene [Puelles et al., 2000] and this pattern exists in all vertebrates [Brox et al., 2004]. The other three parts are considered to correspond to the medial cortex (hippocampus, archicortex), the dorsal cortex (neocortex), and the lateral cortex (olfactory cortex, paleocortex) [Striedter, 2006].

The anatomical terms ‘paleopallium’, ‘archipallium’, and ‘neopallium’ indicate their supposed order of appearance in evolution. The pallium contains both nuclear and layered brain structures like in the mammalian brain and in the non-mammalian brain it more frequently contains nuclear structures exclusively, e.g. in birds or amphibians. However, the cortex is not exclusively found in mammals and was most likely already evolutionary derived in the dorsal pallial structure when sauropsids and therapsids (the mammalian precursor) deviated [Bar et al., 2000]. The functional architecture of cortex exhibits several remarkable and unique features: recurrent, excitatory, and modifiable connections with many other cortical neurons [Douglas and Martin, 2007]. These features are the fundamental principle for the enormous processing capabilities of the cerebral cortex.

2.2.1 Layered cortex

The mammalian dorsal pallium is conventionally described as a cytoarchitectural six-layered cortex [Brodmann, 1909]. The term neocortex is indicating its evolutionary novel development, which is debated especially with regard to the brain of birds [Reiner et al., 2004, Dugas-Ford and Ragsdale, 2015]. The term isocortex indicating its homogenous architecture offers a more neutral description with regard to evolution. Although, differences in lamination are observable, e.g. primate visual cortex possessing more than six layers counting the many sublayers [Balaram and Kaas, 2014], agreeing upon the six-layered scheme has been useful. Every layer contains a unique combination of excitatory and inhibitory cell types. One of the most remarkable features of the mammalian isocortex is the topographical organization of the visual, auditory and somatosensory system [Kaas, 1997]. The question how the six-layered cortex evolved is still debated, e.g. a mutation in the Reelin pathway is suggested to have had a major effect in the cortical lamination and the laminar differentiation

[Bar et al., 2000]. However, the existence of six layers is not a necessary feature of the cortex. Braitenberg's 'skeleton' cortex solely consists of a superficial layer with afferent or intracortical axons and a pyramidal cell layer [Braitenberg, 1978]. This reduction may be sufficient for the most elementary cortical computations [Larkum, 2013] and reptiles possess a three-layered cortical architecture [Ulinski, 1990]. Also the mammalian cortex possesses three-layered cortices, e.g. the hippocampus and the olfactory cortex [Fournier et al., 2015].

2.2.2 Three-layered cortex

The outer and thickest layer 1 (plexiform or molecular layer) contains mainly dendrites of principal cells, a few scattered interneurons, afferent and local axons. The cell bodies of pyramidal cells are densely packed within layer 2 (cellular layer) and their apical dendrites run radially towards the pial surface. This layer is densely packed with cell bodies and shows the most prominent feature of three-layered paleocortices. Their basal dendrites are located in layer 3 (deep plexiform or subcellular layer) besides corticofugal and local axons as well as interneurons. Only in the piriform cortex (PCtx), deep pyramidal cells are in layer 3 [Ulinski, 1990]. The choice of three layers is also a convention with exceptions, e.g. classifying subdivisions of L1 usin expression marker immunoreactivity [Regidor and Poch, 1988] or the legacy work of [Edinger and Rand, 1908] and [Ramón y Cajal, 1952]. This project compares the three-layered cortices mouse piriform cortex (MPCtx) and turtle dorsal cortex (TDCtx) which will be introduced in more detail. Noteworthy, the remarkable feature of sensory topographical organizations has not been found in any three-layered cortex.

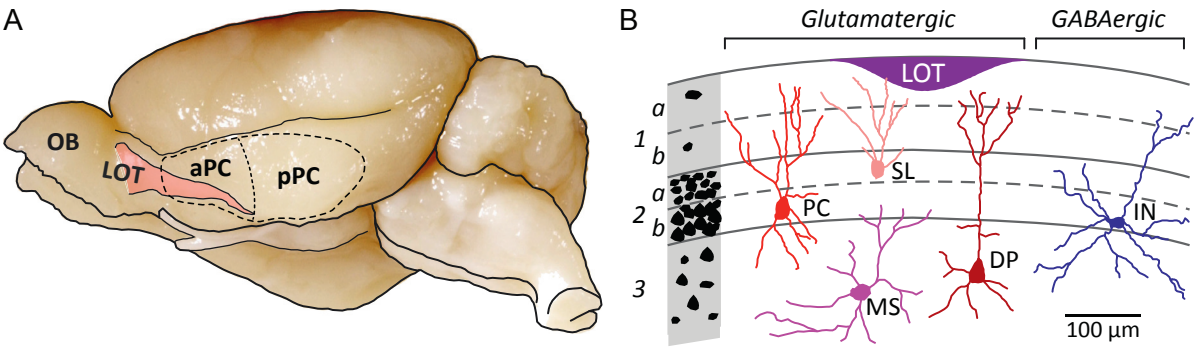

Fig. 2.3: **Location, cytoarchitecture, and circuitry of the piriform cortex.** **(A)** Lateral view of a rat brain showing the olfactory bulb (OB), lateral olfactory tract (LOT) in purple, and the approximate boundaries of the anterior (aPC) and posterior piriform cortex (pPC). **(B)** The schematic drawing shows the cytoarchitecture and basic neuronal types in a coronal slice of the aPC. The black shapes on the left represent the relative density of neuronal cell bodies in different laminae. Semilunar and superficial pyramidal cell bodies are concentrated in layers 2a and 2b, respectively. Deep pyramidal (DP) and multipolar spiny (MS) cells are found in layer 3. GABA-releasing interneurons (INs) are distributed across all layers.
Figure taken from [Bekkers and Suzuki, 2013] with permission.

Piriform cortex

The piriform cortex (PCtx) is a three-layered paleocortex, located caudally to the olfactory bulb (OB) and spans roughly 10 mm^2 [Haberly and Bower, 1989]. It is subdivided into an anterior and a posterior region (see Figure 2.3) which differ in density of afferent vs. intracortical fibers [Haberly, 2001], in properties of odor-evoked responses [Litaudon et al., 2003] and in their connectivity to downstream targets [Johnson and Leon, 2000]. Odor-evoked responses in the PCtx activate unique but scattered ensembles of cortical neurons [Stettler and Axel, 2009], which differs clearly from the topographic organization of other sensory cortices, e.g. the somatosensory cortex S1 [Brecht and Sakmann, 2002]. Layer 1a contains primarily afferent axons from the the OB, while layer 1b contains associational axons from neurons located throughout the PCtx, however this ratio of afferent to associational fibers in layer 1 decreases from anterior to posterior [Hagiwara et al., 2012]. Layer 2 contains the principal neurons

of the PCtx; glutamatergic semilunar (SL) neurons and spiny pyramidal cells (PCs). Layer 2 also contains several GABAergic interneurons, including bitufted, small and large multipolar cells [Suzuki and Bekkers, 2007]. Layer 3 consists predominantly of neuropil, containing relatively few neurons, including deep PCs and a number of interneuron (IN) types. The texture of neuronal dendrites represents a good proxy to separate PCs from INs by showing spiny and smooth dendrites, respectively [Haberly, 1983].

Excitatory cells The excitatory neurons in layer 2 comprise of semilunar (upper layer 2) and pyramidal neurons (lower layer 2) and excitatory neurons in layer 3 comprise deep pyramidal cells and scattered multipolar spiny glutamatergic neurons [Haberly, 1983]. SL neurons are located more superficially within layer 2 and lack basal dendrites while PCs are densely packed in layer 2 and have basal dendrites extending into layer 3. Both SL cells and PCs extend apical dendrites up to the pial surface where they receive synaptic input from the lateral olfactory tract (LOT) and other cells of the PCtx, and innervate downstream regions like the entorhinal and prefrontal cortices [Poo and Isaacson, 2009]. Semilunar and pyramidal cells receive different ratios of afferent to intracortical inputs and studies suggest that each cell type potentially belong to different functional sub-circuits [Poo and Isaacson, 2011].

Inhibitory cells Inhibitory cells are classified by their neurotransmitter, molecular markers, the morphology of their dendritic arbor and the distribution of their axon projections (reviewed by [Suzuki and Bekkers, 2007]. In the MPCtx, the number of IN cells constitute 10% of all neurons [Sarma et al., 2011] and subclasses of INs seem to correlate with the type of inhibition they mediate, e.g. primarily feedback or feedforward inhibition. Horizontal and neurogliaform interneurons in layer 1 receive afferent inputs from the LOT and mediate fast feedforward inhibition targeting apical dendrites of layer 2 pyramidal cells. Bitufted, fast-spiking and regular spiking interneurons

from layers 2 and 3 receive little direct afferent input from the LOT but provide strong feedback inhibition onto cell bodies and basal dendrites of pyramidal cells [Stokes and Isaacson, 2010].

Connectivity Afferents from mitral/tufted cells project to the PCtx through the LOT [Shipley and Ennis, 1996]. These afferents show a clear gradient, with the anterior PCtx receiving more afferents than the posterior PCtx [Haberly and Price, 1977]. In addition, afferent projections do not maintain the topographical relationship of the glomeruli they originated from and project dispersed across the PCtx [Sosulski et al., 2011] which indicates that the information contained in the clustering of olfactory receptor cell axons is most likely lost or differently encoded in the PCtx [Wilson and Sullivan, 2011]. However, studies claim that some fine-scale topographical mapping of OB projections is still maintained (e.g., mitral vs. tufted cell projections) [Igarashi et al., 2012]. The major projection partners are the orbitofrontal cortex, the lateral entorhinal cortex, the agranular insular cortex, the anterior olfactory nucleus, the olfactory tubercule, and the amygdala [Haberly and Price, 1978, Johnson and Leon, 2000, Ekstrand et al., 2001].

Turtle dorsal cortex

Overview Turtles also possess a three-layered paleocortex [Desan, 1984] and the cytoarchitecture is similar in comparison to the PCtx, however layer 3 is smaller and the cell density is lower. It is not uniform over the mantle and the regions are mostly defined by three criteria: neuron anatomy or marker expression, intracortical or extracortical connections, and physiological responses. In all reptiles, at least three major subdivisions are recognized: medial, dorsal, and lateral cortices [Ulinski, 1990, Naumann and Laurent, 2017]. The TDCtx is divided along the latero-medial axis into two regions D1, D2 and D3 covering the medial, intermediate and lateral part, respectively [Molowny et al., 1972] and is mainly based on cytoarchitectural features

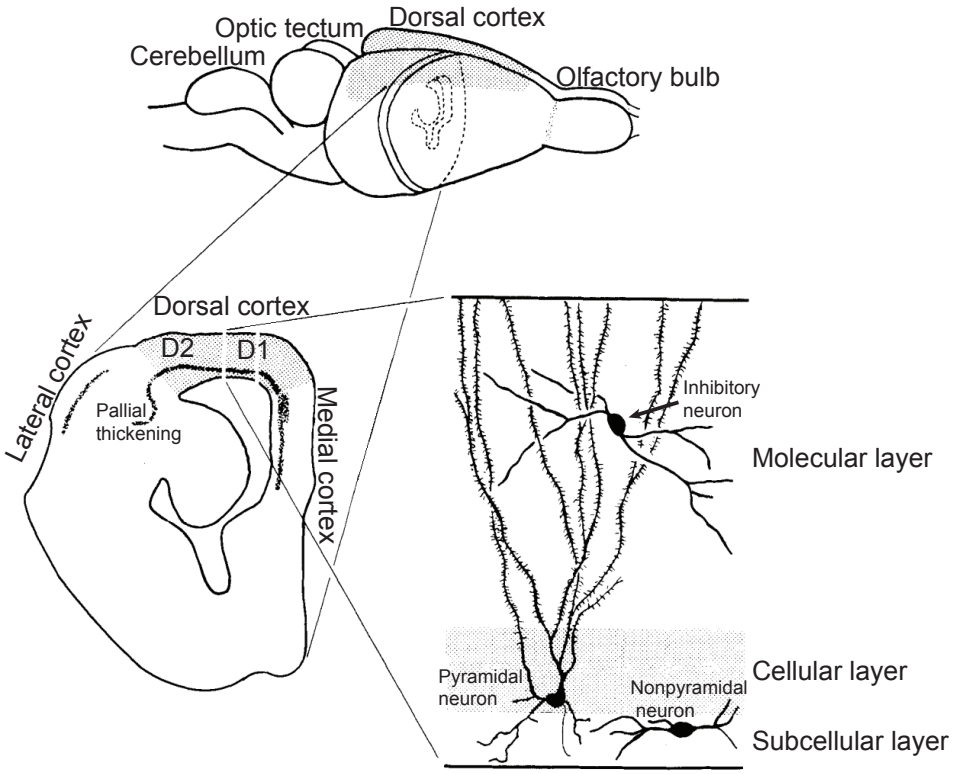

Fig. 2.4: **The turtle brain and cortex at multiple scales.**
(Top) Schematic diagram shows the lateral view of a turtle brain. The dorsal cortex (stippled) is located on the surface of the telencephalon above the lateral ventricle. **(Left)** The coronal slice is enlarged in the lower left panel. The dorsal cortex (stippled) can be subdivided into two regions (D1 and D2) by the distance of the pyramidal cell layer from the ventricle [Desan, 1984]. **(Right)** A small section of the dorsal cortex is enlarged in the lower right panel. The molecular layer lies beneath the pia and contains the apical dendrites of pyramidal cells from the layer below and scattered inhibitory nonpyramidal neurons. Below the molecular layer, the pyramidal cell layer contains the cell bodies of pyramidal neurons. The subcellular zone contains nonpyramidal neurons and basilar dendrites. Lines at the top and bottom of the lower right panel represent the pial and ependymal surface, respectively. Additional abbreviations: CB = cerebellum, OT = optic tectum, OB = olfactory bulb, MC = medial cortex.
Figure modified from [Blanton et al., 1987] with permission.

of subcellular layer 3 which is thick in D2 and thin in D1 [Desan, 1984]. However, the cortical regions are not consistently defined due to a lack of specific markers [Ulinski, 1990]. The most lateral part of the turtle dorsal cortex folds inward forming the pallial thickening [Johnston, 1915]. The pallial thickening receives visual thalamic input from the dorsal lateral geniculate nucleus making the TDCtx the visual cortex of the turtle. These afferents extend further into the dorsal cortex [Hall and Ebner, 1970]. Functional and anatomical studies did not find any retinotopic responses or axon projections from lateral geniculate nucleus [Fournier et al., 2018, Hall and Ebner, 1970]. The TDCtx also contains spiny and smooth cells arranged simply within the three layers. The spiny pyramidal cells located in layer 2 (the pyramidal cell layer) and the smooth interneurons mainly in layers 1 and 3.

Excitatory cells The morphology of turtle PCs differ substantially from mammalian neocortical PCs [Ulinski, 1990]. Most prominently, turtle PCs lack the main apical dendrite and possess multiple apical dendrites branching proximal from the cell body [Larkum et al., 2008]. PCs in turtles show quite heterogeneous morphological subtypes [Ramón y Cajal, 1952]. There are only a few studies subdividing the excitatory neurons of the reptilian cortex into molecularly defined subtypes [Reiner and Beinfeld, 1985]. However, one study suggests that different classes of PCs in the TDCtx correspond functionally and in terms of gene expression to PCs in different layers of the neocortex [Dugas-Ford and Ragsdale, 2015]. Their axon projections have not yet been studied in detail but studies suggest projections locally and onto neighboring and contralateral cortical regions as well as subcortical regions [Desan, 1988]. A recent study using genetic classification tools was able to show two distinct classes of PCs that may also show a difference in their innervation profile targeting either intracortical or subcortical regions [Tosches et al., in revision].

Inhibitory cells In the TDCtx, interneurons account for less than 5% of all neurons [Smith et al., 1980] and different populations of INs mainly mediate feedforward (subpial cells; [Mancilla et al., 1998]) or feedback inhibition [Connors and Kriegstein, 1986]. Whole cell reconstructions [Colombe et al., 2004], electrophysiological recordings [Kriegstein and Connors, 1986] and immunocytochemical labeling [Reiner, 1993] of TDCtx interneurons suggest the existence of inhibitory interneuron classes defined by morphologically, expression marker and physiologically criteria in all three layers. Turtle progenitor cells of cortical INs originate subcortically and migrate tangentially into the pallium [Métin et al., 2007]. This developmental feature predates the divergence of reptiles and mammals [Cobos et al., 2001]. In turtles, data on interneuron marker expression are extensive and reviewed in detail by [Reiner, 1993].

Connectivity The primary dorsal cortex input from lateral geniculate nucleus (LGN) axons fan out below the pial surface and form en passant synapses with pyramidal cells and L1 INs [Smith et al., 1980]. The thalamo-cortical axons cross the lateral forebrain bundle and the pallial thickening, entering laterally the TDCtx and pass in a rostrocaudally orientation towards the turtle medial cortex [Ulinski, 1990]. As well as in the PCtx, superficial layer 1 INs receive a higher density of synapses by afferent axons than PCs do [Smith et al., 1980]. This may explain the observed strong inhibition evoked by sensory stimulation and the sparseness of pyramidal cell firing [Kriegstein and Connors, 1986]. Early tracing studies found that the visual field is projected onto the rostro-caudal axis of the TDCtx in the form of iso-azimuth lamellae covering the naso-temporal dimension of the visual field [Ulinski and Nautiyal, 1988]. However, this anatomical connectivity is not mirrored functionally [Fournier et al., 2018] and most studies point to a missing retinotopy mapping of visual to cortical space [Hall and Ebner, 1970]. Intracortical projections connect reciprocally to dorso-medial and medial cortices [Desan, 1984]. Most synapses on PCs come from cortical cells

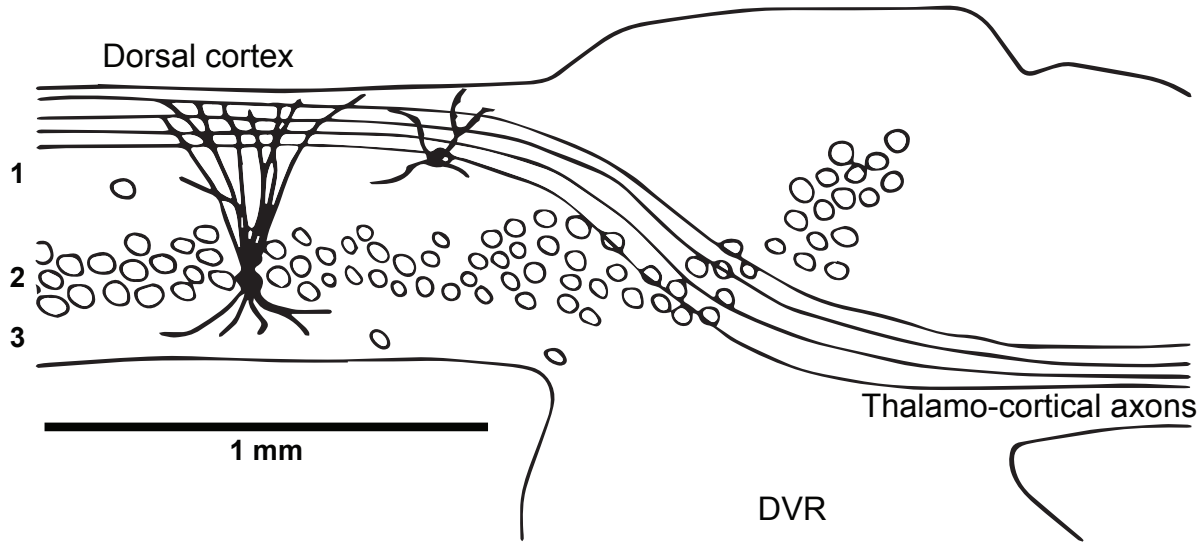

Fig. 2.5: **Thalamo-cortical axons in the turtle dorsal cortex.**
The coronal cross-section of the turtle dorsal cortex is shown and thalamic afferents run superficially from lateral to medial. The cortical layers 1, 2, and 3 are indicated on the right, and typical pyramidal and smooth stellate cells are illustrated. DVR: dorsal ventricular ridge.
Figure modified from [Colombe and Ulinski, 1997] with permission.

forming both feedforward and feedback circuits. In feedforward circuit pattern, PCs receive excitatory synapses from other PCs and inhibitory synapses from subpial and stellate cells, all of which directly receive excitation from geniculate afferents [Cosans and Ulinski, 1990]. Feedback circuits involve PCs receiving inhibitory input from INs which got excited by PCs [Kriegstein and Connors, 1986] (see Figure 2.6A).

2.2.3 Turtle dorsal cortex and mouse olfactory cortex in comparison

The olfactory cortex is assumed to be the region of the cortex least changed in vertebrate evolution. It is used to form a model for a basic cortical circuits that are reflected in circuit elements of the dorsal cortex of reptiles [Connors and Kriegstein, 1986, Smith et al., 1980] and maybe also by single circuit elements in the neocortex of mammals [Shepherd, 2011]. Besides the similar cortical architecture, the MPCtx and the TDCtx also share functional and anatomical characteristics (see Figure 2.6). Identifying

the structural and functional similarities between the reptilian dorsal and mammalian olfactory cortex could reveal common organizational and computational principals [Fournier et al., 2015]. The discussion about similarity to the ancestral cortical circuits rests on the common features, e.g. the tangential organization, with afferents running in the superficial layer and intracortical associative neural circuits beneath. The mammalian olfactory, reptilian olfactory and dorsal cortices exhibit a similar laminar organization and no apparent topographic mapping of the input (visual for dorsal cortex) and studies hint a mode of associative processing [Fournier et al., 2015] which is reflected by the substantial reciprocal interconnections with high-order cortical areas [Shepherd, 2011]. Thus, the cerebral cortex may have evolved from a basic tangential associative circuit with little radial and modular structure [Aboitiz and Montiel, 2015]. Note that modular structures have been reported to appear transiently during development in the pallium of reptiles and birds [Davila et al., 1999, Suárez et al., 2006]. The pyramidal neurons in both cortices are similar with respect to their dendritic electrophysiological properties, suggesting comparable integrative properties at the subcellular level [Larkum et al., 2008]. They also show morphological similarities with regard to the spine density of PCs and in comparison with piriform SL cells, the apical dendrites of turtle dorsal cortex PCs also branch from the cell body and fan up to layer 1 (see Figure 2.5 and Figure 2.3). The afferent fibers in both cortices innervate the apical dendrites of principle cells by en passant synapses [Haberly and Presto, 1986] and the superficial layer 1 interneurons receive a higher density of afferent input if compared to the innervation density of PCs [Smith et al., 1980, Suzuki and Bekkers, 2012]. Both cortices possess local feedforward and feedback inhibition transmitted via superficial layer 1 INs and basal inhibitory INs respectively [Haberly and Bower, 1984].

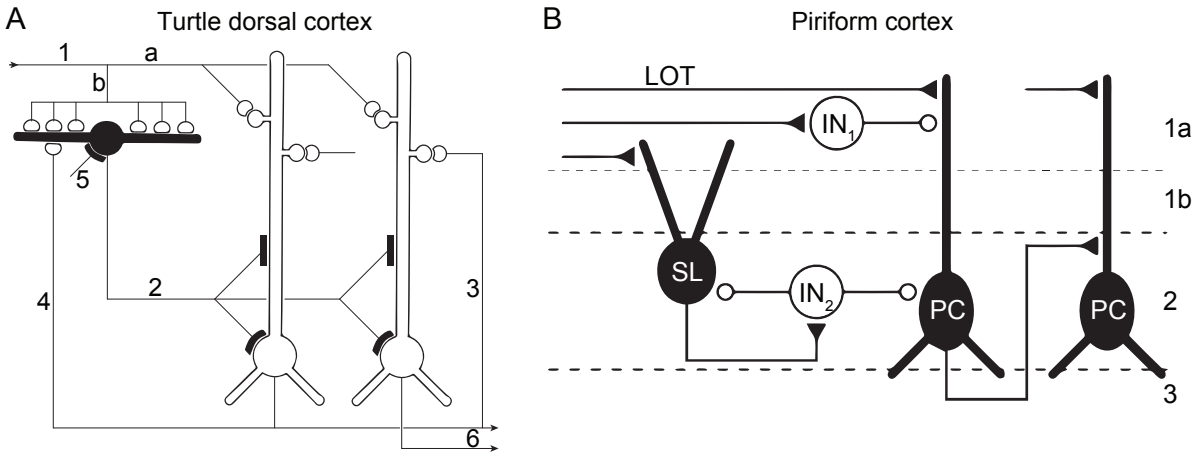

Fig. 2.6: **Feedback and feedforward circuit in the turtle dorsal and mammalian piriform cortex.**
(A) A schematic diagram shows the principal intracortical connections of the turtle visual cortex based on neuroanatomical data [Smith et al., 1980]. Thalamocortical afferent provide excitation onto pyramidal cell dendrites (a) and also excite inhibitory stellate cells (b). Feedforward inhibition is mediated by stellate cell-pyramidal cell contact (2). Local pathways mediate reciprocal excitation between pyramidal cells (3) as well as feedback inhibition through pyramidal cell-stellate cell contact (4). There is also physiological support for inhibition of stellate interneurons (5). The pyramidal cells provide output from the cortex (6). Figure modified from [Kriegstein and Connors, 1986] with permission. **(B)** The lateral olfactory tract (LOT) provides inhibition in layer 2 pyramidal cells (PCs). Feedforward inhibition is mediated by interneurons IN1 located in the layer 1a, whereas feedback inhibition is mediated by interneurons IN2 located in one of the deeper layers (1b, 2, and 3). Two targets of synaptic inhibition are glutamatergic semilunar (SL) and pyramidal neurons with their cell bodies located in layer 2.
Figure modified from [Suzuki and Bekkers, 2012] with permission.

2.2.4 Reptilian cortex and mammalian isocortex in comparison

The interneuron types in the mammalian cortex which are exclusively found in the upper layers (vasoactive intestinal peptide (VIP), cholecystokinin (CCK), choline acetyltransferase (ChaT) interneurons) are absent in the turtle dorsal cortex [Reiner, 1993]. In contrast, cell types prominent in layers 1, 5, and 6 of the mammalian neocortex (somatostatin (SST), neuropeptide Y (NPY), substance P (SP)) are found in the turtle dorsal cortex [Reiner, 1991]. These findings suggests the notion that layers 2, 3, and 4 are recent mammalian additions to a reptilian framework based on layers 1, 5, and 6. However, while some interneuron subtypes may be more common in certain layers of mammalian cortex, their distribution is often not exclusive. In mammals, VIP-, CCK-, SP-, and SST-positive interneurons can be found in all layers [Peters et al., 1983]. In addition, ChaT-positive neurons are found in the lizard cortex, although they appear to be absent from all other reptiles investigated [Reiner, 1991]. Developmental mechanisms for interneuron generation and migration most likely preceded the emergence of neocortical structures. Also, interneurons are not generated locally in the cortex but rather migrate from subpallial regions to all of the pallium, to extents comparable in birds [Cobos et al., 2001], frogs [Brox et al., 2004], and fishes [Carrera et al., 2008]. In conclusion, current evidence for the laminar position of interneuron subtypes in the mammalian cortex and developmental arguments make a suggestive, but not entirely tight case for a layer equivalence scheme between reptilian and mammalian cortices. The cell-poor cortical layer 1 can be compared across reptiles and mammals, both in terms of development and tangential connectivity [Marin-Padilla, 1971]. The laminar position, neuronal connectivity, density, and projection neuron morphology could support an upper layer equivalence. In particular, the cellular morphology of turtle pyramidal cells bears little resemblance with mammalian deep layer pyramidal cells [Larkum et al., 2008]. Instead, turtle pyramidal cells resemble the atypical pyramidal

cells of superficial layers in the mammalian isocortex [Sanides and Sanides, 1972]. These excitatory neurons are frequently characterized by spiny dendrites growing directly into the cell-free layer and possessing only a few basal dendrites and several larger apical branches. Gene expression studies in the reptilian cortex show that mammalian upper layer markers are also expressed in the dorsal cortex of reptiles [Dugas-Ford et al., 2012]. Identifying the homologous brain regions between reptiles and mammals is a largely unresolved issue [Striedter, 2016]. However, solving that question bears the promise of using the general structure-function principles of the 'simple' reptilian brain to understand the function of more complex cortical structures in mammals [Naumann and Laurent, 2017].

2.3 Connectomics

The mouse brain contains 157.500 neurons per mm^3 [White and Peters, 1993], four km of axon wiring per mm^3 which form on average one synapse per μm^3 [Braitenberg and Schüz, 1998]. The prominent feature of neurons lies in their number of contacts which adds up to one thousand other neurons [Helmstaedter, 2013]. The term 'Connectomics' was introduced in 2005 as 'comprehensive structural description of the network of elements and connections forming the human brain' [Sporns et al., 2005]. Synaptic connections between neurons are relevant to understand the brain's computations which give rise to perception, behavior and memory. However, it is yet unknown whether the brain is organized in distinct modules (e.g. as cortical columns [Hubel and Wiesel, 1963, Mountcastle, 1978]) which function as isolated computational units. Connectomics electron microscopy (EM) methods are currently investigated and developed for the challenge of single synapse Connectomics of whole mouse brains [Mikula, 2016]. On a different scale, Connectomics also includes the mapping of distinct brain regions or sparse neuron populations and their connectivity

using low resolution techniques such as functional magnetic resonance imaging (fMRI) and light microcopy. However, high resolution electron microscopy-based Connectomics alone allows visualization of synaptic contacts and considering their development trajectory, it may be the most feasible method to densely analyze cortical circuits and potentially whole brains at single synapse resolution [Mikula, 2016].

2.3.1 Electron microscopy-based Connectomics

The smallest diameters of neuronal processes determine the minimal required resolution for dense neural circuit mapping. Axons and dendritic spine necks become as thin as 50 nm, which requires a minimal resolution of 25 - 30 nm [Helmstaedter, 2013]. The resolution of light microscopic techniques is limited by light's minimal wavelengths to roughly 200 nm [Lipson, 1998] and methods trying to overcome that limit (e.g. stimulated emission depletion microscopy (STED) [Hell and Wichmann, 1994], stochastic optical reconstruction microscopy (STORM) [Rust et al., 2006] or photo-activated localization microscopy (PALM) [Betzig et al., 2006] are able to work below that limitation. However, the major limitation of light microscopy methods is the requirement of sparsely labeled tissue. Electron-microscopy techniques are able to overcome these mentioned challenges and are therefore suitable for cortical circuit mapping.

The first electron microscopy-based neural circuit analysis was published 1986 by Sydney Brenner and colleagues [White et al., 1986]. 302 neurons of the nematode *C. elegans* have been mapped and reconstructed facing challenges with data acquisition and analyses which are partially still present today. Researchers are still working on this data: a complete reconstruction based partially on these initial results (for example the study restored a major gap in the connectivity of ventral cord neurons) has since been published [Varshney et al., 2011]. Since then, a broad range of electron microscopic

approaches for high resolution connectomic circuit analyses were developed.

All EM-based connectomical research requires the extraction of nerve tissue or even entire brains which are consecutively stained yielding contrast for EM imaging. The stain is usually provided by heavy metal compounds like osmium tetroxide (OsO_4) and uranyl acetate in order to outline membranes, visualizing for example neuronal processes and synaptic vesicles [Hua et al., 2015]. In addition, heavy metal compounds provide electrical conductivity to prevent electron accumulations and reduce poor image quality. After extraction of brain tissue and consecutive staining, there are several EM imaging and cutting techniques available to obtain 3D EM volumes for dense circuit reconstructions All methods have their challenges and benefits and are based on two phases: two dimensional electron microscopic imaging and slicing or milling tissue from the block-face. In addition, every technique strives to avoid even single section loss over long periods of imaging or alternations of cutting and imaging over months or even years [Helmstaedter, 2013, Mikula, 2016]. Acquired EM images are consecutively aligned into three-dimensional image stacks for reconstruction and analysis.

Serial-section transmission electron microscopy (ssTEM)

Serial section transmission electron microscope (ssTEM) is the first applied approach in electron microscopy-based Connectomics studies (see [White et al., 1986]). The brain tissue block is sectioned with a diamond knife within an ultramicrotome and cutting thickness range from 40 - 90 nm [Briggman and Bock, 2012, Helmstaedter, 2013]. Sections are manually collected on grids for transmission electron microscope (TEM) imaging. TEMs allow large fields of view and a high in-plane resolution. The challenges of the method are the limitation of the minimal cutting thickness (z-resolution) and the high loss-rate of slices along the cutting axis due to the manual processing. Commercial TEMs yield slow image acquisition speeds which stipulated the development to use arrays of high-speed charge-coupled device (CCD) cameras (e.g. transmission

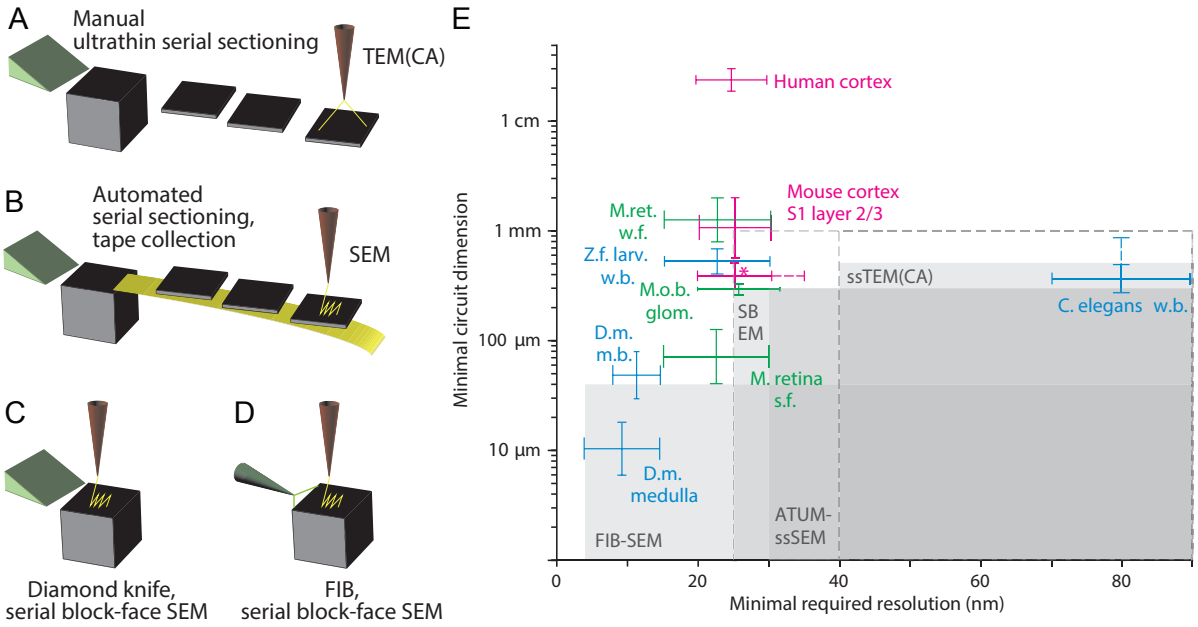

Fig. 2.7: **Volume electron microscopy techniques for cellular Connectomics and their spatial resolution and scope.**
(A) - (D) Conceptional sketches of four used methods for dense neural circuit reconstruction: **(A)** conventional manual ultrathin sectioning of brain tissue and consecutive transmission electron microscope (TEM) or transmission electron microscopy camera array (TEMCA) imaging [Bock et al., 2011], **(B)** automated tape collecting ultra microtome (ATUM) [Hayworth et al., 2006a], **(C)** scanning electron microscope (SEM) [Denk and Horstmann, 2004] and **(D)** focused ion beam scanning electron microscope (FIBSEM) [Knott et al., 2008]. **(E)** The approximate minimal resolution and smallest spatial dimension which is typically yielded with the imaging techniques in **(A) - (D)** is depicted.
Figure taken from [Helmstaedter, 2013] with permission.

electron microscopy camera array (TEMCA)), resulting in an order of magnitude acquisition speed-up [Bock et al., 2011]. Further development (TEMCA2) yield net imaging throughput of 50 Mpixel/s [Zheng et al., 2017]. TEMs allow higher electron doses resulting in higher resolution and contrast and sections can be further processed (e.g. immune labelling) and reimaged. Known challenges are high rate of lost sections, the slow slicing, the comparable low z-resolution, the slow image acquisition speed and the difficult alignment of acquired data [Helmstaedter, 2013].

Automated serial-section tape-collection electron microscopy (ATUM)

The automated tape collecting ultra microtome (ATUM) method offers the automation of slicing and slice collection and thus, reduces the slice loss-rate, increases the cutting speed and reduces the cutting thickness [Hayworth et al., 2006b, Schalek et al., 2011, Helmstaedter, 2013]. However, manual work (cutting and gluing the tape onto silicon wafers) is still needed to prepare the collected slices for EM-imaging. The original development of the automated tape collecting ultra microtome (ATUM) included TEM imaging using stamped collecting tape [Hayworth et al., 2006a], which was substituted for scanning electron microscope (SEM) imaging [Schalek et al., 2011]. The benefits of ATUM is in particular the non-destructive preparation of tissue slices which can be reimaged if needed. Although parallelization of imaging is possible, recent EM techniques offer more feasibility to use parallelization of electron beams within one setup ([Eberle et al., 2015] see section 'Multibeam SEM') rather than multiple single beam setups. This method requires low resolution registration of slices on tape first and then the slices are imaging with 61 hexagonally arranged electron beams in parallel, allowing acquisition speeds of about 1 GHz aiming for two order of magnitude higher imaging speeds [Eberle et al., 2015]. However, remaining challenges are the sensitivity of the cutting system which can cause higher than expected section loss and wrinkled sections hampering image alignment.

Serial block-face scanning electron microscopy (SBEM)

The serial block-face electron microscopy (SBEM) method is destructive (sections cannot be reimaged) and most prominently cutting and imaging are linked within the SEM by a custom-made microtome [Denk and Horstmann, 2004]. The block-face is typically imaged at 12 nm in plane resolution [Briggman et al., 2011, Helmstaedter et al., 2013] and consecutively cut by a diamond knife, removing 25 - 30 nm tissue off from the block's surface [Berning et al., 2015]. Imaging and cutting is synchronized by custom-written software offering a high degree of automation. The method allows large field of view and cutting series of at least 300 µm [Briggman et al., 2011] and the volume alignment of data yields low error rates. The known challenges of the method are the destructive cutting procedure generating debris particles which interact with the electron optics causing reduced signal amplitude, defocus and distorted image geometry during acquisition. In addition, the diamond knife wears off during long-term acquisition experiments.

Multibeam SEM

Imaging larger fields (e.g. entire mouse brain) results in proportionally larger experiment times, thus, increasing imaging speed reduces experiment time or offers imaging of larger tissue volumes in reasonable timespans. The recent introduction of a commercially available multi-beam scanning electron microscope (mSEM) offer potentially significant improvements in imaging speeds for SBEM and ATUM by using electron beams in parallel within a single machine. Development of next generation SBEM setup is ongoing and imaging will be done using 91 parallel electron beams and the microtome will be able to cut entire mouse brains [Mikula, 2016]. The challenge of high electron doses during imaging is approached by introducing in-chamber block-face coating [Titze and Denk, 2013, Mikula, 2016].

The multibeam EM technique is already utilized by the ATUM method, using 61 electron

beams in parallel for the EM acquisition [Eberle et al., 2015].

Focused ion beam scanning electron microscopy (FIBSEM)

The focused ion beam scanning electron microscope (FIBSEM) method is similar to the SBEM method, both linking the imaging and destructive sectioning phase within the microscope chamber. However, the two techniques differ with regard to the cutting mechanism. FIBSEM uses a focused gallium ion beam to mill the tissue's block-face [Knott et al., 2008]. This milling technique offers high precision allowing down to 4 nm milling thickness yielding isotropic voxel resolution of less than 10 x 10 x 10 nm^3 [Hayworth et al., 2015]. The challenges of the method is the limited z-depth of milling (40 µm), which is enough for small volume Connectomics like the fly brain [Helmstaedter, 2013]. Noteworthy, fly brains contain even smaller neural processes than mammalian brains making FIBSEM the suitable method with a limited but enough volume capability and a higher voxel resolution [Hayworth et al., 2015].

Hot knife with FIBSEM Further development to overcome the z-depth limitation of the ion beam milling resulted in the 'hot knife microtomy' technique [Hayworth et al., 2015]. Tissue blocks are sliced into 20 - 30 µm thick sections using an ultrasonic diamond knife which operates at a temperature up to 60 °C. The cutting aims for later realignment of these sections yielding larger neural tissue volumes. In addition, section imaging can be parallelized. The border alignment is still challenging and small processes in between sections can be lost.

Achievements of EM-based Connectomics Mapping the connectivity of neural circuits from 3D EM data requires identifying each neurite and its pre- and postsynaptic partners. The first EM-based Connectomics research (see [White et al., 1986]) was performed by a single annotator reconstructing 302 neurons of the nematode by

contouring their volumes. The work-time is estimated being between ten to twenty thousand hours. Today, following and reconstructing neural processes is still primarily done by human annotators [Helmstaedter, 2013]. This approach of human-based contouring is very time-consuming (200 - 400 $\mathrm{h\,mm^{-1}}$ neurite reconstruction) and therefore prohibitive for larger circuit reconstructions [Helmstaedter et al., 2008, Helmstaedter et al., 2011]. Development of reconstruction techniques went from contouring to placing connected nodes at the center of neurites yielding a skeleton representation of whole neurons. This 'skeletonization' allowed annotation speed-up 50-fold with up to 3 - 9 $\mathrm{h\,mm^{-1}}$ path length and was used in recent mammalian circuit reconstructions [Briggman et al., 2011, Helmstaedter et al., 2013]. In addition, the annotation labor was parallelized by the help of more than one hundred undergraduate annotators providing thousands of reconstruction hours [Helmstaedter et al., 2011]. Further improvement of annotation software has been published [Boergens et al., 2017] and [Schmidt et al., 2017], speeding up the manual reconstruction work by a factor 4 - 13, still limiting manual work to reconstruction of smaller circuits. Reconstruction times for dense circuit mappings in current and future datasets render exclusive human annotation as impossible. Estimated reconstruction times of circuit mapping of an entire mouse brain e.g. add up to 500.000 years reconstruction time at total costs of 50 billion Euros [Mikula, 2016]. However, human annotation will support automated, machine-learning-based algorithms by proofreading them and thus improving the results. First, automated reconstruction algorithms [Jain et al., 2010, Turaga et al., 2010, Varshney et al., 2011] were lagging behind human annotators accuracy and only used in combination with massive manual annotation [Helmstaedter et al., 2013, Takemura et al., 2013]. Latest developments in machine learning algorithms aim to reduce the required human annotation time by a factor of ten which is needed for circuit reconstructions on the nanoliter scale within reasonable

time scales [Berning et al., 2015]. Identification and reconstruction of neurons is the first part followed by detecting all synaptic contacts and the associated neuron identity in a given volume. The manual synapse identification on reconstructed axon paths yield about 1.6 $\mathrm{h\,mm^{-1}}$ path length which results in ∼730 years manual annotation time for all the synapses in 1 $\mathrm{mm^3}$ [Staffler et al., 2017]. Recent machine learning algorithms like SynEM [Staffler et al., 2017] offer automation of synapse detection with high precision and recall. The automation of both, neuronal reconstruction and synapse identification, enables research to tackle large volume and even whole brain circuit mapping. Both imaging and reconstruction methods are still evolving and they have already proven to answer important biological questions.

Challenges of EM-based Connectomics All approaches share similar challenges as they are time-consuming, technically complex and expensive (e.g. whole mouse brain data disk storage costs: 2.8 million Euros and the human whole brain data disk storage costs: 8.7 billion Euros [Mikula, 2016]. Data storage requirements add up to hundreds of gigabytes [Bock et al., 2011, Helmstaedter, 2013, Briggman et al., 2011], hundreds of terabytes [Mikula, 2016] and whole brain projects in the tens of petabytes [Mikula, 2016]. The storage and the access challenge both require an increase in bandwidth requirements. In recent years, both the staining and imaging techniques improved in quality and speed, increasing the development pressure of data analyses which represents the major bottleneck of cortical circuit reconstructions [Helmstaedter, 2013].

2.3.2 Light microscopy-based Connectomics

First insights into cell-types and connectivity of the brain was done using light microscopy requiring reliable staining of neurons [Osten and Margrie, 2013]. Individual innervation pathways were mapped using tracers revealing connectivity motives in the brain [Rockland and Pandya, 1979] and recent methodological developments in

neuronal labeling (anterograde and retrograde tracer injections) further support light microscopy-based Connectomics [Osten and Margrie, 2013]. The automation of light microscopy is used to acquire a mesoscopic connectivity map of the whole mouse brain ('mesoscopic connectome') [Bohland et al., 2009, Osten and Margrie, 2013] (e.g. Allen Institute for Brain Science). Similar to EM techniques, light microscopy three-dimensional datasets for brain wide connectivity are achieved by alternating light microcopy imaging and tissue slicing which is demonstrated by the approach serial two photon tomography (STP) combining two photon microscopy (2P) [Denk et al., 1990] with sectioning (about 50 µm) the imaged brain block [Ragan et al., 2012]. While mesoscopic connectome approaches are suitable to contribute valuable insights into brain wide cell-type distribution and connectivity between anatomical regions [Bohland et al., 2009, Osten and Margrie, 2013], dense neuronal circuit reconstruction remains a key feature of electron microscopy methods. New methodological attempts are developed to overcome the resolution barriers and its lack of synapse visualization like expansion microscopy (ExM) which magnifies the tissue and all its processes uniformly using a polymer system [Chen et al., 2015]. Another major limitation for light microscopy techniques are densely labelled neural tissues which is challenged by recent explorations combining ExM with barcode-guided agglomeration using RNA-barcodes which labels each neuron uniquely and can be read-out optically [Peikon et al., 2014, Kebschull et al., 2016, Chang et al., 2017]. While these approaches are promising for the near future, the well-established method in-vivo light microscopy imaging generates valuable knowledge about neural circuits driving behavior, perception and memory which relies not only on connectivity but also its function [Grinvald et al., 1999]. The combination of functional 2P calcium imaging and 3D EM have already produced invaluable insights in the retina's structure-function relation [Briggman et al., 2011] and the investigation of cortical structure-function relation is already undertaken (Hua et al.,

in preparation).

2.3.3 Electrophysiology-based Connectomics

The methods patch clamp and whole cell recordings are used for measurement of neuronal functional properties, classification of cell types and mapping neuronal receptive fields (e.g. [Brecht and Sakmann, 2002]. Using a set of pipettes for paired electrophysiological recordings show synaptic connections at a pairwise level (e.g. [Jiang et al., 2015]). The attempt of using electrophysiology alone however is rather questionable whether it may be able to reveal neural circuit organization on a dense connectivity level.

2.3.4 Magnetic resonance imaging-based Connectomics

The field of magnetic resonance imaging (MRI) offers a variety of approaches like task fMRI, resting-state fMRI (rfMRI) or diffusion MRI for mapping macroscopic functional connections. Resting-state fMRI (rfMRI) reveals connected brain areas by interpreting hemodynamic time courses and it is especially suited for studies in humans since it is non-invasive. However, the low resolution is prohibitive to decipher brain wiring mechanisms at a local circuit level [Hagmann et al., 2010].

2.4 Wiring rules

The rules underlying the neuronal connectivity and the location of synapses are rather unknown and two possibilities will be introduced in the following: Peters' rule and specific wiring.

2.4.1 Peters' rule

There are three conceptual distinct interpretations of Peters' rule which correspond to increasing levels of resolution [Rees et al., 2017].

1. On a cell type level as originally proposed, Peters' rule predicts synapses between neuron types by their anatomically collocated axon and dendritic arbors [Peters and Feldman, 1976, Peters and Payne, 1993, Braitenberg and Schüz, 1998]. The quantitative prediction of synapses scales with the overlap of axons and dendrites, but the connectivity of individual cells within each type is not considered.

2. For individual neuron pairs the rule implies that spatial overlap of axon and dendrites among a pair of neurons predicts the number of synapses. However, the actual connectivity heavily depends on at least two factors: the spatial geometry (e.g. branching patterns, relative orientation and overlap) and the specificity of the neurites in question.

3. The interpretation on a subcellular resolution predicts the number of synapses between connected neurons based on the overlap of their axon and dendritic arbors at a set proximity. This is further applied to single axons and their fractional availability of subcellular postsynaptic structure classes (e.g. axon initial segment, cell body or dendritic shaft) to predict the axon's synapse target distribution. Connection strength between two neurons correlates with the product of densities of axon boutons and dendrites [Binzegger et al., 2004, Shepherd and Svoboda, 2005]. Additionally, synaptic strength on a single synaptic level is considered homogeneously ('form follows function', [Kristan and Katz, 2006]). Although, a geometrical proximity is required for synapse formation, this is however most likely not the only predictor. Laminar and columnar positions of pre- and postsynaptic neurons also influence connection strength, indicating location dependent circuit organization [Shepherd and Svoboda, 2005].

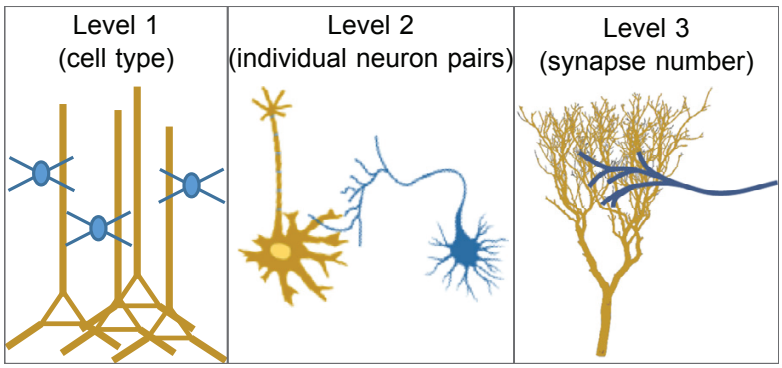

Fig. 2.8: **Three conceptually distinct interpretations of Peters' rule.**
Level 1, prediction of synapses formed among neuron types. Here, pyramidal cells in yellow and axons of one type of interneurons in blue collocate their dendrites and axons which is used as a proxy to estimate the synaptic connection strength. Level 2, prediction of synapses formed between overlapping axon (blue presynaptic neuron) and dendritic (yellow postsynaptic neuron) arbors of individual neurons. Level 3, prediction of synapses formed on a subcellular resolution by observing the proximity of individual axon branches (blue) for subcellular postsynaptic structures (e.g. cell bodies, axon initial segments, dendrites (yellow)).
Figure modified from [Rees et al., 2017] with permission.

2.4.2 Wiring specificity

Studies show several examples of axon wiring which do not follow the proposed Peters' rule, but rather contradict the principle. The opposite of Peters' rule might be a specific wiring which is not following geometrical availability, e.g. layer 2 and 3 Chandelier cells [Somogyi, 1977]. These neurons have been shown to display strong wiring specificities which can be summarized by two fundamental principles:

a) The primary postsynaptic target structure is an axon initial segment (AIS)

b) The primary postsynaptic target neuron is a pyramidal cell [Somogyi et al., 1982].

Other examples showing specific wiring are demonstrated by Basket cells preferentially targeting neuronal cell bodies [Jones, 1984] and interneuron-specific interneurons [Freund and Buzsáki, 1996, Klausberger and Somogyi, 2008]. Further examples can be found in thalamo-cortical projections in V1 [Reid and Alonso, 1995] and S1 [White and Hersch, 1982, Benshalom and White, 1986] as well as in cortico-thalamic

[White and Keller, 1987] and retinal projections [Briggman et al., 2011]. These mentioned examples might be interpreted as a contradiction of random wiring principles hypothesized by Peters' rule, implicating the complexity of circuit organization beyond geometrical motives. Wiring diagrams for local or global circuits remain very challenging and expensive to generate and they might be crucial to fully understand the brain's circuit wiring principles and consequently its function.

This projects is an effort to further understand how cortical processing is done by revealing and comparing structural neural circuit pattern within three-layered cortices of turtles and mice. The existence of such target-specific inhibitory wiring in the mammalian cortex has inspired substantial functional implications concerning effects on neuronal activity gain control [Shapley and Xing, 2013], action potential timing [Huang et al., 2013] and the resulting implementation for cortical basic algebraic operations.

In this study, three-dimensional EM datasets were acquired from the mouse piriform cortex (MPCtx) and the turtle dorsal cortex (TDCtx). The connectivity of axons targeting neuronal cell bodies, axon initial segments and dendrites of principal neurons were reconstructed in both cortices. The results revealed that turtle cortex axons do not show distinct separation between excitatory and inhibitory synapse targets which have been reported for mammalian cortices. The lack of such target specificity might indicate a fundamentally different neuronal implementation between reptiles and mammals and underline that connectomic circuit patterns can be substantially different despite an overall similar cytoarchitecture and functional similarities. At the same time, these results raise an important set of questions about the algorithmic or computational similarity (according to Marr's three levels of understanding, [Marr, 1982]) between the reptilian and mammalian cortex.

3 Materials and Methods

3.1 Animal experiments

All animal experiments were performed in accordance to the law of animal experimentation issued by the German Federal Government under the supervision of local ethics committees and according to the guidelines of the Max-Planck Society. All chemicals and reagents were purchased from Sigma-Aldrich, Serva, Roth, and VWR unless stated otherwise in the following.

3.1.1 Brain tissue preparation

Male wild-type mice (C57BL/6J, Jackson Laboratory, Bar Harbor, Maine) with a body weight of 16 - 20 g were anesthetized with isoflurane (induction: 4%, maintenance: 2%). When no reflexes were detectable anymore, mice were perfused transcardial (flow rate 10 ml/min maintained by Standard PHD ULTR CP Syringe Pump, Harvard apparatus, Holliston, USA) with 15 ml Cacodylate buffer (0.15 M, pH 7.4) and 50 ml fixation solution (cacodylate buffer (0.08 M, pH 7.4), 2,5% PFA, 1,25% glutaraldehyde, 2 mM CaCl) followed by decapitation, removal of skull bones caudally and incubation in fixation solution for at least 12 h at 4 °C. The brain was extracted from the skull and tissue from the piriform cortex was extracted with a biopsy punch (1 mm diameter, Millitex) using the mouse brain atlas [Paxinos and Franklin, 2008] as a reference map.

Female turtles (Trachemys scripta, Nasco Inc., Fort Atkinson, USA) with a body weight of 277 g and 298 g were anesthetized using ketamin 0.3 ml/kg und dexdomitor 0.225 ml/kg. Female animals were used due to limited supply of male turtles. The local circuit connectivity in the turtle dorsal cortex was expected to be comparable in between sexes. When reflexes were not detectable anymore, the turtles were decapitated and transcarotidal perfused (gravity) with 80 ml cacodylate buffer (0,15 M, pH 7.4) and 250 ml fixation solution (cacodylate buffer (0.08 M, pH 7.4), 2,5% PFA, 1,25% glutaraldehyde, 2 mM CaCl) followed by incubation of the intact skull in fixation solution for at least 12 h at 4 °C. The brain was extracted from the skull, the cortex was separated and tissue from the dorsal cortex was extracted with biopsy punches (1 mm diameter, Millitex) penetrating the tissue radially from the ventricular side.

3.2 Electron microscopy tissue staining

The applied staining protocol was taken from [Hua et al., 2015]. En bloc staining was performed on the extracted specimens by incubating in 2% OsO_4 in cacodylate buffer (0.15 M, pH 7.4) for 90 min at room temperature (RT). Then, the specimens were transferred into 2.5% ferrocyanide in cacodylate buffer (0.15 M, pH 7.4) for 90 min at room temperature. Next, the specimens were incubated in thiocarbohydrazide (saturated) for 45 min at 40 °C and transferred into nanopure filtered water twice for 30 min. Then, specimens were incubated in 2% OsO_4 aqueous solution for 90 min at room temperature and transferred into nanopure filtered water twice for 30 min. The specimens were kept in 1% uranyl acetate aqueous solution overnight at 4 °C. The next day, the specimens were warmed to 50 °C for 120 min in 1% uranyl acetate aqueous solution and transferred into nanopure filtered water twice for 30 min. Next, the specimens were incubated in lead aspartate (0.066 g lead nitrate in 10 ml, 0.03 M aspartic acid, pH adjusted to 5.0 with KOH) for 120 min at 50 °C followed by incubation in graded

ethanol and put into acetone. Then, the specimens were incubated in 1:1 mixture of acetone:resin (4.1 g ERL 4221, 0.95 g DER 736, 5.9 g NSA, Spurr Low-Viscosity Embedding Kit) for 12 h on rotator at RT, 1% DMAE was added and the specimens were incubated for 6 h at RT. Consecutively, the specimens were placed on custom-made aluminum cylinders (diameter 10 mm, length 25 mm, conical head) and then cured at 70 °C for at least 48 h in pre-warmed oven (Universal Oven Um, Memmert, Schwabach, Germany). Note, the mouse piriform cortex specimens were placed on aluminum cylinder so that cylinder axis and pia plane were parallel.

The turtle cortex tissue staining and curing was performed analog to mouse cortex tissue. Note, the turtle dorsal cortex specimens were placed on aluminum cylinder so that cylinder axis and pia plane was orthogonal and the pia surface was facing down.

3.3 Specimen preparation

3.3.1 Specimen trimming

The specimens were kept on aluminum cylinder and further processed for serial block-face electron microscopy (SBEM) acquisition [Denk and Horstmann, 2004]. The specimens were trimmed using a diamond-head milling machine (EM Trim, Leica, Wetzlar, Germany) to a cube of 700 x 700 x 1000 µm^3. The cube block-face was further trimmed using an ultramicrotome (UC7, Leica, Wetzlar, Germany), gold-coated (100 nm) (ACE600, Leica, Wetzlar, Germany) and placed in the custom-built SBEM microtome (courtesy of W. Denk, MPI of Neurobiology, Munich) which was mounted inside the scanning electron microscope chamber (Quanta FEG 200, Thermo Fisher, Hillsboro, USA).

3.3.2 Specimen approaching

A binocular (Zeiss S90, Zeiss, Oberkochen, Germany) maintained in position by a custom-made holder was used to visually control the next steps. The diamond knife (Diatome, Biel, Switzerland) edge was positioned above the block-face of specimen. The specimen was lifted until the specimen block-face distance to the knife edge was roughly 20 µm which was measured with the built-in scale of the binocular. The diamond knife edge and the specimen block-face width were aligned by shifting the custom-made diamond knife holder. The diamond knife edge was positioned so that the specimen width was completely within the knife edge's boundaries. The diamond knife cutting stroke window was set to cover the specimen block-face length completely. The custom-written software controlling the cutting mechanism was started which operated the alternating lifting of the specimen by 50 nm and cutting strokes. This was performed until the specimen block-face was cut completely. The Lifting and cutting was continued while the SBEM microtome was inserted into a field emission gun scanning electron microscope (Quanta FEG 200, Thermo Fisher, Hillsboro, USA) and the chamber was evacuated to 10^{-5} - 10^{-6} mbar.

3.4 Data acquisition

The datasets acquired from turtle dorsal cortex L2 and L1 were from the same specimen and a different animal was used for the turtle dorsal cortex L3 dataset. The cutting mechanism and imaging procedure were controlled using custom-written software which was executed by the Spike2 software (Cambridge Electronic Design Limited, Cambridge, England). The scanning parameter were: pixel dwell time of 2.8 - 3.2 µs, 11.86 nm or 12 nm pixel size and spot size 3.5 (calibrated to a dose of about $\sim 16\ \frac{e}{nm^2}$) which yielded an image acquisition speed of 310 - 350 $\frac{kVx}{s}$. The backscattered electrons (BSE) were

detected using a custom designed detector (AXUV, International Radiation Detectors Inc., Torrance, USA) and the signal was amplified using a custom-built current amplifier (courtesy of W. Denk, MPI of neurobiology, Munich). The image acquisition and in plane motor movements were set to take two images (8 bit color depth) overlapping roughly 1 - 2 µm at the long edge of the images after motor movement. The image size was set to 6144 x 4096 pixels at a pixel resolution of 11.63 nm and 12.00 nm for turtle dorsal cortex L2 and L1, and mouse piriform cortex L2, respectively. The image acquisition and in plane motor movements of turtle dorsal cortex L3 tissue were set to take 9 images (size 2048 x 2768 pixels at 11.73 nm in plane resolution) arranged as a 3 by 3 tiles grid overlapping roughly 1 - 2 µm between images after motor movement. The cutting thickness was initially set to 25 nm for all acquisition experiments. When inconsistent cutting was observed in acquired images (e.g. partial cutting, cut/no cut in consecutive planes, etc.), the cutting thickness was increased by 1 nm steps until consistent cutting was observable. The final cutting thicknesses were set to 30 nm and 28 nm for turtle specimen and mouse specimen acquisition, respectively.

In turtle dorsal cortex L2 and L1 and mouse piriform L2 acquisition, lower resolution images (6144 x 4096 pixels at 46.52 nm and 29.96 nm in plane resolution) were taken after each cut (see Figure 3.1). In addition, 3222 images (size 6144 x 4096 pixels at 46.52 nm in plane resolution with a cutting thickness of 50 nm) were taken in between the locations from which the turtle dorsal cortex L2 and L1 datasets were acquired. The number of cuts, the cutting thickness and the resolution for all datasets are given in Table 3.1.

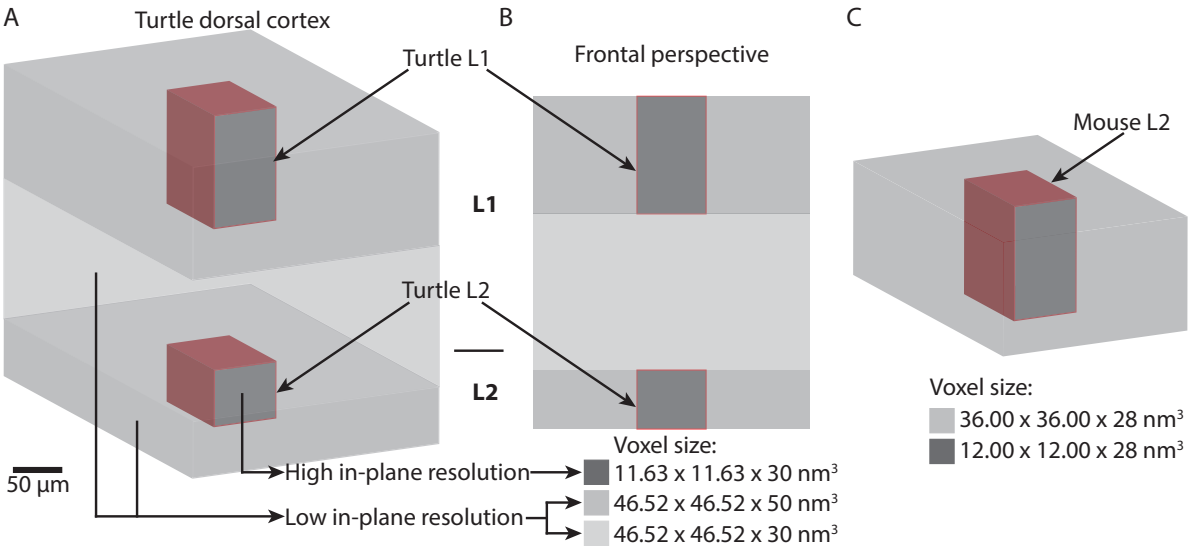

Fig. 3.1: **The location of acquired datasets in turtle dorsal cortex L1, L2 and mouse piriform cortex L2.**
(A)+(B) Conceptional sketch indicates the locations of turtle dorsal cortex L1 and L2 SBEM datasets which were acquired from the same turtle specimen. Before each high resolution image was taken, a low resolution image was acquired for both datasets. In between the two datasets, 3222 low resolution images were acquired and the specimen was cut at 50 nm. **(C)** Sketch indicates the location of the high and low resolution mouse piriform cortex L2 datasets.

Table 3.1: **Electron microscopy conditions and parameters.**

	TDCtx L3	**TDCtx L2**	**TDCtx L1**	**MPCtx L2**
Pixel size [nm^2]	11.73 x 11.73	11.63 x 11.63	11.63 x 11.63	12.00 x 12.00
Dwell time [µs]	3.5	2.8	2.8	3.0
Cutting thickness [nm]	30	30	30	28
Number of cuts	2328	2101	4056	4362
Image size [pixel]	2048 x 1768	6144 x 4096	6144 x 4096	6144 x 4096
Size image grid	3 x 3	1 x 2	1 x 2	1 x 2

3.4.1 Monitoring of acquisition and reapproaching

The stack acquisitions were monitored and corrected if needed for stable focus and astigmatism. The acquisition was paused every 1000 - 1500 imaged block-faces, the specimen was lowered 50 µm and the chamber was vented. The debris dust was removed using pressurized air, then chamber was closed and evacuated to the previous pressure level. The specimen was lifted 45 µm and acquisition was continued using initial cutting thickness settings and imaging was performed at 1536 x 1024 pixels and $\frac{1}{16}$th of the initial in plane resolution. Then, each image was observed whether the block-face was cut. When the observation was positive the block-face was reimaged using the originally set resolution and acquisition with the initial parameters and the experiment was continued.

3.4.2 Image alignment

The acquired EM images were stitched into a global reference frame using a custom-written alignment tool. First, in-plane alignment was done using cross-correlation on the overlap regions of neighboring image pairs. The cross-correlation

peaks were used to align all images in plane. Next, the middle region (1024 x 768 pixels) from the first plane was cross-correlated with the same region from the next image plane using the assumption that subsequent planes were similar due to the thin cutting. The translation to cross-correlation peak were used to shift the second image. This was done for all aligned planes and consecutively the aligned data was converted into the KNOSSOS data format ([Helmstaedter et al., 2011]; www.knossostool.org) by splitting the whole volume data into cubes sized 128 x 128 x 128 voxels each. The converted data was uploaded to the online data annotation software webKnossos [Boergens et al., 2017] for in-browser distributed data visualization, neurite skeletonization, synapse identification and volume reconstruction.

3.4.3 Transmission electron microscopy

The serial section and whole cortical thickness spanning single slice transmission electron microscope (TEM) data used for comparison were acquired from turtle (Trachemys scripta, Nasco Inc., Fort Atkinson, USA) using conventional TEM preparation methods. The data was kindly provided by Silke Haverkamp (Max Planck Institute for Brain Research, Frankfurt, Germany). The turtles were perfused by Christian Müller (Department of Neural Systems, Max Planck Institute for Brain Research, Frankfurt, Germany). The brain tissue specimens were prepared, stained, and acquired by Catharina Schilt (Max Planck Institute for Brain Research, Frankfurt, Germany) and Gongsun Nam (Max Planck Institute for Brain Research, Frankfurt, Germany). The image post-processing and alignment was done by Stephan Junek (Max Planck Institute for Brain Research, Frankfurt, Germany).

3.5 Reconstructions

The reconstruction was done using an in-browser data visualization [Boergens et al., 2017] and converting raw data signal of cell bodies, axons and dendrites into abstract skeleton representations by manual annotation ([Helmstaedter et al., 2011]; www.knossostool.org). A skeleton representation is an undirected graph consisting of nodes which are connected via edges. The tool webKnossos visualizes data in three viewports. The 'red' viewport displays in plane raw EM data, the 'blue' and 'green' viewport displays the pixel values of stacked image planes orthogonally to each other and the 'red' plane. Each plane can be moved via the computer mouse (holding the left bouton and moving) and the next or previous plane is shown by pressing the keyboard keys 'd' or 'f' respectively. The nodes are set at the location of the cursor by clicking the right computer mouse bouton (each node is then assigned to a specific coordinate inside the data's boundary). Every new node placed by the operator is connected via an edge with the previous node. For example, reconstruction of an axon was done by identification of the axon cross section in the plane visualizing it the most circular, annotating the middle of the axon cross section by placing a node, consecutively revealing the next 10-15 planes and placing again a node in the middle of the axon cross section. More features of webKnossos can be found online (webknossos.brain.mpg.de).

3.5.1 Synapse annotation

The synapses were identified using the tool webKnossos. The additional label feature enables the operator to assign a string of words to each node individually which was used to mark the location of the synapse, link the synapse to an axon and add the information about the postsynaptic target class (e.g. dendritic spine head, shaft, cell body, etc.).

Identification of synapses using the raw EM data visualized by webKnossos based on multiple (but not necessarily all) criteria/arguments (see Figure 3.2):

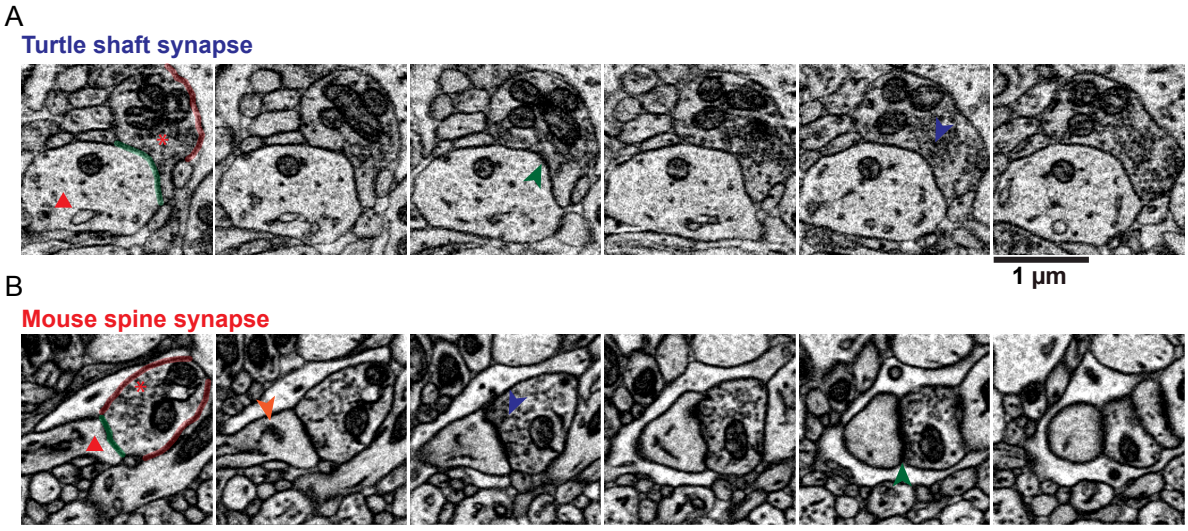

Fig. 3.2: **Synapse identification in aligned SBEM data.**
(A) Six planes imaged with SBEM with an inter-plane distance of 30 nm show cross sections of a dendritic shaft synapse in the turtle dorsal cortex L2 dataset. The presynaptic terminal (marked with an orange triangle) is touching (green shading) the postsynaptic dendrite (marked with a red triangle). The red shading marks a membrane touching another process that does not form a synaptic contact. Further criteria were used to identify synapses like the postsynaptic membrane (green arrowhead) and the clouds of vesicles (blue arrowhead) which are close to the presynaptic membrane. In **(B)**, six cross sections of a dendritic spine head synapse with an inter-plane distance of 112 nm in mouse piriform cortex L2 dataset are shown and the same criteria are marked. Note, multiple planes are needed to detect most of the mentioned criteria.

1. contact between the pre- and postsynaptic membrane

2. visible postsynaptic density [Bloom and Aghajanian, 1968]

3. multiple intracellular vesicles close to the presynaptic membrane

4. visible intracellular spine apparatus in the postsynaptic process

5. exclusion of other possible postsynaptic structures like nearby axon processes

3.5.2 Segmentation and volume reconstruction

The volume segmentation was generated using the automated volume segmentation tool SegEM (see [Berning et al., 2015]). Briefly, SegEM is based on a convolutional neural network classifier, trained for detecting membrane borders in raw EM data. After that, the intracellular space is segmented using a watershed based algorithm. The volume segmentation results were focused on minimizing merger rates resulting in rather high rates of segmentation splits. The volume segmentation result was uploaded and could be accessed by webKnossos. Each volume segment was identified by a unique segment ID (visualized by different colors) and the overlay of segmentation over the raw data could be switched on and off. The volume reconstructions were done using one of two approaches: the first was the webKnossos 'merger mode' reconstruction. The operator merged single volume segmentations (generated by SegEM) of one particular neurite of interest into one volume segmentation. The second approach 'volume mode' was performed using the computer mouse to draw the circumference of the neurite of interest in every plane reconstructing the volume of one particular neurite of interest. The acquired volume data of both volume reconstruction approaches was transferred to Amira software (Thermo Fisher, Hillsboro, USA) for visualization of the neurite of interest (isosurface representation).

3.6 Statistics

The axon and dendritic measurements were considered as being independent, normally distributed variables and error bars represent the SEM if not stated otherwise.

The boxplot data displays show the medians at the central marks and the 25th and 75th percentiles are the edges of the boxes. The whiskers of the boxplots extend to the most extreme data points. The outliers (marked as red dots) are datapoints which are 1.5 x interquartile range (IQR) (IQR = Q_3 - Q_1) above Q_3 or below Q_1 (according to [McGill et al., 1978]).

The results were marked significant when the null hypothesis was rejected at the 5% significance level.

4 Results

4.1 Overview of mouse piriform and the turtle dorsal cortex datasets

The specimens were prepared from two turtles *trachemys scripta* with a body weight of 277 g and 298 g and 28 days old mouse for 3D EM using the en-bloc staining protocol as described previously [Hua et al., 2015]. First, the cortical cross sections were imaged at low resolution to define the cytoarchitectonic boundaries of cortical layers (see Figure 4.1A and Figure 4.2A). Both in the turtle dorsal cortex (TDCtx) and the mouse piriform cortex (MPCtx), the cortical surface (pia) and layer 1 - 3 were identified based on the density of cell bodies (see Figure 4.1A and Figure 4.2A). Two 3D EM datasets were acquired from the turtle dorsal cortex L2 with a volume of 71.2 x 93.0 x 63.0 μm^3 at a resolution of 11.63 x 11.63 x 30 nm^3 and from the mouse piriform cortex L2 with a volume of 73.2 x 94.1 x 130.9 μm^3 at a resolution of 12 x 12 x 28 nm^3, which were targeted at turtle and mouse layer 2, respectively. In addition, two more datasets were acquired in the TDCtx, one dataset located within layer 3 (specimen from turtle weighing 277 g) and the middle region of layer 1 with a volume of 67.3 x 58.8 x 69.8 μm^3 at a resolution of 11.73 x 11.73 x 30 nm^3 and a volume of 70.9 x 93.7 x 121.7 μm^3 at at a resolution of 11.63 x 11.63 x 30 nm^3, respectively (see Figure 4.1A). Note that the TDCtx datasets L1 and L2 were acquired from the same specimen (turtle weighing 298 g) with the L1

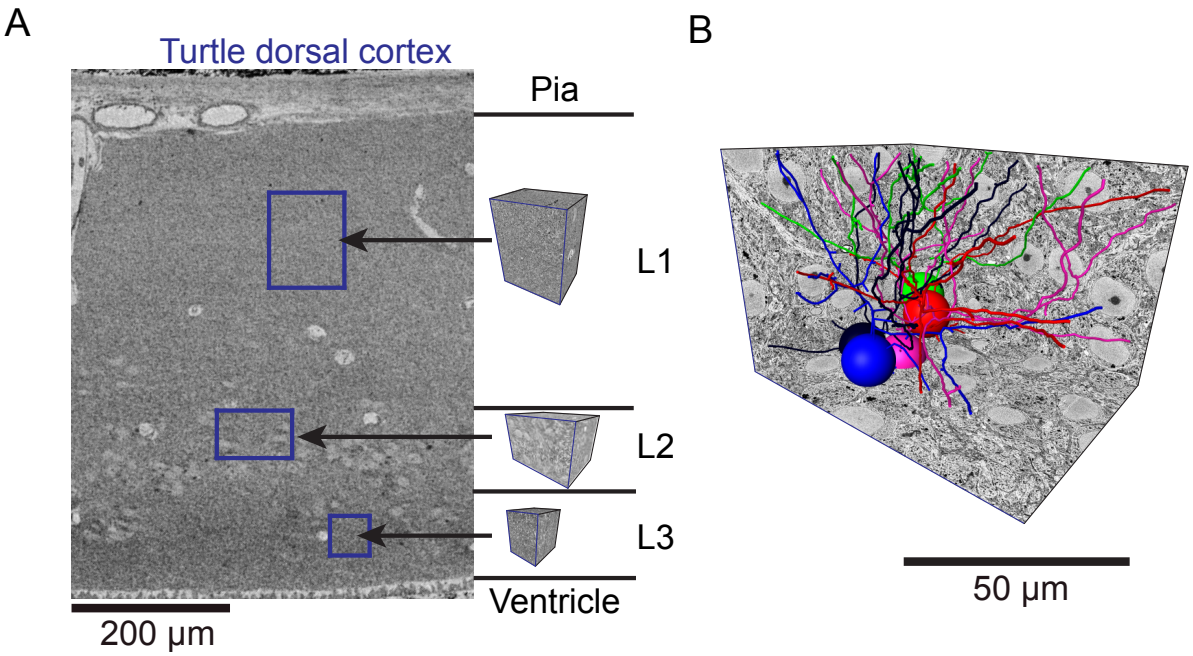

Fig. 4.1: **3D EM datasets of the turtle dorsal cortex.**
(A) Frontal view of the turtle dorsal cortex imaged with a scanning electron microscope (SEM). The three layers are indicated on the right and pia and ventricle boundaries are indicated at the upper and lower end of the image, respectively. The locations of the three datasets acquired in each layer using serial block-face electron microscopy (SBEM) are indicated by the blue boxes. On the right, the dataset boundaries are visualized. **(B)** The dataset boundaries of the turtle dorsal cortex L2 (71.2 x 93.0 x 63.0 µm^3) including 5 skeleton representations of pyramidal cells (PCs) are visualized. Cell bodies are indicated by spheres (diameter 10 µm).

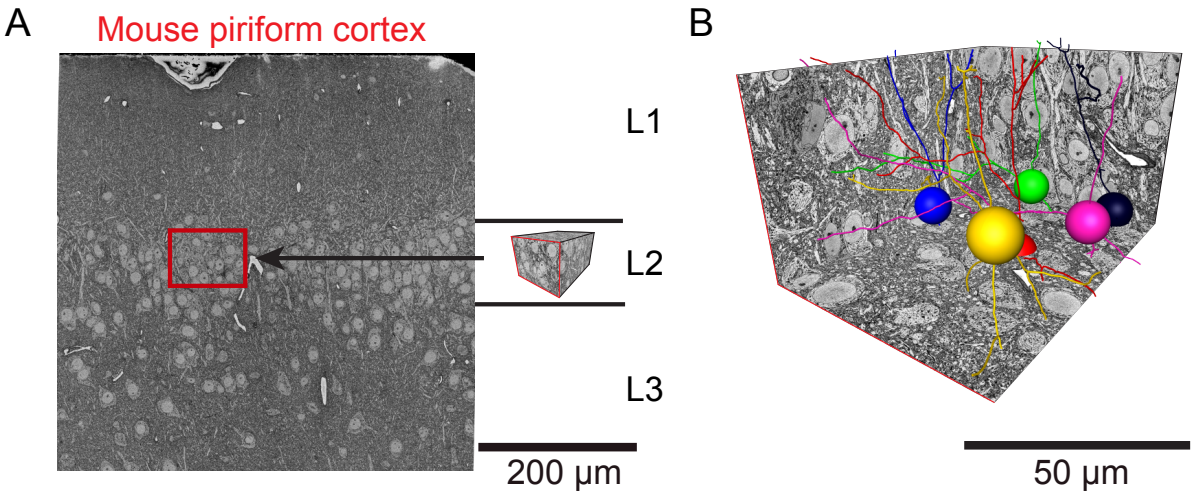

Fig. 4.2: **3D EM dataset of the mouse piriform cortex L2.**
(A) Frontal view of the mouse piriform cortex imaged with a scanning electron microscope (SEM). The three layers are indicated on the right and the cortex radial axis is oriented vertically with the pia at the upper end of the image. The location of the high-resolution dataset acquired in layer 2 using serial block-face electron microscopy (SBEM) is indicated by the red box. On the right, the dataset boundaries are indicated. **(B)** The dataset boundaries (73.2 x 94.1 x 130.9 µm^3) of the dataset including 6 skeleton representations of pyramidal cells (PCs) are visualized. Cell bodies are indicated by spheres (diameter 10 µm).

dataset located about 160 µm closer to the pia. Furthermore, lower resolution data was acquired surrounding the TDCtx L1 and L2 as well as the MPCtx L2 datasets (see Figure 3.1). The image data was then aligned into a 3D dataset and exported to

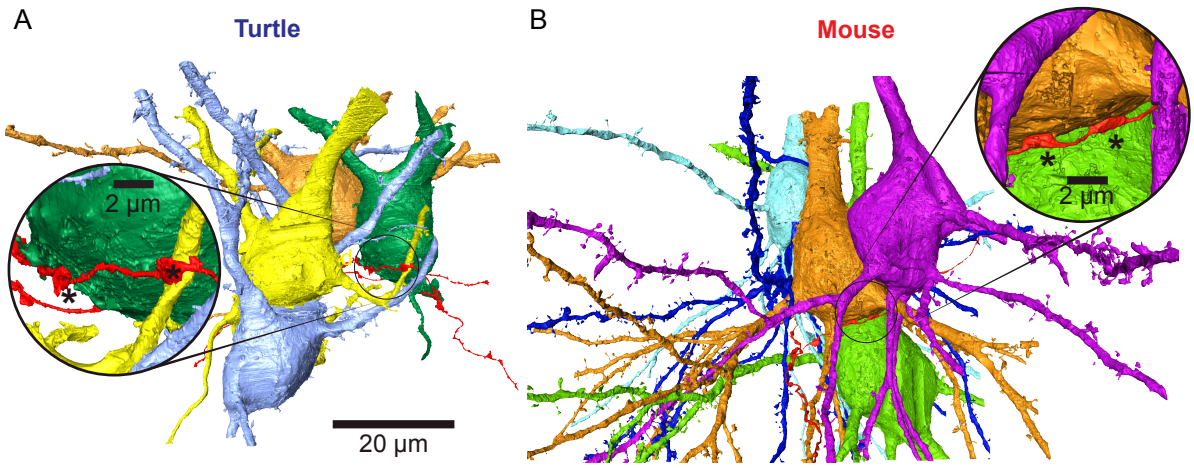

Fig. 4.3: **Volume reconstruction of pyramidal cells in the turtle dorsal and mouse piriform cortex.**
(A) Four pyramidal cells (PCs) in the turtle dorsal cortex were volume reconstructed (merger mode, see Materials and Methods: Segmentation and volume reconstruction) including the proximal parts of the basal and apical dendrites. The inset shows an axon (red isosurface) forming a synapse on a cell body (left asterisk) and a dendritic shaft (right asterisk). **(B)** Five PCs in the mouse piriform cortex were volume reconstructed and the inset shows an axon (red isosurface) forming two synapses (asterisks) on the same cell body (orange isosurface). Note that the mouse PCs posess single apical dendrite while PCs in turtle possess several apical dendrites.

webKnossos [Boergens et al., 2017] for skeleton annotation and volume reconstruction (see Figure 4.3).

4.2 Identification of subcellular structures

The first analysis was focused on postsynaptic subcellular structures, e.g. cell body, apical dendrite (see Figure 4.4) and axon initial segment (AIS) (see Figure 4.5).

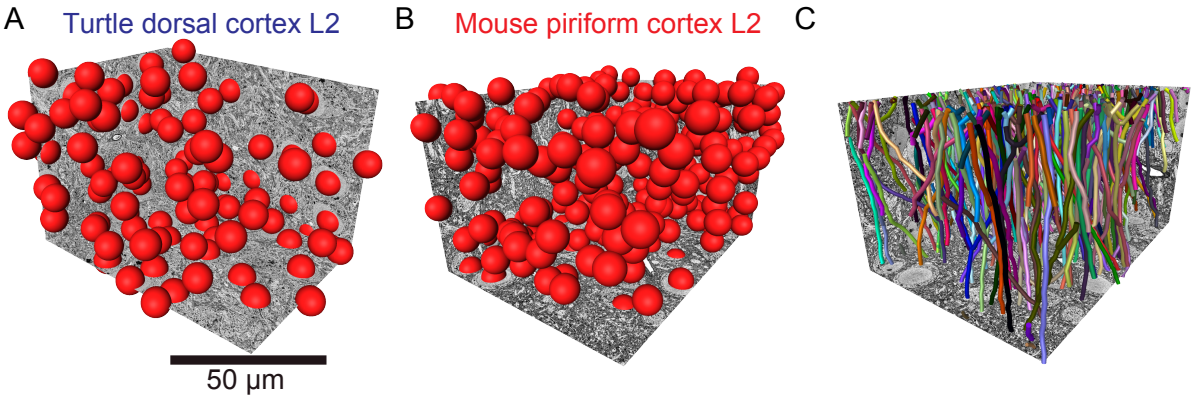

Fig. 4.4: **Postsynaptic subcellular structure identification.**
(A) All cell bodies (n = 102) in the turtle dorsal cortex L2 were annotated manually. The locations are represented by the red spheres (diameter 10 µm). **(B)** The same annotation as in **(A)** was done in the mouse piriform cortex (MPCtx) L2 (n = 206). **(C)** All apical dendrites (n = 184) in the MPCtx L2 were reconstructed manually and are represented as tubes (diameter 2.5 µm).

4.2.1 Cell body diameter

The cell bodies were identified manually in both mouse and turtle L2 (see Figure 4.4A and B). Then, the skeleton of the associated dendrites were reconstructed. For a subset of cell bodies (n = 10) the diameter was approximated by using the largest extent of the cell body in each of the three cardinal axes, resulting in 15.57 ± 0.75 µm (mean ± standard deviation (SD)) and 16.32 ± 0.75 µm (mean ± SD) for mouse and turtle, respectively.

Table 4.1: **3D electron microscopy data and reconstruction in mouse and turtle.**

	TDCtx L1	**TDCtx L2**	**TDCtx L3**	**MPCtx L2**
X-Dimension [µm]	70.9	71.2	67.3	73.2
Y-Dimension [µm]	93.7	93.0	58.8	94.1
Z-Dimension [µm]	121.7	63.0	69.8	130.9
Reconstructed axon path length [mm]	5.37	40.53	8.34	31.49
Reconstructed dendritic path length [mm]	0.12	43.80	3.91	65.56
Cell bodies	5	102	1	206
Identified synapses	936	5249	1055	3051

4.2.2 Axon initial segment identification

The identification of axon initial segments (AISs) was based on several criteria. First, the AISs of pyramidal cells were reported to exit the cell body on the pia-averted side in both turtle dorsal and the mouse piriform cortex [Ramón y Cajal, 1952]. Second, the AISs did not form spine-like structures, however, studies reported spine-like appendages [Kosaka, 1980] occasionally, which was observed both in the turtle dorsal cortex and the mouse piriform cortex dataset as well as in the mouse primary somatosensory 'barrel' cortex S1 (personal communication with Anjali Gour and Philip Laserstein). Third, the AISs were also identified by observing each neurite process exiting the cell body and excluding those showing clear structural features of dendrites, e.g. postsynaptic dendritic spine heads or multiple proximal branching. Additionally, the beginning of myelination or forming of presynaptic structures of presumable AIS processes was used as a marker

for AISs. Finally, the cytoskeleton of AISs were structurally different compared to

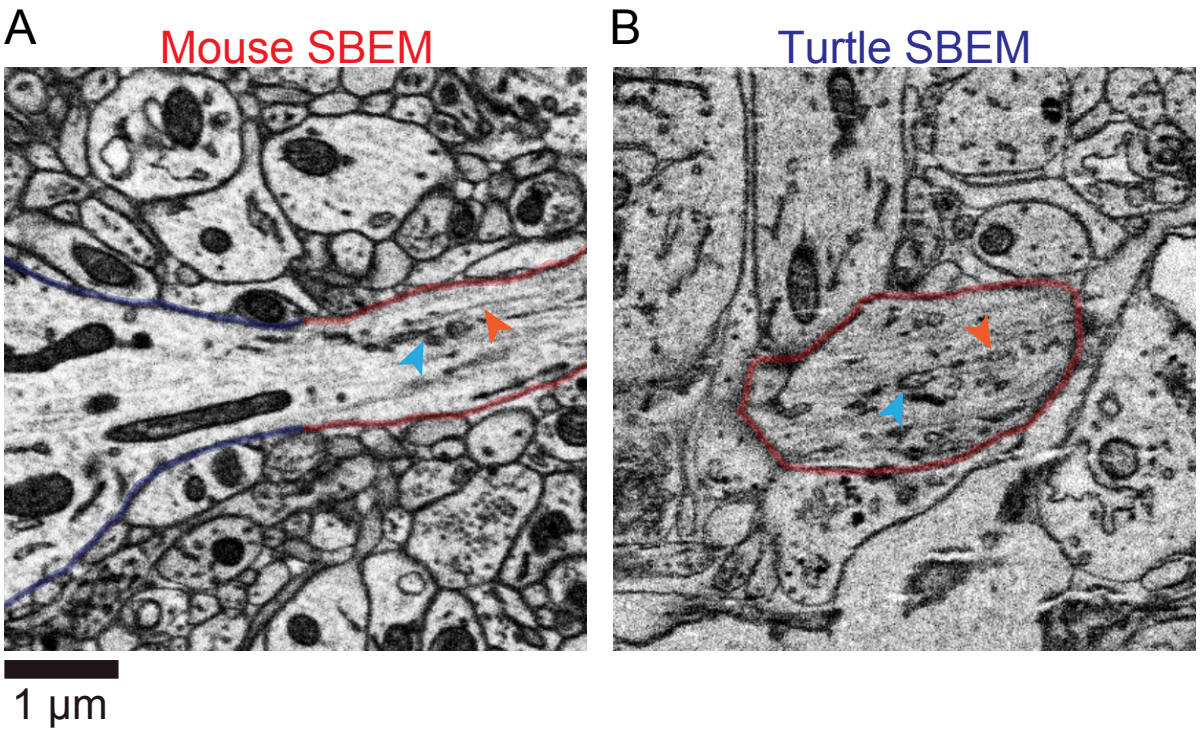

Fig. 4.5: **Axon initial segment identification in SBEM data of the turtle dorsal and mouse piriform cortex L2.**
Two axon initial segments (AISs) in mouse piriform **(A)** and the turtle dorsal cortex **(B)** were imaged with serial block-face electron microscopy (SBEM). The cell body membranes are shaded in blue and the axon initial segment (AIS) membranes are shaded in red. Among other criteria, the intracellular structures - like the fasciculation of microtubules (blue arrowhead) which are linked by cross-bridges (orange arrowhead) described in [Kosaka, 1980] - were used to detect and identify AISs.

dendrites. In particular, the fasciculation of microtubuli [Peters et al., 1968] was used to identify AISs which were passing through the dataset and whose cell bodies were not contained within the datasets boundaries (see Figure 4.5). A total of 65 and 95 AISs were identified in the TDCtx L2 and the MPCtx L2, respectively.

4.2.3 Apical dendrite identification

The apical dendrites were identified manually either by reconstructing the dendritic tree starting from an identified cell body (the dendrite exiting the cell body at the pia-facing

side) or by searching for large diameter dendrites passing through the dataset in the pia to white matter axis. In the MPCtx L2 a total of 184 apical dendrites out of which 124 apical dendrites were identified with their cell body within the dataset boundaries (see Figure 4.4). This identification analysis was not possible in the TDCtx due to the morphology of turtle pyramidal cells possessing multiple apical dendrites. These did not show a constant orientation parallel to the pia-to-ventricle axis (see morphology in Figure 4.3 and Figure 2.4).

4.3 Dendritic spine head and shaft innervation

Next, the turtle cortex was investigated for axonal specificity to dendritic spine heads and dendritic shafts. Therefore, several synapses formed on dendritic spine heads and dendritic shafts were identified in each dataset. These synapses were used as seeding points identifying presynaptic axons which were consecutively skeleton-reconstructed (see Table 4.2). Next, for each reconstructed axon all synapses were detected manually and labelled with the class of postsynaptic subcellular structure, e.g. cell body, AIS, etc. Figure 4.6A and Figure 4.7A show a spiny dendrite in each dataset from mouse L2 and turtle L2 together with two innervating axons that were identified by establishing a synapse onto a dendritic spine head. In mouse, the spine-seeded axon is innervating several additional dendritic spine heads. In turtle, however, the spine-seeded axon is innervating both dendritic spine heads and shafts. Figure 4.6B and Figure 4.7B show examples of axons in mouse and turtle, respectively, which were identified via the synapses formed onto the dendritic shafts (grey isosurface). In the mouse dataset, the identified and reconstructed axon exclusively forms synapses onto dendritic shaft locations. The turtle axon, however, forms synapses on dendritic shaft and spine head locations.

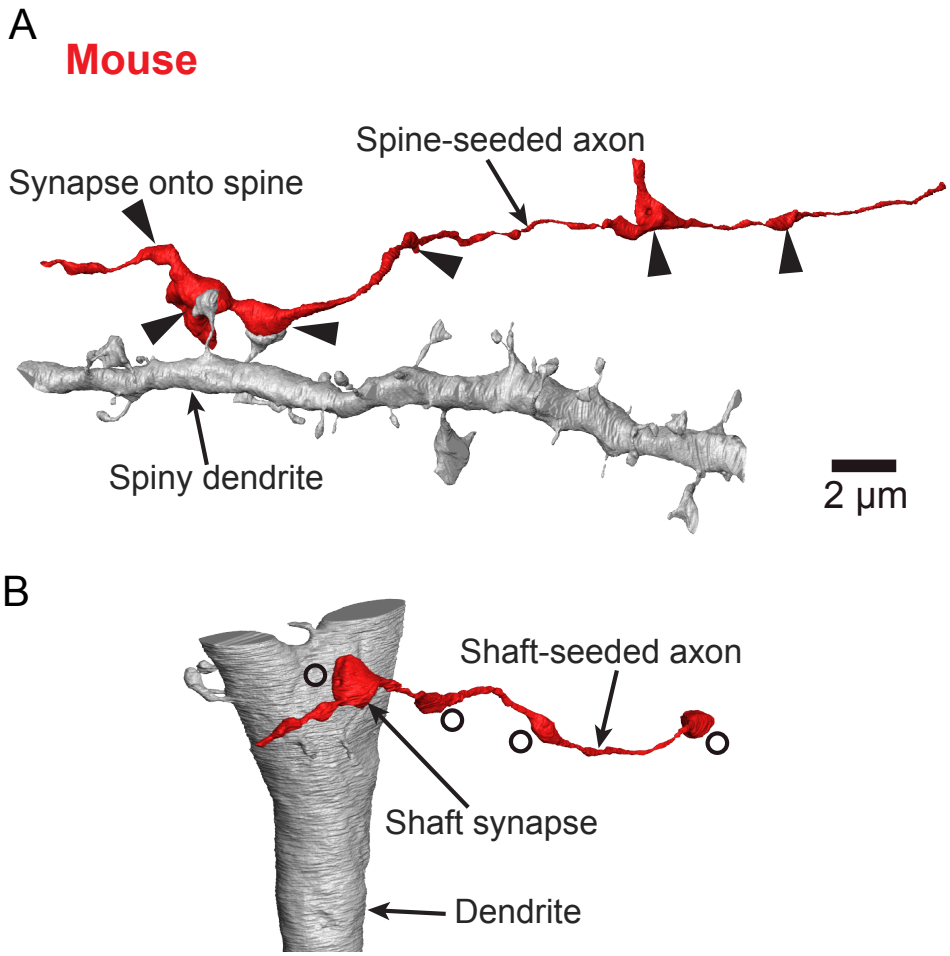

Fig. 4.6: **Volume reconstruction of axons and dendrites in the mouse piriform cortex L2.**
(A) Volume reconstructions (volume mode, see subsection 3.5.2) of a spiny dendrite (grey isosurface) and an axon (red isosurface) identified by the two synapses formed on the dendrite's spine heads in the MPCtx L2. The arrowheads point to the locations of the detected dendritic spine head synapses. **(B)** Volume reconstructions of an apical dendrite (grey isosurface) and an axon (red isosurface) identified by the synapse formed on the dendritic shaft (grey isosurface) in the same dataset as **(A)**. The circles mark the locations of detected dendritic shaft synapses.

Figure 4.8A shows the quantitative result and the dichotomy between axons targeting dendritic spine heads and shafts as found in mammals appears to be absent in the turtle cortex. In the mouse piriform cortex L2, 19.6% of all axons (n = 147) made less than 25% of their synapses onto dendritic spine heads and 65.4% of axons made at least 75% of their synapses onto dendritic spines. In contrast, the distribution shows a lower specificity in turtle with approximately half their axons neither prefering nor avoiding spine head synapses. 87.75 ± 2.72% (mean ± SD) of axons are below the 25th or above the 75th percentile in mouse, compared to 43.67 ± 2.37% (mean ± SD) in turtle (n = 435) (see Figure 4.8C, $p<10^{-2}$, bootstrapping test). Similar results were obtained from TDCtx L1 and L3 datasets (24.45 ± 5.64% (mean ± SD) and 30.42 ± 4.39% (mean ± SD) of axons are below the 25th or above the 75th percentile in TDCtx L1 (n = 58) and L2 (n = 114), respectively, see Figure 4.8D, p>0.3, two sample t-test).

Although, more than half of the axons in the turtle cortex do neither prefer nor avoid innervating dendritic spine heads, it seems that the remaining axons do behave similarly specific as the axons measured in the mouse cortex. This analysis, however, might be influenced by the number of synapses each axon formed within the datasets. With smaller number of synapses which were identified in each axon there is a growing tendency of describing an axon to be specific for innervating or avoiding dendritic spine heads. A simple example would be an axon forming a single synapse onto a dendritic spine head. This axon would be described and classified as an axon having 100% of its synapses formed on dendritic spine heads and is therefore specifically innervating dendritic spine heads.

Since the turtle datasets were mostly smaller (see Table 4.1), the described bias was evaluated: the number of synapses of each axon was counted and the result is shown in Figure 4.9. In fact, the average number of synapses per axon was

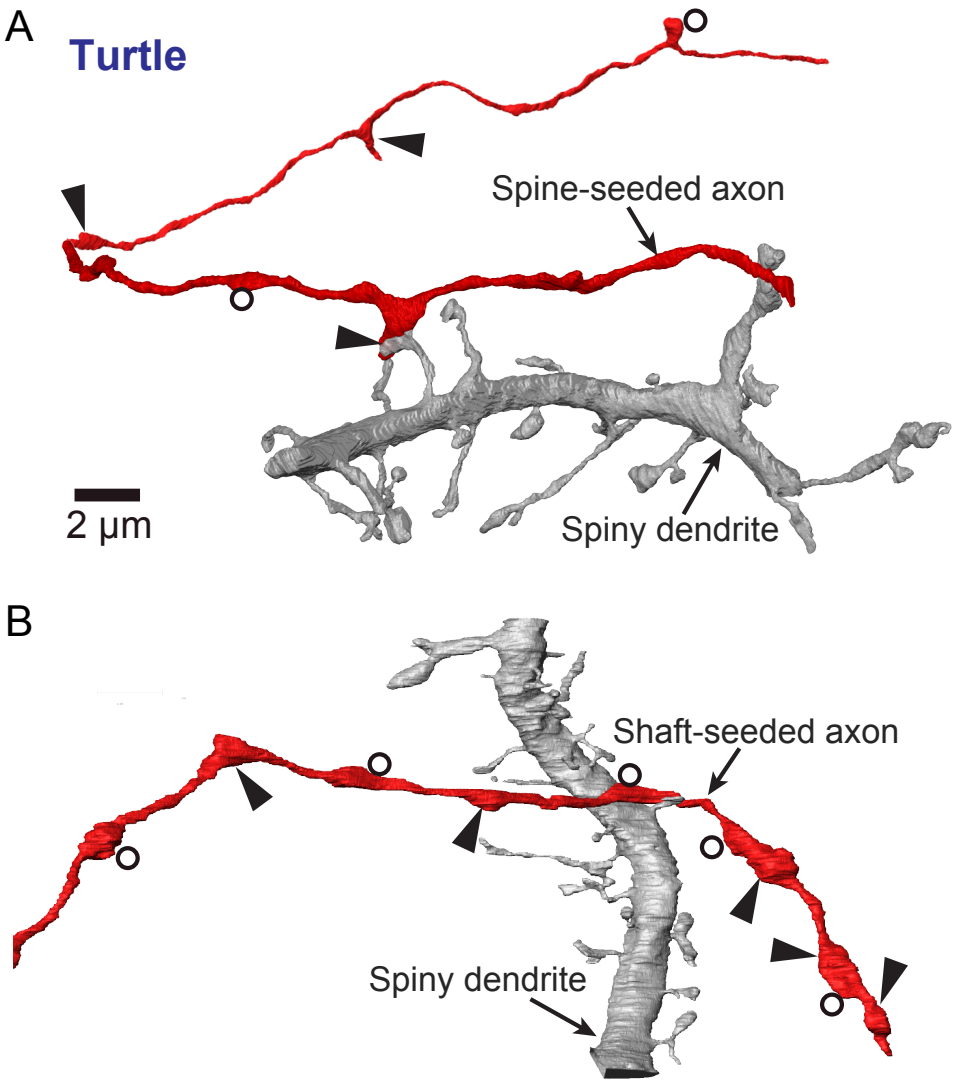

Fig. 4.7: **Volume reconstruction of axons and dendrites in the turtle dorsal cortex L2.**
(A) Volume reconstructions (merger mode) of a spiny dendrite (grey isosurface) and an axon (red isosurface) identified by the synapse formed on the dendrite's spine head in the TDCtx L2 dataset. The arrowheads point to the locations of detected dendritic spine head synapses and the circles mark the locations of the detected dendritic shaft synapses. **(B)** Volume reconstructions of a spiny dendrite (grey isosurface) and an axon (red isosurface) identified by the synapse formed on the dendritic shaft (grey isosurface) in the same dataset as **(A)**.

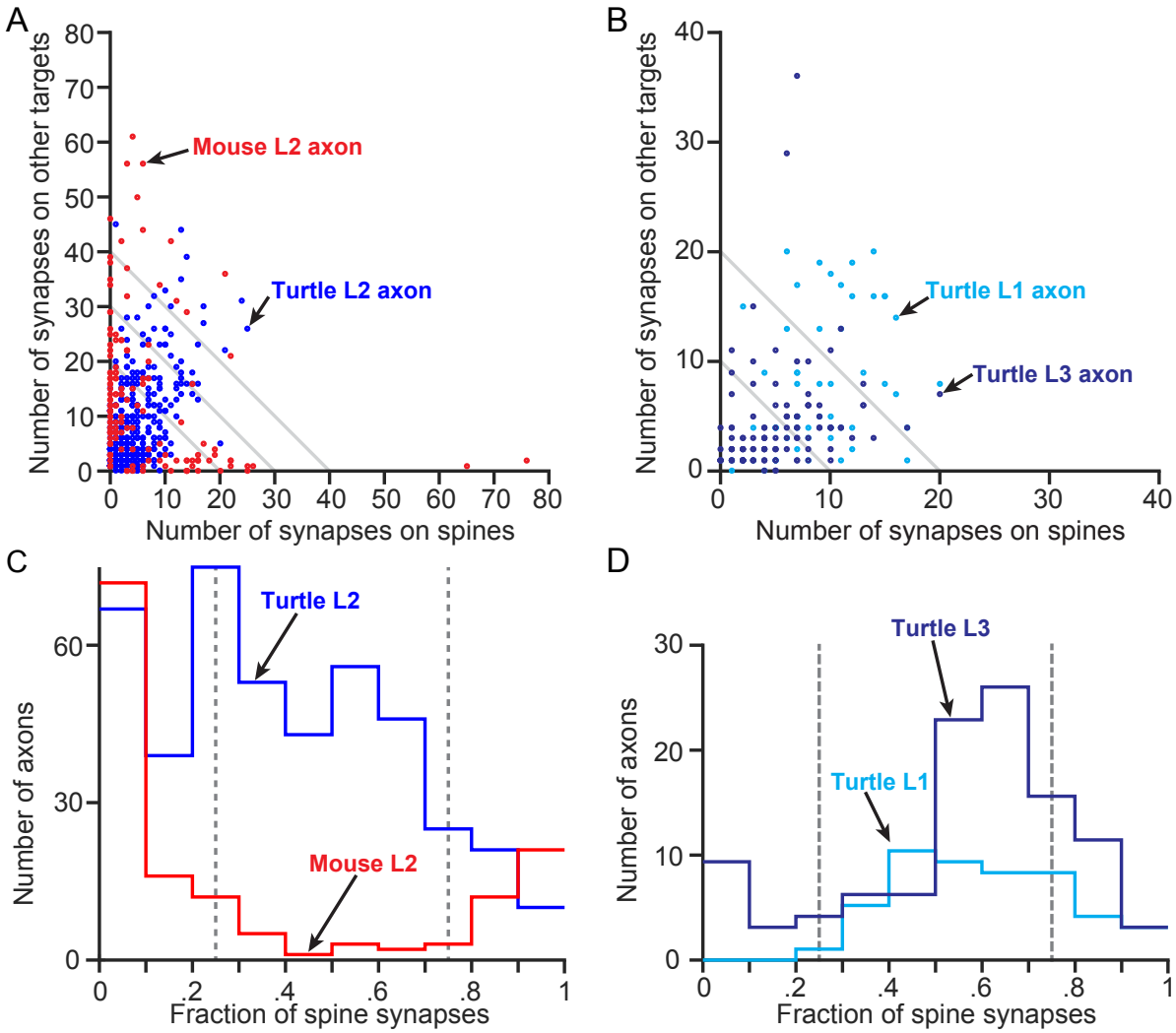

Fig. 4.8: **Dendritic spine head and shaft innervation in both the mouse piriform and turtle dorsal cortex.**

(A) Scatter plot of absolute numbers of synapses formed on dendritic spine heads (x-axis) and other targets (y-axis) of single axons in mouse piriform (3025 synapses, 147 axons) and the turtle dorsal cortex L2 (5238 synapses, 435 axons). Grey lines indicate the boundaries of 20, 30 and 40 synapses (from left to right). **(B)** Scatter plot as in **(A)** for axons reconstructed in the turtle dorsal cortex L1 (937 synapses, 58 axons) and L3 (1054 synapses, 114 axons). **(C)** Histogram of the axons in **(A)** shows the fraction of synapses on dendritic spine heads. **(D)** Histogram shows the result for the axons in **(B)**. Dashed lines indicate the 25th- and 75th-percentile boundaries.

significantly lower in turtle L2 (12.04 ± 10.33 (mean ± SD)) compared to mouse L2 (20.58 ± 16.47 (mean ± SD)). The results in turtle L3 (9.25 ± 6.89 (mean ± SD)) and L1 (16.16 ± 8.93 (mean ± SD)) yielded a similar result. The larger dataset volumes most likely covered more axon path length and therefore, larger numbers of synapses per axon were counted in the turtle dorsal cortex L1 and the mouse piriform cortex L2. In addition, the axon path length was measured for each axon and the synapse

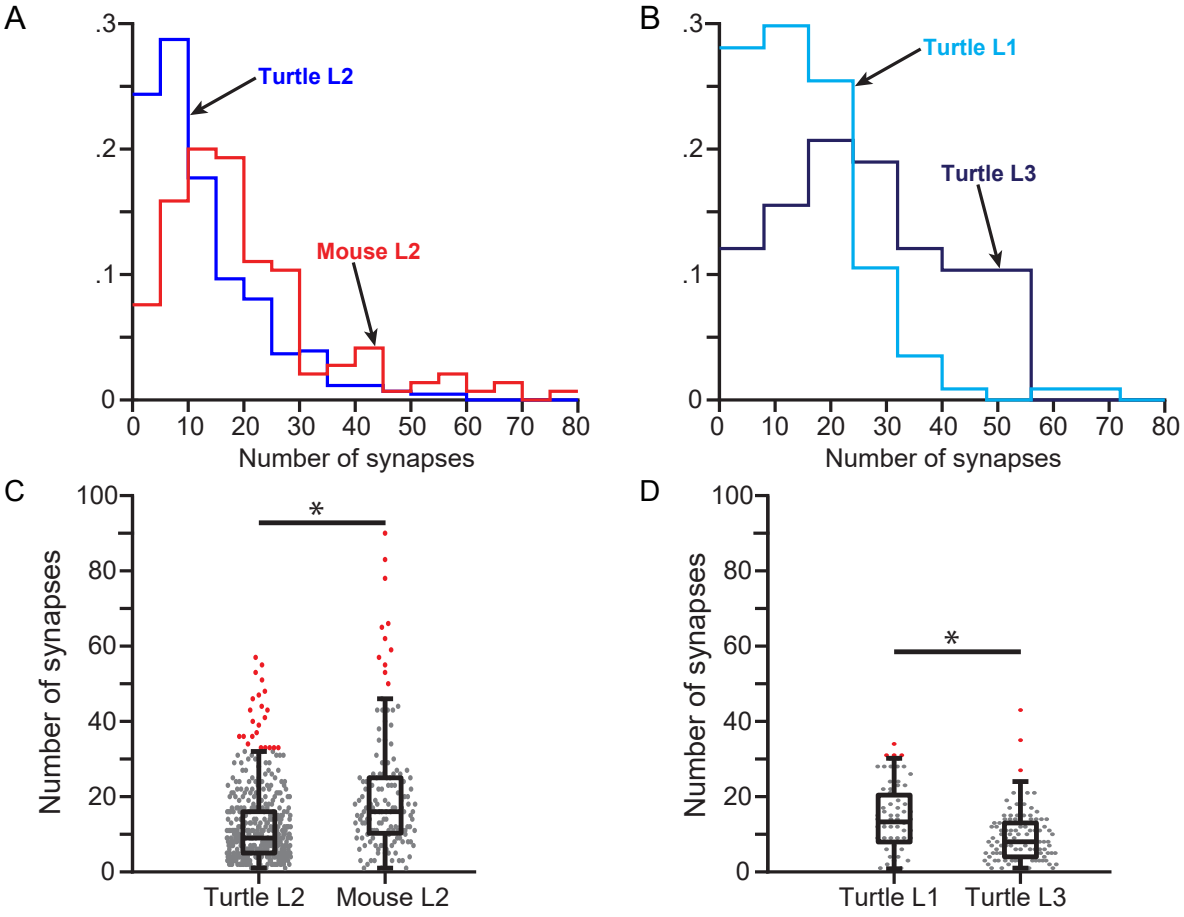

Fig. 4.9: **Number of synapses per axon in the mouse piriform and turtle dorsal cortex.**
(A) Histogram of absolute numbers of synapses for each reconstructed axon in the mouse piriform and turtle dorsal cortex L2. **(B)** Histogram of reconstructed axons of turtle dorsal cortex layers 1 and 3. **(C)** Box plot of mouse and turtle L2 axons shows a significant difference in the average number of synapses per axon (two sample t-test, $p<10^{-5}$). **(D)** Box plot of average number of synapses per axon for turtle L1 and L3 also shows a significant difference (two sample t-test, $p<10^{-5}$). Grey dots represent single measurements.

densities were calculated (see Figure 4.10). In both datasets, turtle L2 and mouse L2 axons show comparable densities (0.15 ± 0.10 µm^{-1} (mean ± SD) in mouse L2 and 0.14 ± 0.08 µm^{-1} (mean ± SD) in turtle L2, two sample t-test, p>0.24).

This result supported the hypothesis that the larger volume of the MPCtx dataset leads to higher synapse numbers per axon. To account for axons with small numbers

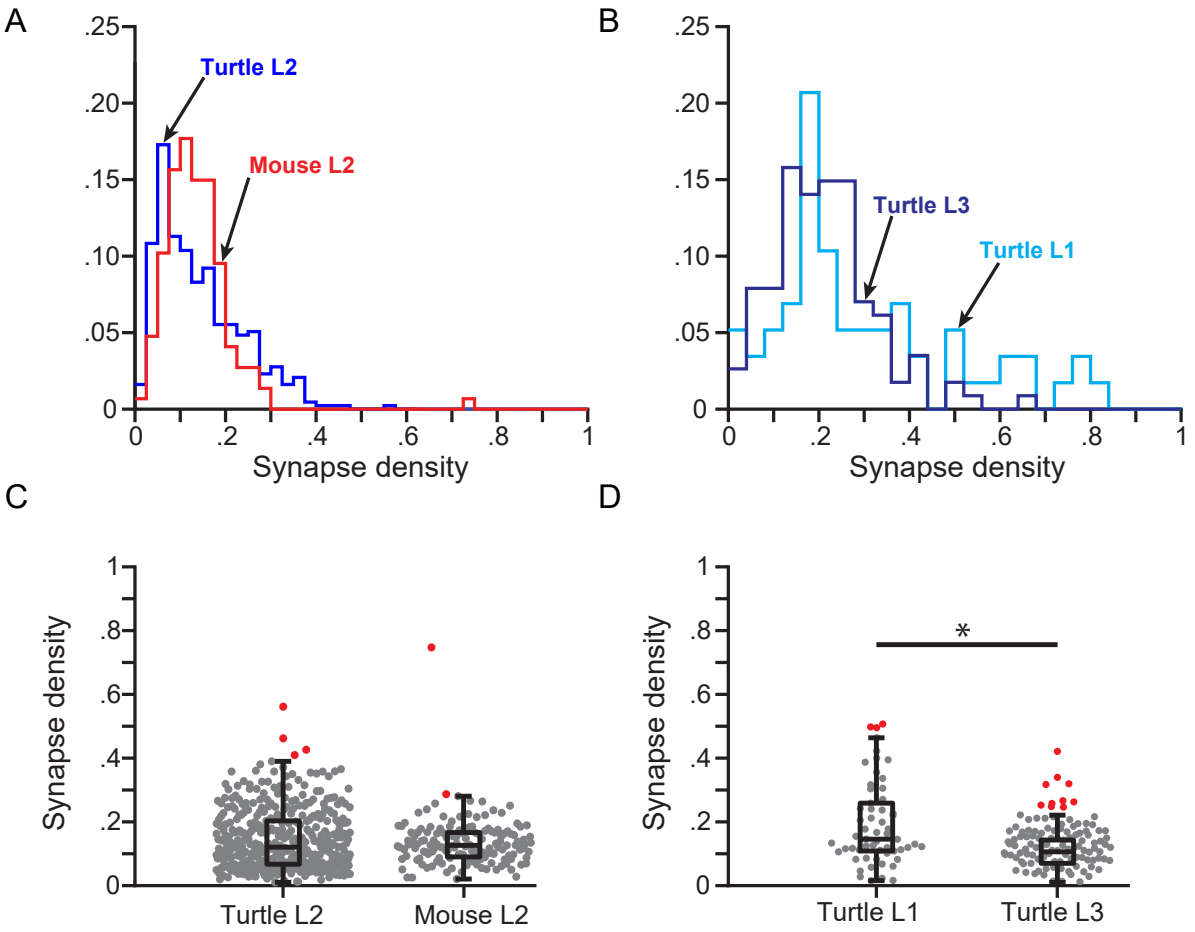

Fig. 4.10: **Axon synapse density in the mouse piriform and turtle dorsal cortex.**
(A) Histogram of synapse densities for each reconstructed axon in mouse piriform and the turtle dorsal cortex L2. **(B)** Histogram of reconstructed axons in turtle dorsal cortex layers 1 and 3. **(C)** Box plot of mouse and turtle L2 axons does not show a difference in synapse densities. **(D)** Box plot of turtle L1 and L3 axons indicates that synapse densities differ slightly. Grey dots represent single measurements.

of synapses, the histogram presented in Figure 4.8 was altered by only including

axons containing at least 11 synapses (see Figure 4.11). In turtle L2, the fraction of axons forming more than 75% of their synapses onto dendritic spine heads dropped substantially from 11.03% to 2.65%. The fraction of turtle L2 axons forming less than 25% of their synapses onto dendritic spine heads remained stable (35.86% including all axons and 39.15% only including axons containing 11 or more synapses). Regarding mouse L2, the fraction of axons having less than 25% or more than 75% of their synapses on dendritic spine heads remained stable (87.75% including all axons and 85.45% only including axons containing 11 or more synapses). After bootstrapping the axon population, the average sum of axons below the 25th and above the 75th percentile in mouse L2 was 85.90 ± 2.76% (mean ± SD) (n = 110) compared to 40.81 ± 3.34% (mean ± SD) in turtle L2 (n = 189) (see Figure 4.11A, two sample t-test, $p<10^{-5}$). The correction removed most of the axons in turtle L2 which were considered to be specific for dendritic spine heads while the overall fraction of axons which were considered to be specific remained stable.

Interestingly, two axons in turtle L3 had a high number of synapses (35 and 43 synapses) and also formed more than 75% of their synapse onto dendritic shafts (see Figure 4.8B). Although, axonal specificity for dendritic shaft or dendritic spine head synapses might not be the prominent feature in turtle cortex, there might be a small population of axons that mirror the well-established dichotomy of mammalian cortical axonal specificity.

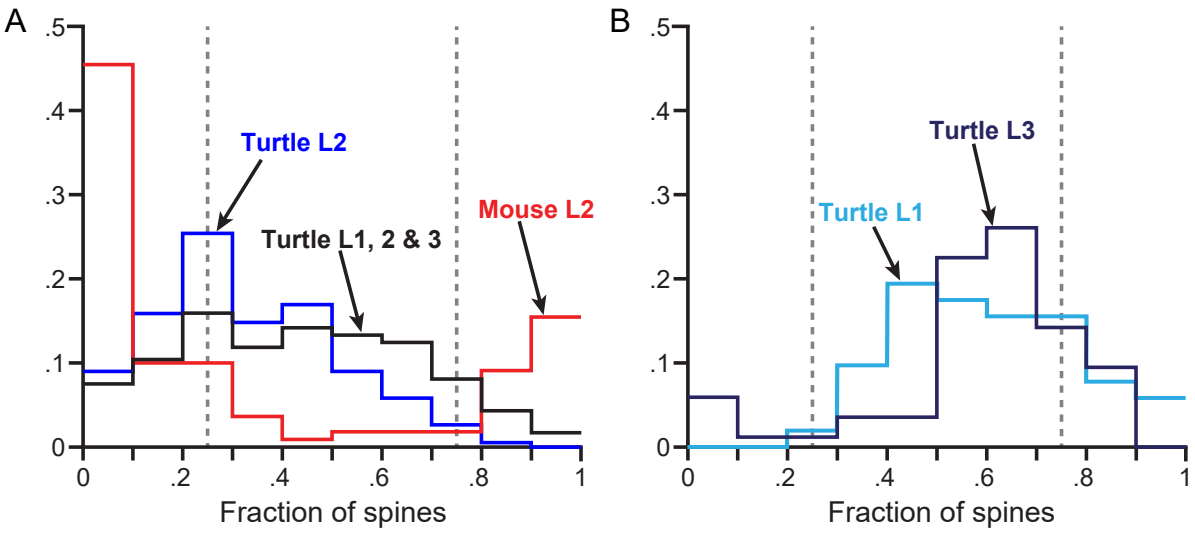

Fig. 4.11: **Normalized histogram of dendritic spine head and shaft innervation in mouse piriform and the turtle dorsal cortex.**
Histogram of single axon synapse fractions formed on dendritic spine heads. Only axons with at least 11 synapses were included. **(A)** Histogram of turtle L2 (blue, 3951 synapses, 189 axons), mouse L2 (red, **(A)**, 2803 synapses, 110 axons) and L1, 2 and 3 of turtle combined (black). **(B)** Histogram of turtle L1 (bright blue, 846 synapses, 42 axons) and turtle L3 (dark blue, 689 synapses, 53 axons). Dashed lines indicate the 25th- and 75th-percentile boundaries.

4.4 Synapse volume density and axon wiring density

The cortical pyramidal cells in both species show lower densities of dendritic spine heads proximally compared to their distal parts of dendrites. A difference in dendritic spine heads per volume in turtle L2 and mouse L2 might have an effect on the previous analysis. Next, the datasets were investigated whether the lack of dendritic spine head innervation in turtle L2 might be caused by a lower occurence of dendritic spine heads per volume compared to mouse L2. To examine this, five cubic volumes with an edge length of 3 µm were randomly selected and all synapses within the datasets mouse L2 and turtle L2 were annotated and labelled by the class of postsynaptic partner (dendritic spine head and shaft). In addition, all axon processes were identified and skeleton-reconstructed to calculate the axon wiring density. The result is shown in Figure 4.12 indicating a substantial difference in the synapse volume density.

In mouse L2 the synapse volume density is on average 0.92 ± 0.06 µm^{-3} (mean ± SD)

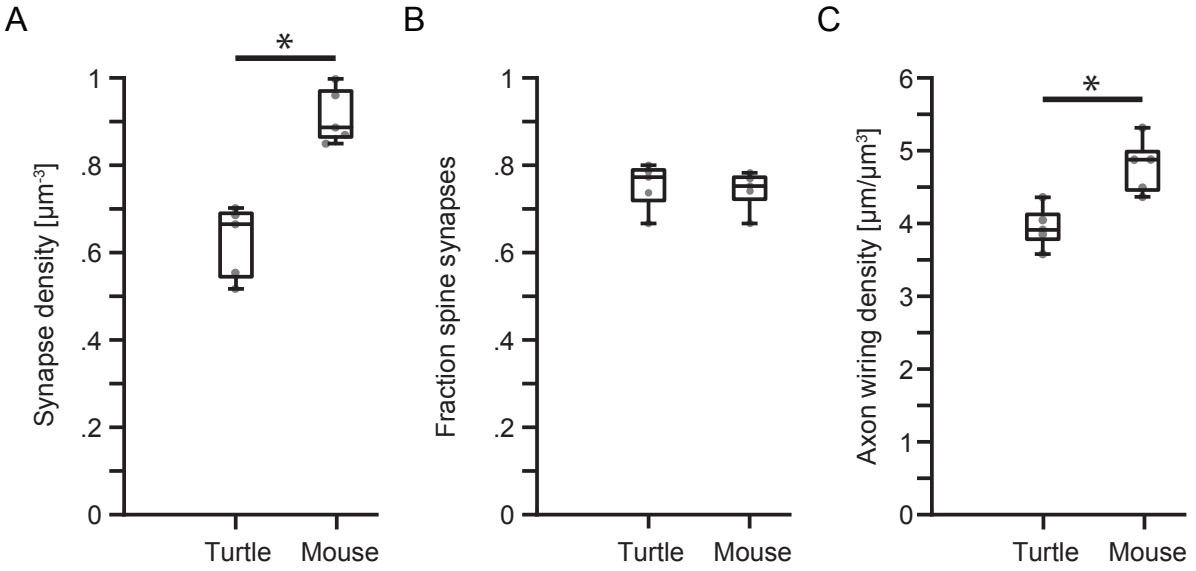

Fig. 4.12: **Volume density of synapses and total axonal wiring path length.** **(A)** Synapse volume densities in mouse and turtle differ significantly (two sample t-test, $p<10^{-3}$). **(B)** Fractional occurrence of dendritic spine head synapses in mouse and turtle is comparable (two sample t-test, $p>0.75$). **(C)** Axon wiring density in mouse and turtle differ significantly (two sample t-test, $p<10^{-2}$). Grey dots represent single measurements.

and in turtle L2 the density is significantly lower 0.63 ± 0.08 µm^{-3} (mean ± SD) (two sample t-test, p<10^{-3}). The ratio of dendritic spine head and shaft synapses, however, is similar (0.63 ± 0.08 µm^{-3} (mean ± SD), two sample t-test, p>0.75). Since the measured synapse densities of mouse and turtle L2 axons (see Figure 4.9A+C) were comparable, one explanation might be that turtle cortex either possesses lower absolute number of axons or does not innervate the volume as dense as in the mouse piriform cortex. In Figure 4.12C the measured axon wiring density is shown and, in fact, turtle axons in L2 show a significantly lower wiring density compared to mouse L2 axons (4.79 ± 0.37 µm^{-3} (mean ± SD) in mouse L2 versus 3.95 ± 0.29 µm^{-3} (mean ± SD) in turtle L2, two sample t-test, p<10^{-2}).

This result might explain the general lower volume densities of synapses in the turtle dorsal cortex. Since the relative fractions of dendritic spine synapses are comparable, it does not explain the observation that the turtle dorsal cortex lacked axons preferring dendritic spine synapse locations compared to the mouse piriform cortex (see Figure 4.11).

Lack of axonal specificity in TDCtx confirmed between individual turtles Due to monetary and time constraints with regard to acquisition and annotation time (see Introduction: Connectomics and Figure 2.7), the application of 3D EM techniques in neuroscience often lacks the ability to confirm findings in more than one individual. Therefore, studies are rarely able to exclude a potential effect caused by an individual animal. Recent studies in the field successfully confirmed their findings in at least two animals (see [Schmidt et al., 2017, De Vivo et al., 2017]).

Here, the turtle L3 dataset was acquired from a different brain than the datasets acquired from turtle L2 and L1. Therefore, the comparative analysis, e.g. axon dendritic spine head and shaft synapse distribution, is also a comparison between two individual TDCtxs continuing the trend to confirm findings within species. The observation of

the turtle dorsal cortex lacking specific axons for dendritic spine heads and shafts was therefore replicated in a second individual Figure 4.11 as well as the axon synapse density (0.14 ± 0.08 µm^{-1} (mean ± SD) in turtle L2 versus 0.13 ± 0.07 µm^{-1} (mean ± SD) in turtle L3, two sample t-test, $p>0.94$). These results which were reproduced in another animal might be seen as a confirmation that these findings are not necessarily an effect caused by an individual animal.

4.5 Subcellular innervation

Next, the turtle cortex was investigated for axonal specificity to postsynaptic subcellular targets. The cortical layer 2 in both species contains various subcellular structures, e.g. AISs, cell bodies or apical dendrites that are known to be specifically innervated by classes of interneurons (see AIS-specific innervation by axons of Chandelier cell [Somogyi, 1977]). Therefore, several synapses were identified by their postsynaptic target class, e.g. cell body, apical dendrite and AIS. These synapses were used as seeds to identify axons which were then skeleton-reconstructed (see Table 4.2). As described previously, all synapses formed by these axons were annotated and labelled with the postsynaptic target class.

Table 4.2: **Number of axons seeded from postsynaptic subcellular structures.** The number of synapses for each axon population is given in parenthesis.

Seeding origin	**TDCtx L1**	**TDCtx L2**	**TDCtx L3**	**MPCtx L2**
Cell body	NA	28 (406)	NA	20 (431)
Axon initial segment (AIS)	NA	304 (3249)	NA	24 (508)
Apical dendrite	NA	NA	NA	21 (410)
Dendritic spine head	21 (364)	31 (391)	22 (317)	21 (420)
Dendritic shaft	21 (432)	23 (516)	23 (335)	20 (387)

To reduce the bias which was introduced by the process of selecting the axons, each axon's seed synapse (on cell bodies, axon initial segments, apical dendrites, dendritic shafts and spine heads) was discarded and the remaining synaptic innervations onto these postsynaptic target structures were reported. Each postsynaptic target class gave rise to one axon population.

The number of axons in each population is given in Table 4.2. The results are given by the connectivity matrix (see Figure 4.13) which might already indicate that there is a block-sorted innervation profile in mouse L2 that seems to be absent in turtle L2. Quantitatively, this analysis shows axon subcellular innervation profiles for mouse cortex (see Figure 4.14A): axons identified by their first synapse onto axon initial segments did so again with 86.3 ± 29.2% (mean ± SD) of their synapses (described as Chandelier axons by [Somogyi, 1977]). The cell body seeded axons had a probability of 46.8 ± 22.7% (mean ± SD) to innervate other cell bodies; axons identified by their first synapse onto an apical dendrite did so again with a probability of 25.1 ± 14.0% (mean ± SD). In the turtle connectome however, the axon populations seeded from each postsynaptic structure class were indistinguishable from each other (see ANOVA p-values in Figure 4.14). In the turtle L2 dataset, all AIS were reconstructed, all synapses formed on them were identified and these synapses were used to identify all axons forming at least one synapse on an AIS. No AIS specific axons could be found (none out of 304 reconstructed axons in the turtle dataset showed an AIS innervation preference). Similarly, the cell body specific axons were absent in turtle L2 showing a probability of 9.9 ± 14.2% (mean ± SD) to find another cell body innervating synapse. Furthermore, the dichotomy of axons targeting dendritic spine heads or shafts stayed consistent in mouse L2 (see grey and black line in Figure 4.14). The axons seeded from dendritic shaft synapses were again innervating dendritic shaft locations with a probability of 52.2 ± 20.3% (mean ± SD) and the probability to find dendritic spine

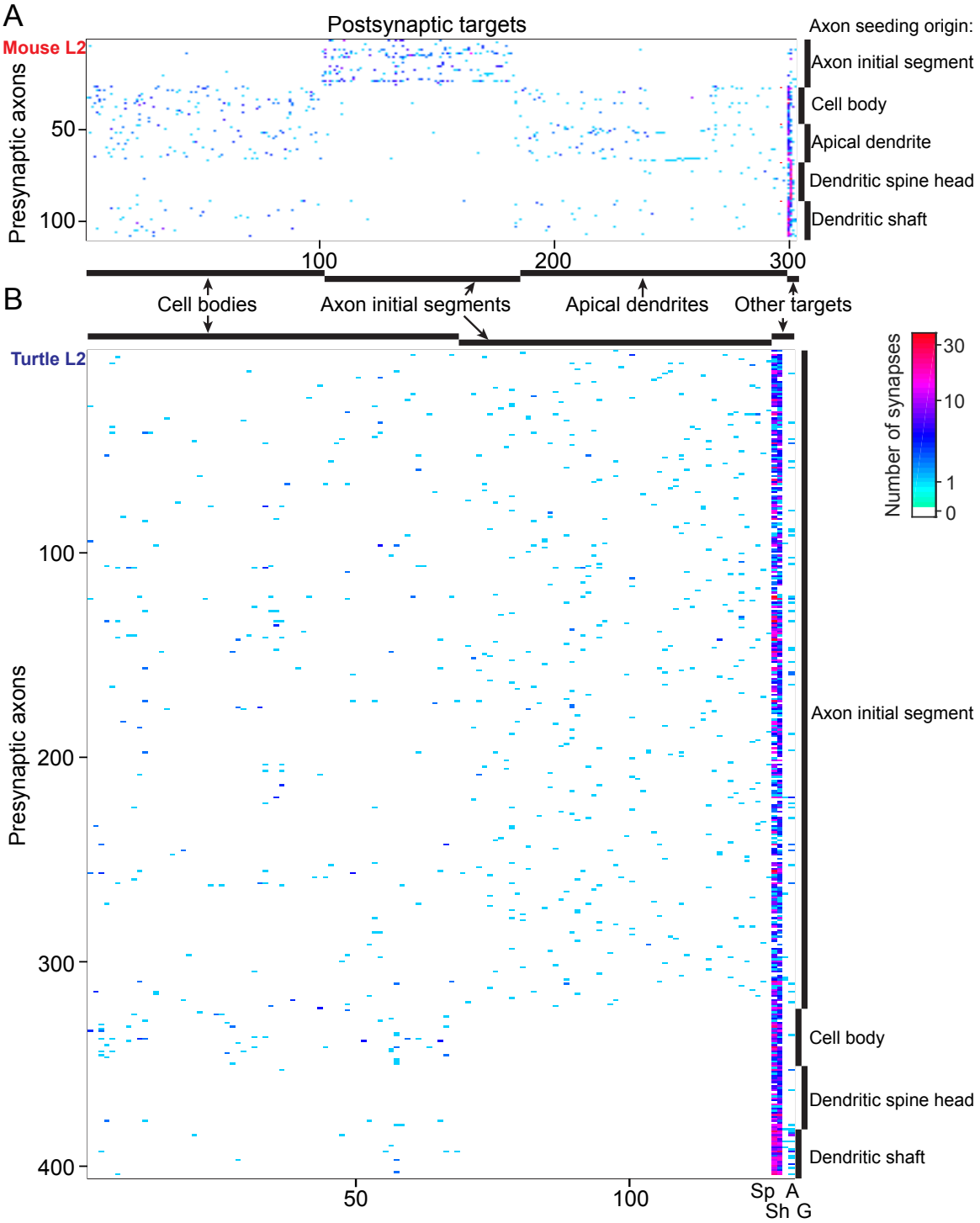

Fig. 4.13: **Sparse connectome of the mouse piriform and turtle dorsal cortex L2.**

Each row represents a unique axon (seeding origin is indicated on the right). Each column represents a unique postsynaptic process (postsynaptic structure class are indicated between the matrices). The last four columns labeled as 'Other targets' show the summed synapses formed on dendritic spine heads (Sp), shafts (Sh), axons (A) and glia (G) processes, respectively. **(A)** and **(B)** show all reconstructed axons in mouse piriform and the turtle dorsal cortex L2, respectively.

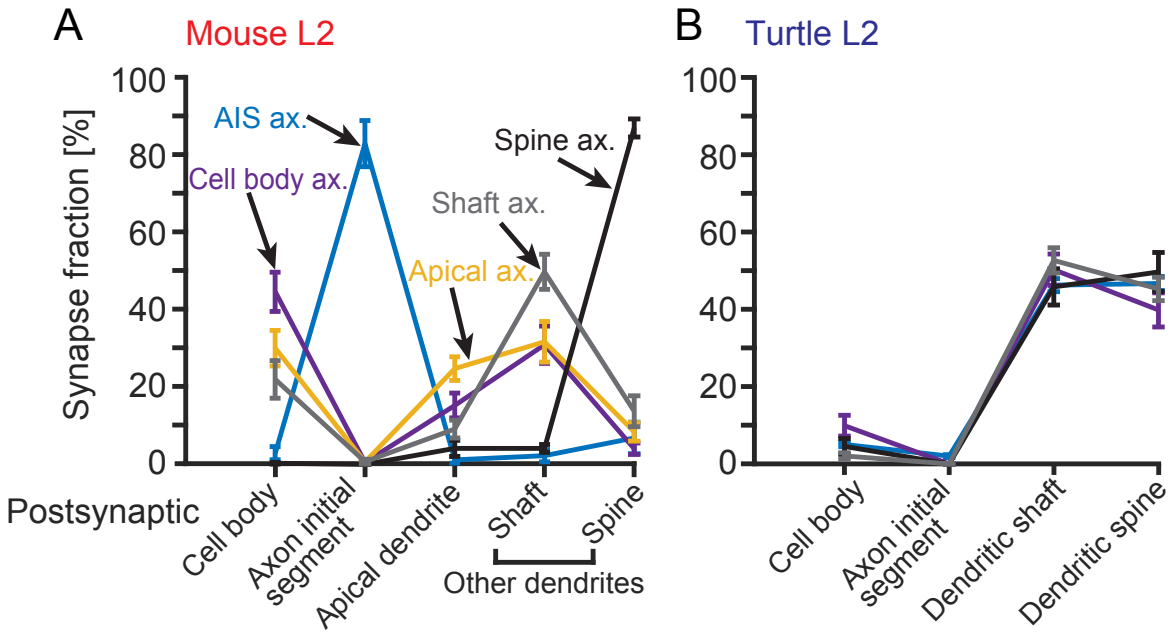

Fig. 4.14: **Axon subcellular innervation profiles in the mouse piriform and turtle dorsal cortex L2.**
For each axon population, the average synapse fraction found in each postsynaptic structure class was calculated after discarding the seeding synapse in each axon. **(A)** and **(B)** show the results for mouse piriform and the turtle dorsal cortex L2, respectively. The 5% significance level was corrected to $p<0.01$ and $p<0.0125$ for mouse and turtle, respectively (Bonferroni correction for multiple comparisons). For each axon population the fraction of synapses formed on each postsynaptic structure class was compared (ANOVA). In mouse, the postsynaptic structure class comparisons yielded significant probability values of at least $p<10^{-5}$. In turtle, the probability values for each comparison were not significant ($p>0.04$, $p>0.04$, $p>0.67$, and $p>0.62$ for the postsynaptic structure classes cell body, AIS, dendritic shaft, and spine head, respectively). The error bars represent SEM.

head synapses was 14.4 ± 17.9% (mean ± SD). The probability for finding again spine head synapses in dendritic spine head seeded axons was 91.0 ± 10.7% (mean ± SD) and the probability for finding dendritic shaft synapses was 4.3 ± 4.7% (mean ± SD). In turtle L2, the probabilities for both axon populations (dendritic spine head and shaft seeded axons, black and grey line in Figure 4.14B) were all close to 50%. The dendritic shaft seeded axons targeted again dendritic shaft locations with a probability of 52.7 ± 15.7% (mean ± SD) and dendritic spine heads with a probability of 45.3 ± 14.5% (mean ± SD). The dendritic spine head seeded axons targeted again dendritic spine heads with a probability of 49.7 ± 28.1% (mean ± SD) and dendritic shafts with a probability of 45.8 ± 26.1% (mean ± SD).

Again, these observations indicate the missing dendritic spine head and shaft innervation specificity of turtle dorsal cortex axons and synapse volume density measurements (see Figure 4.12) confirmed that both target classes are as available as in the mouse piriform cortex. However, the occurrence of postsynaptic structure classes, e.g. cell bodies, AISs and apical dendrites was not reflected by that measurement.

4.6 Axonal availability of postsynaptic targets

Subsequently, it was investigated whether the absence of target specificity was caused by a different availability of postsynaptic targets in the turtle dorsal cortex. The axonal availability was defined as the proximity of an axon to a given subcellular structure. It was hypothesized that the frequency of innervation of a subcellular structure positively correlates with the availability of a given axon. This availability assumption was quantitatively analyzed by defining a cylindrical surround of radius r_{surr} around a given axon. Subsequently, segments of the axon intersected by a cell body were labelled (see Figure 4.15). The path length of labelled segments were aggregated, providing the fractional axon path length being in proximity to cell bodies. The proximity was set to

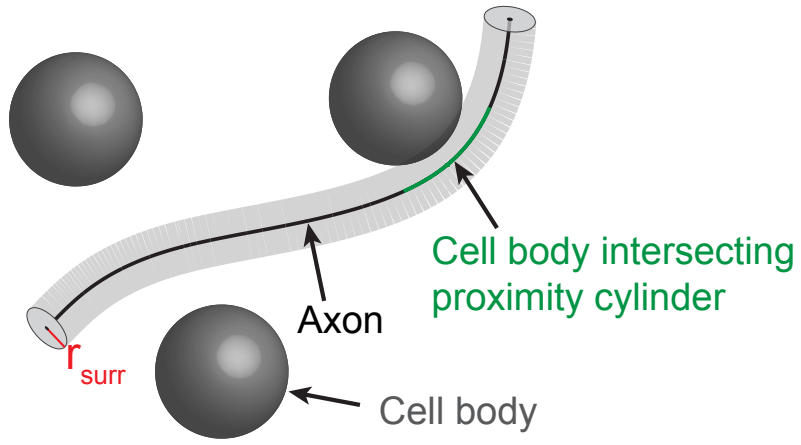

Fig. 4.15: **Geometric availability scheme.**
The sketch indicates the measurement method that was used to determine the availability of cell bodies (grey spheres) for a single axon (black line). Every time the axonal proximity (grey transparent tube, defined by the radius r_{surr}) is intersected by a cell body (green intersection segment), the segment path length was aggregated. The fractional path length of these segments was used as proxy for cell body availability for a given axon.

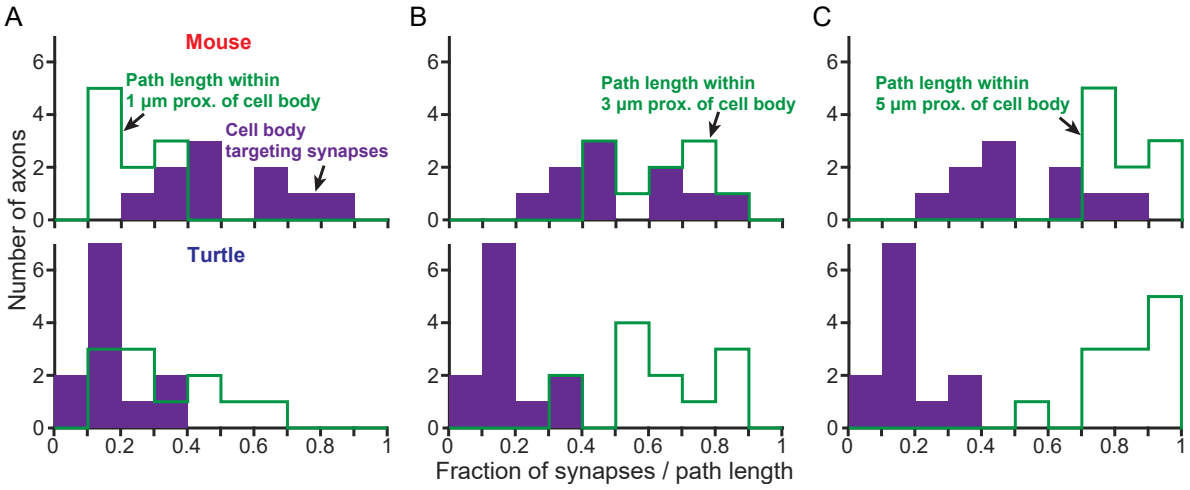

Fig. 4.16: **Geometric availability of cell bodies in the mouse piriform and turtle dorsal cortex L2.**
The histograms show the distribution of cell body synapse fractions (purple bars) and the path length fractions (green stairs) which were intersected by cell bodies. Axons with more than 10 synapses were selected in the turtle dorsal cortex L2 and a similarly sized subset of mouse L2 was randomly selected. The data is given for different proximity distances r_{surr} of 1 µm **(A)**, 3 µm **(B)** and 5 µm **(C)**.

several distances r_{surr} (1 µm, 3 µm and 5 µm).

This was done for a random subset of the population of axons seeded from synapses formed on cell bodies (see Figure 4.16). The data indicate that the geometric availability of cell bodies is indistinguishable for axon trajectories in turtle L2 and mouse L2 for the three chosen proximity distances (two sample t-test, $p_{1\mu m}>0.1$, $p_{3\mu m}>0.7$, $p_{5\mu m}>0.3$). For axons from the mouse piriform cortex L2 a probability of 50.6 ± 18.7% (mean ± SD) to again find an additional synapse on a cell body was measured, whereas in turtle the probability was 17.3 ± 9.3% (mean ± SD) which was significantly lower (two sample t-test, $p<10^{-3}$). This result indicates that both populations of axons in turtle L2 and mouse L2 are traversing the volume with a comparable trajectory with regard to proximity to cell bodies and only in mouse the axons tend to innervate cell bodies specifically.

Similarly to the mentioned two axons in turtle L3 avoiding dendritic spine heads (see Figure 4.8), two axons showed a substantial higher rate (>30%) of synapses formed on cell bodies in turtle L2 (see Figure 4.17 second from right). Although, the majority of turtle axons do not form synapses on any postsynaptic target class, there might be a small number of exceptions to that tendency.

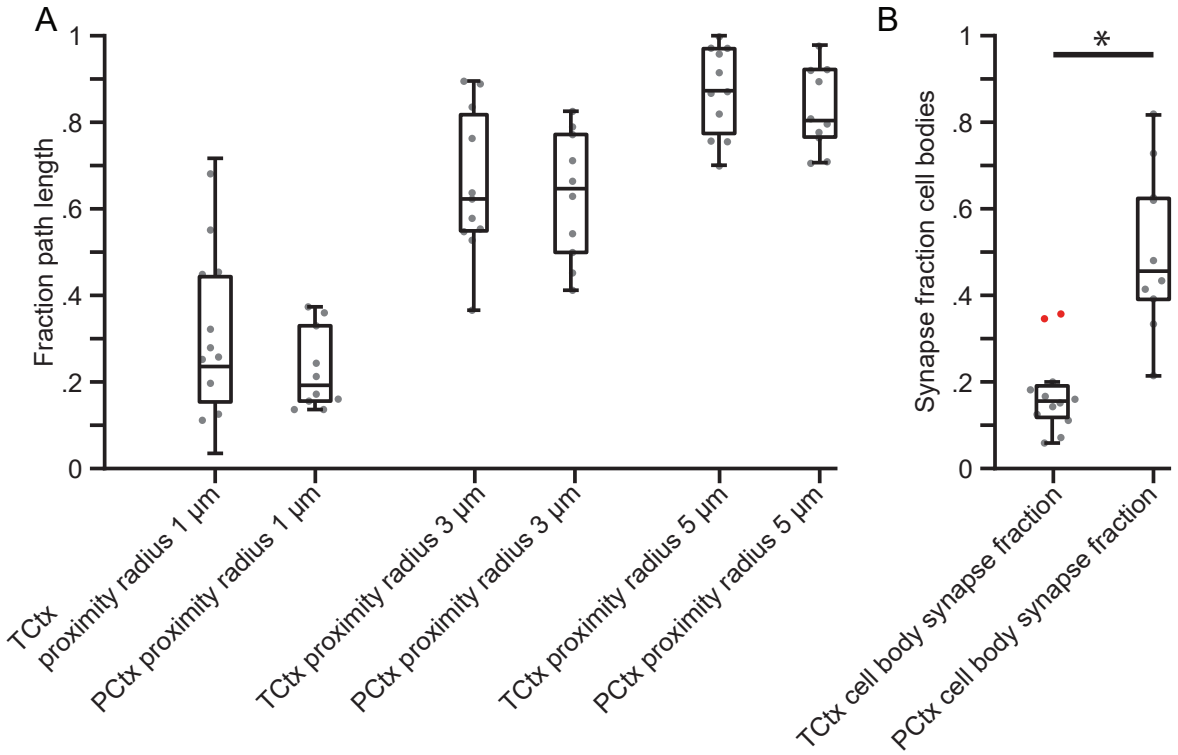

Fig. 4.17: **Geometric availability of cell bodies is different in the mouse piriform and turtle dorsal cortex L2.**
(A) Boxplot of the data used in Figure 4.16 show a comparable cell body availability for turtle and mouse axons (two sample t-test, $p_{1\mu m}>0.1$, $p_{3\mu m}>0.7$, $p_{5\mu m}>0.3$ for r_{surr} of 1 µm, 3 µm and 5 µm, respectively). **(B)** Innervation fraction of cell bodies differ significantly between turtle and mouse L2 axons seeded from cell body synapses (two sample t-test, $p<10^{-3}$). Each dot represents a single measurement and outliers are indicated by red dots. Note that there are two outlier turtle axons in **(B)** forming 10 out of 28 and 9 out of 26 synapses on cell bodies.

4.7 Mouse piriform cortex semilunar cells

Semilunar (SL) cells constitute one of the principal cell classes in the mouse piriform cortex and are located in the upper part of layer 2 [Haberly, 1983]. Their somato-dendritic shape (multiple apical dendrites) resembles partially the morphology of principle cells found in the turtle cortex (see Figure 2.4). Due to this morphological resemblance, these cells were further investigated.

The incoming subcellular innervation was measured and investigated whether it is as specific as for mouse pyramidal cells (see Figure 4.14A), or rather unspecific as in turtle principal neurons Figure 4.14B.

Two neurons in the mouse piriform cortex L2 dataset were identified having the morphological criteria of semilunar cells (lacking basal dendrite and cell body located superficially in layer 2, see Figure 4.18). A total of 28 axons were seeded from the

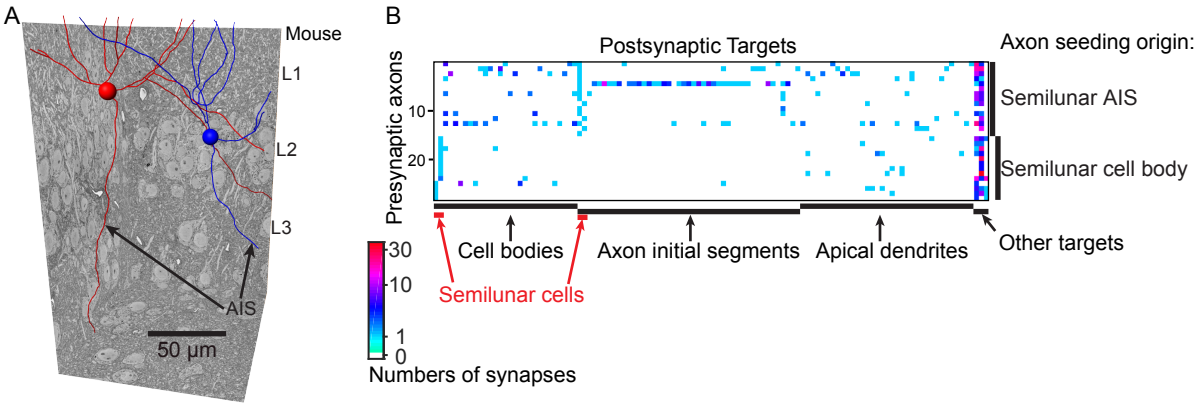

Fig. 4.18: **Semilunar cells in the mouse piriform cortex L2.**
(A) Low resolution mouse piriform cortex dataset boundaries and two skeleton representations of semilunar (SL) neurons. The blue and red spheres (diameter 10 µm) indicate the location of the cell bodies. The three layers are indicated on the right. **(B)** Connectivity matrix of the reconstruction results of single axons seeded from AISs and cell bodies of the SL neurons. Each row and each column represent a single axon and a postsynaptic process, respectively. In addition, each visualized postsynaptic process (column) was innervated at least once. The last three columns labelled as 'Other targets' represent the summed synapses formed on dendritic spine heads, shafts and axons, respectively.

two cell bodies (n = 13) and AISs (n = 15). The skeleton-reconstruction and synapse identification analysis was performed as described previously (see Figure 4.19). The specificity of axons innervating the axon initial segment of these neurons is substantially lower 17.0 ± 34.2% (mean ± SD) than for the pyramidal cells in the same dataset 86.3 ± 29.2% (mean ± SD) (compare Figure 4.14A and Figure 4.19A). In addition, the dendritic shaft and spine head distinction is less clear for the whole populations and seems more similar to the lack of innervation specificity phenomenon as found in turtle. However, when the previous criteria for the dendritic spine head and shaft specificity were applied (see Figure 4.11), a total of 19 (out of the 28) axons were identified forming >75% or <25% of their synapses on dendritic spine heads. Furthermore, the axons innervating the cell bodies of these identified semilunar cells showed no cell body specificity 7.3 ± 20.7% (mean ± SD). Next, the synapse input density onto AIS of SL and pyramidal cells in turtle L2 and mouse L2 was measured and the result is shown in Figure 4.19B. The input density onto mouse SL (0.15 ± 0.07 µm^{-1} (mean ± SD)) and turtle L2 PC AISs (0.18 ± 0.09 µm^{-1} (mean ± SD)) differ significantly compared to mouse L2 PC AISs which were innervated three times as often on average (0.52 ± 0.11 µm^{-1} (mean ± SD)). Although, the number of cells and axons in this analysis are very small, this data might be a first hint of a class of cells in the mouse piriform cortex sharing features of unspecific innervation. This observation might be viewed carefully as a remnant cell type of an older cortex type.

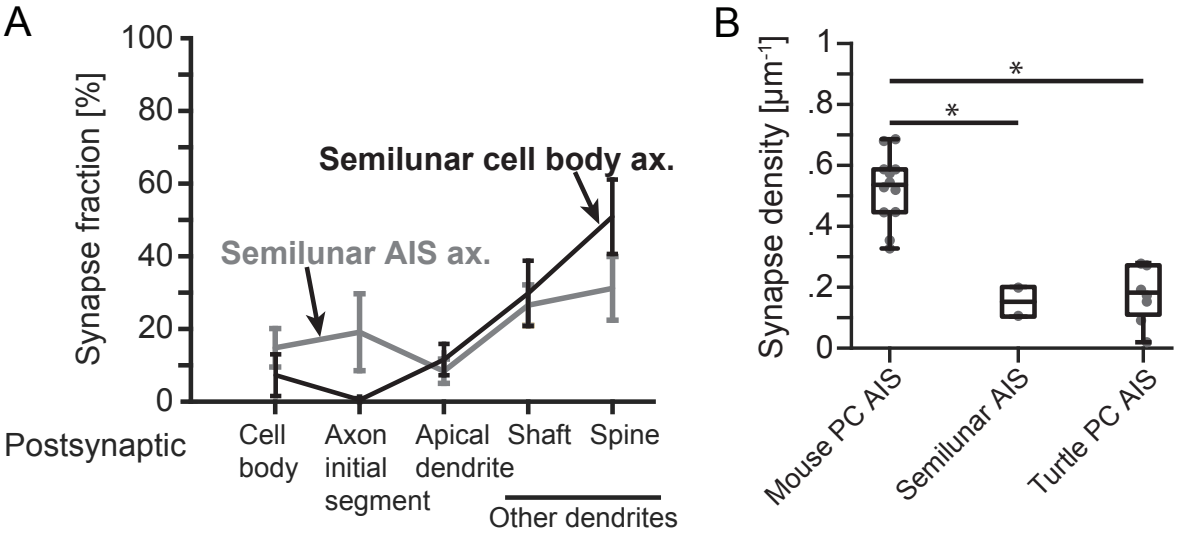

Fig. 4.19: **Axon subcellular innervation profiles of semilunar-seeded axons.** **(A)** For each axon population seeded from AISs and cell bodies of SL neurons, the average synapse fraction found in each postsynaptic structure class was calculated after discarding the seeding synapse in each axon. The error bars represent scanning electron microscope (SEM). **(B)** Synapse densities on AISs of mouse and turtle pyramidal and SL neurons were measured and show significant differences (ANOVA multiple comparison test, $p<10^{-3}$ for mouse pyramidal AIS and semilunar AIS, $p<10^{-5}$ for mouse pyramidal AIS and turtle pyramidal AIS, $p<10^{-3}$ for semilunar AIS and turtle pyramidal AIS). Grey dots represent single measurements.

4.8 Enwrapped dendritic spines in the turtle dorsal cortex

Besides the lack of axonal specificity, the turtle dorsal cortex shows structural differences compared to the mouse piriform cortex. In particular, boutons were frequently encountered enwrapping the post-synaptic spine completely (see Figure 4.20). This

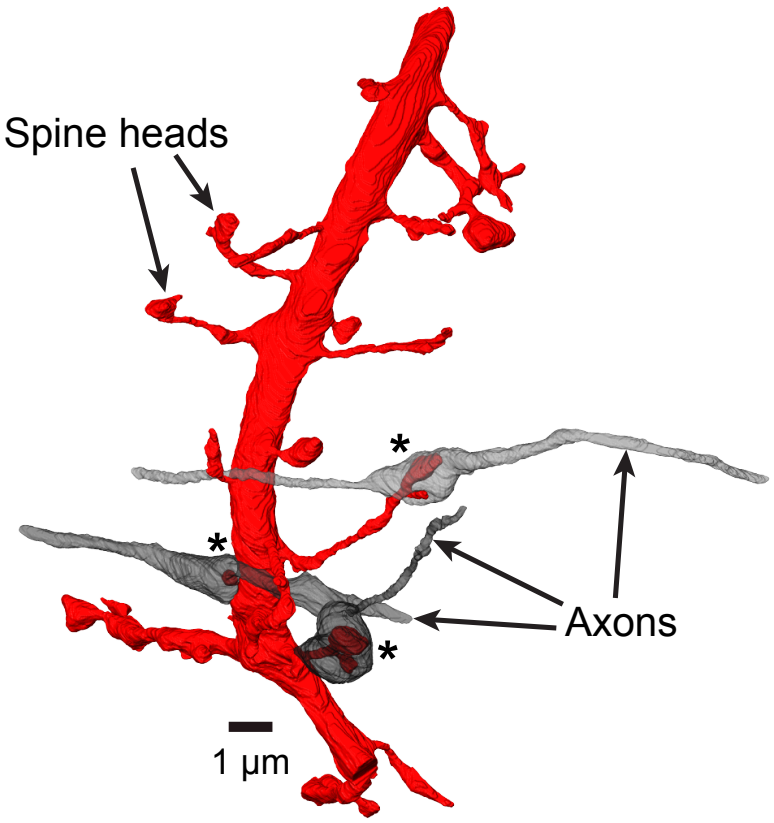

Fig. 4.20: **Enwrapped dendritic spines in the turtle dorsal cortex.**
Volume reconstruction (volume mode) of a spiny dendrite (red isosurface) and three axons (shades of grey) forming boutons which enwrap the dendritic spine head (top axon) or the dendritic spine completely (bottom axon).

structural phenomenon was confirmed in a total of four animals and in each layer of the turtle dorsal cortex. Serial section transmission electron microscope (ssTEM) data in Figure 4.21 shows one example. Volume reconstructions of SBEM data from L2 specimens obtained from two individual turtle dorsal cortices are shown in Figure 4.22

and Figure 4.23. The same phenomenon was also observed in the turtle dorsal cortex L3 dataset, which represents a fourth animal. Furthermore, they were observed in the turtle dorsal cortex L1 dataset confirming the occurrence in all three layers (data not shown).

Such a geometric configuration might constitute highly efficient and temporal

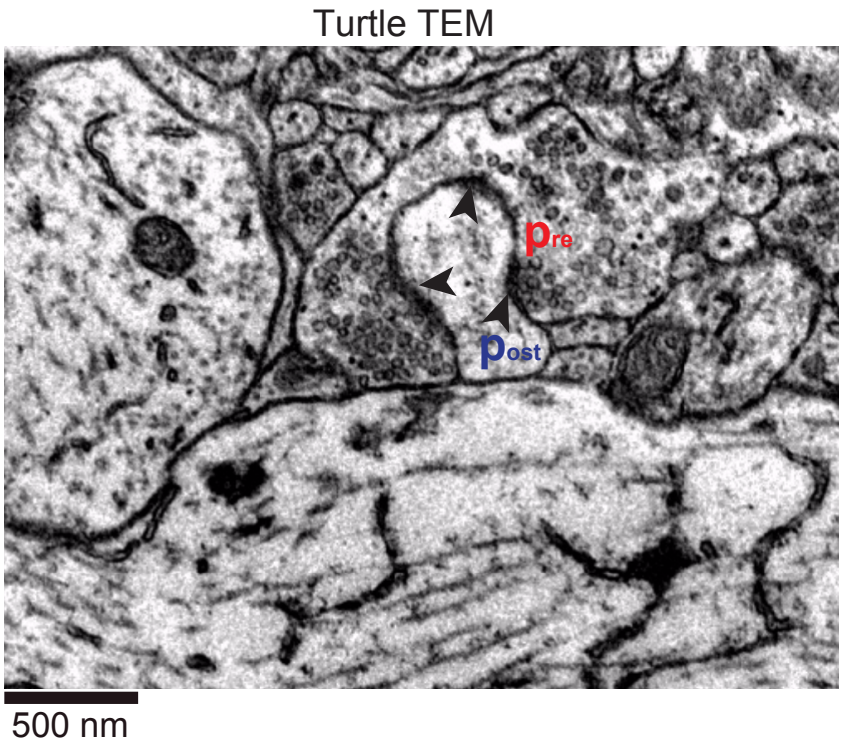

Fig. 4.21: **TEM cross section of a turtle enwrapped spine synapse.**
An image of an enwrapped dendritic spine acquired by TEM showing multiple active zone locations.
The data was kindly provided by Silke Haverkamp.

precise synaptic transmission (see review of large 'giant' mossy fiber boutons [Rollenhagen et al., 2007]). Therefore, the question was raised whether this is either a feature of certain axons, a feature of certain dendrites or an unspecific phenomenon. Here, the first approach of investigation was to determine whether the axon boutons enwrapping spines are in fact establishing synapses. Figure 4.21 shows structural features of synapses, e.g. active zone and vesicles being close to the presynaptic membrane. The

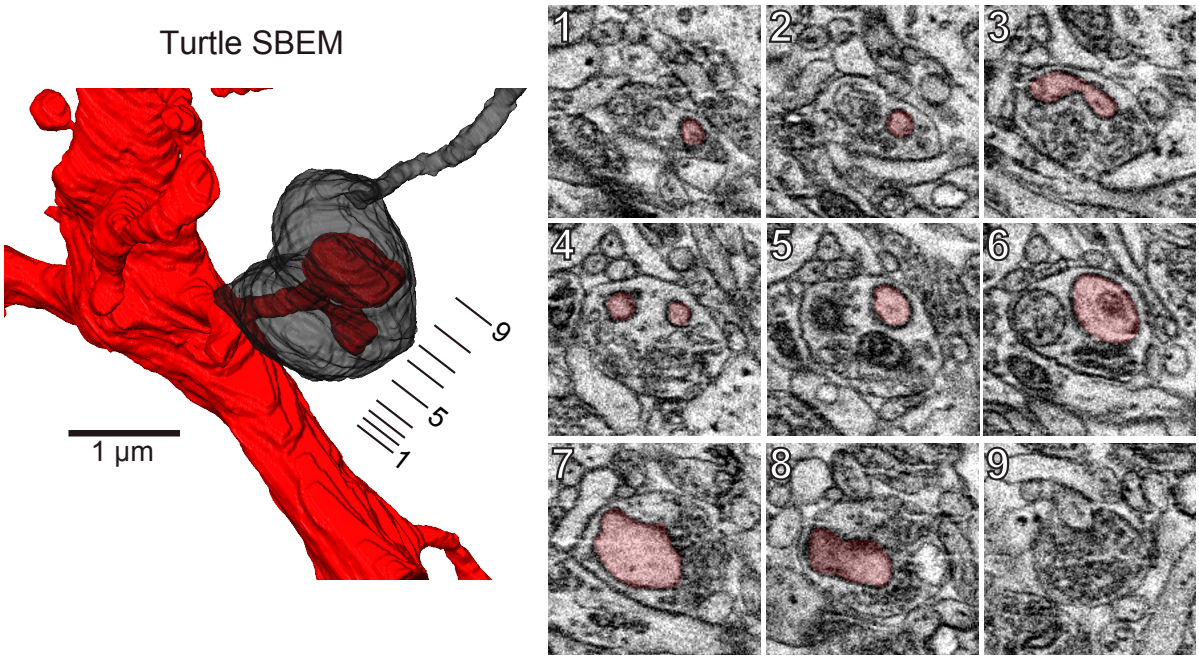

Fig. 4.22: **Reconstruction of an enwrapped spine synapse from 3D SBEM data.**
The inset of the enwrapped spine synapse (bottom axon) shown in Figure 4.20 was volume reconstructed by drawing the circumference of the axon and dendrite cross section in each plane. A subset of planes (plane locations indicated by the lines next to the isosurfaces) shows the cross section of the spine (red shading) and the enwrapping bouton.

TEM image in Figure 4.21 (kindly provided by Silke Haverkamp) shows multiple active zones. However, since single section TEM data does not reveal the three-dimensional structure, it was not clear if these multiple active zone sites were connected forming one large active zone. This data suggests that these spine enwrapping structures are indeed synapses.

Judging by the structure and location of the active zones, it might indicate a synaptic configuration with high efficiency and precise timing. Additional EM data using ssTEM was acquired using an in-plane resolution of 5 nm (TEM data was acquired by Gongsun Namand and kindly provided by Silke Haverkamp), and two examples of enwrapped spine heads were volume reconstructed (see Figure 4.23). Next, it was investigated whether the occurrence of enwrapped synaptic configurations are specific for pre- and/or postsynaptic processes. Therefore, the rate of enwrapped spine synapses was measured from a presynaptic and postsynaptic viewpoint and the result is shown in Figure 4.24. A total of 53 axons, 7 PCs and 5 spiny dendrites were investigated for the synapses formed by (presynaptic viewpoint) and onto (postsynaptic viewpoint) these processes. A spine synapse was classified as an enwrapped spine synapse when >50% of the spine head surface was covered by the presynaptic bouton and a clear invagination of the dendritic spine head was visible. On average, 29.0 ± 17.9% (mean ± SD) of all synapses formed by axons and 37.7 ± 7.2% (mean ± SD) of all synapses formed onto the postsynaptic processes were classified as enwrapped spine synapses.

Next, the volume density of enwrapped spine synapses was measured using the same subvolumes as in Figure 4.12 and the result is shown in Figure 4.25A. The volume density of enwrapped and 'classical' synapses on dendritic spine heads was similar (0.23 ± 0.08 μm^{-3} for enwrapped spine synapses and 0.24 ± 0.10 μm^{-3} for 'classical' synapses on dendritic spine heads, two sample t-test, p>0.91). Furthermore, the volume fraction of enwrapped spine synapses was compared with the fraction of enwrapped

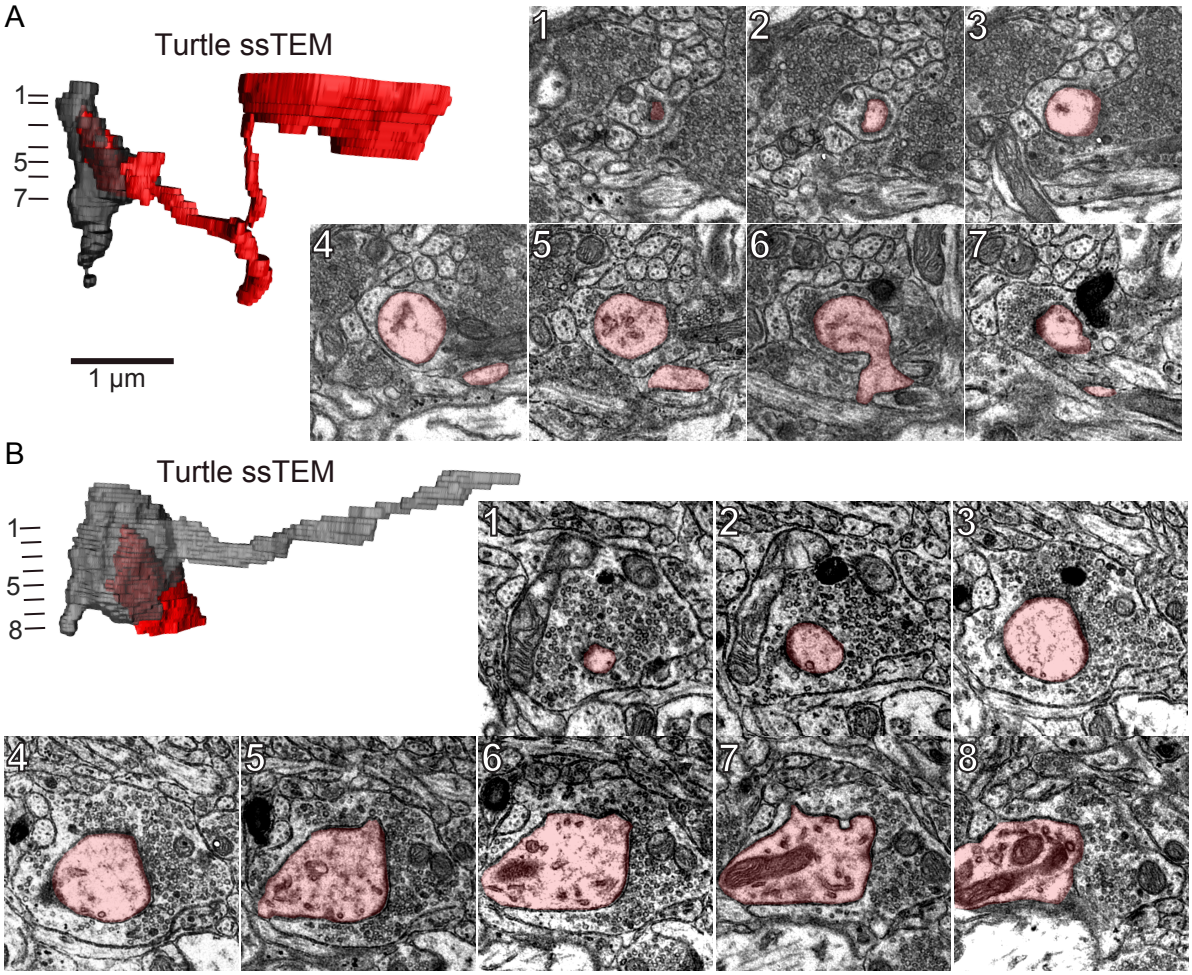

Fig. 4.23: **3D ssTEM reconstruction of enwrapped spine synapses.**
Volumes of two enwrapped spine heads (red isosurface) and the two presynaptic axons (grey isosurface) were volume reconstructed (volume mode). For both examples, a subset of planes (indicated by the lines next to the isosurfaces) are shown and the spine cross sections are shaded red.
The data was kindly provided by Silke Haverkamp.

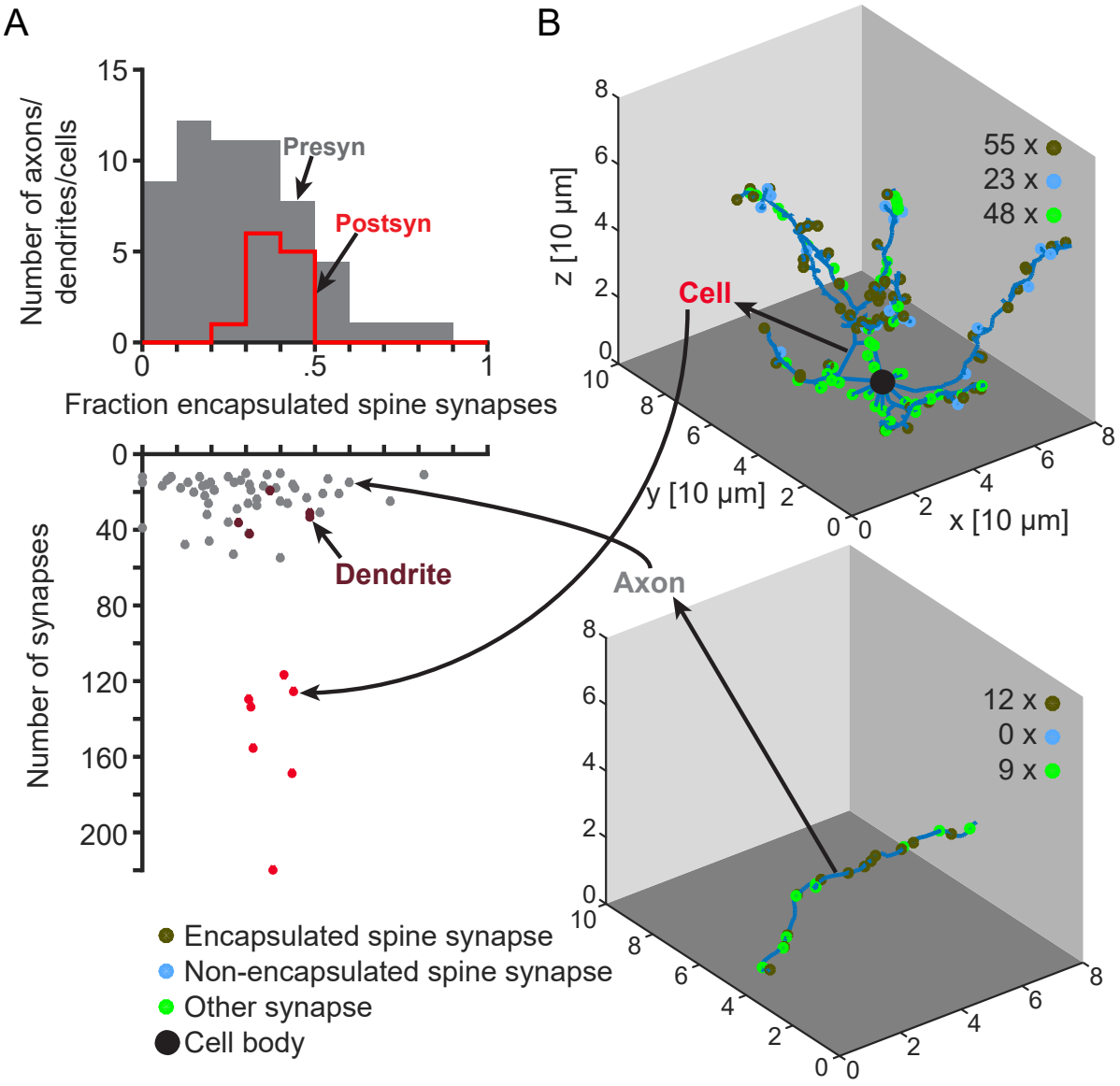

Fig. 4.24: **Occurrence of enwrapped spine synapses in presynaptic and postsynaptic processes.**
(A) Histogram of fractions of enwrapped spine synapses formed by axons (Presyn., grey) and onto dendrites or cells (Postsyn., red). The scatter plot below shows the absolute number of synapses for each investigated process. **(B)** Skeleton reconstructions of a pyramidal cell (top) and an axon (bottom) show all identified synapses in each process indicated by brown, blue and green circles.)

spine synapses of presynaptic and postsynaptic processes (see Figure 4.25B) However, no significant difference was found (ANOVA, p>0.34).

This result indicated that the overall occurrence of enwrapped spine synapses was at chance level along dendrites and axons. Next, it was investigated whether single axons form enwrapped spine synapses and 'classical' dendritic spine head synapses in a similar frequency to the volume density fractions (50.0 ± 18.9% (mean ± SD), see Figure 4.27A). The same pre- and postsynaptic processes were used, the synapses not formed on

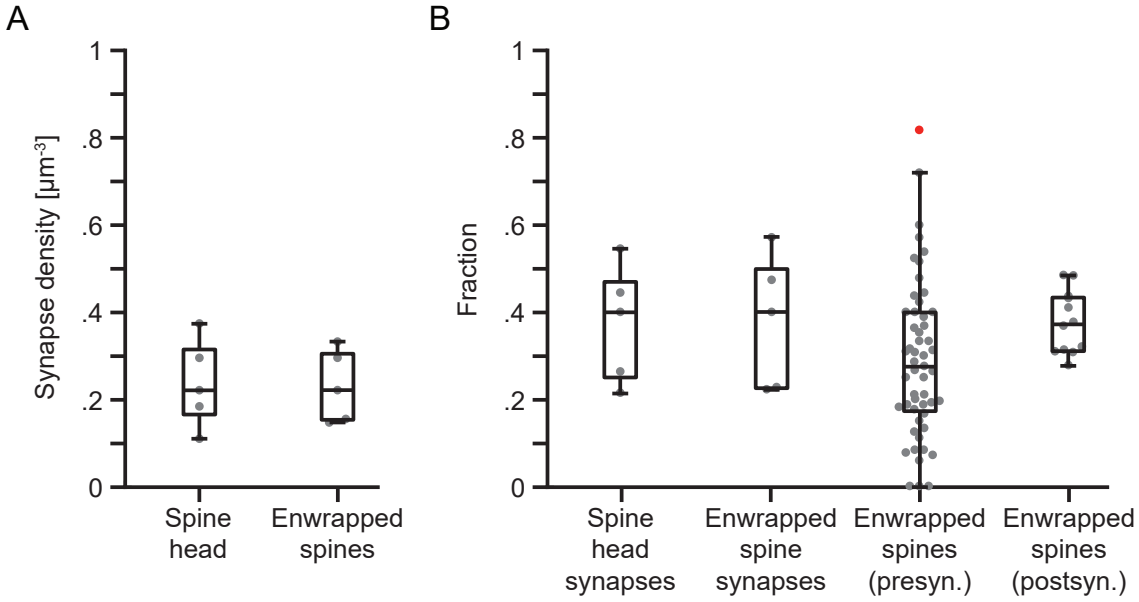

Fig. 4.25: **Volume density of enwrapped spine synapses.**
The volumes shown in Figure 4.12 were further investigated for enwrapped spine synapses. **(A)** Synapse volume densities of 'classical' dendritic spine head and enwrapped spine synapses are comparable (two sample t-test, p>0.91). **(B)** Fractional occurrence of presynaptic and postsynaptic enwrapped spine synapses are matching the fractional volume occurrence of enwrapped spine synapses (ANOVA multiple comparison test, p>0.34 for each pairwise comparison).
Each dot represents a single measurement and outliers are indicated by red dots.

dendritic spines were neglected and the results is shown in Figure 4.26 and Figure 4.27. As expected, an upshift of the distribution was observed (50.0 ± 18.9% (mean ± SD) for presynaptic and 66.6 ± 28.6% (mean ± SD) for postsynaptic processes).

Interestingly, the rate of established enwrapped spine synapses was particularly

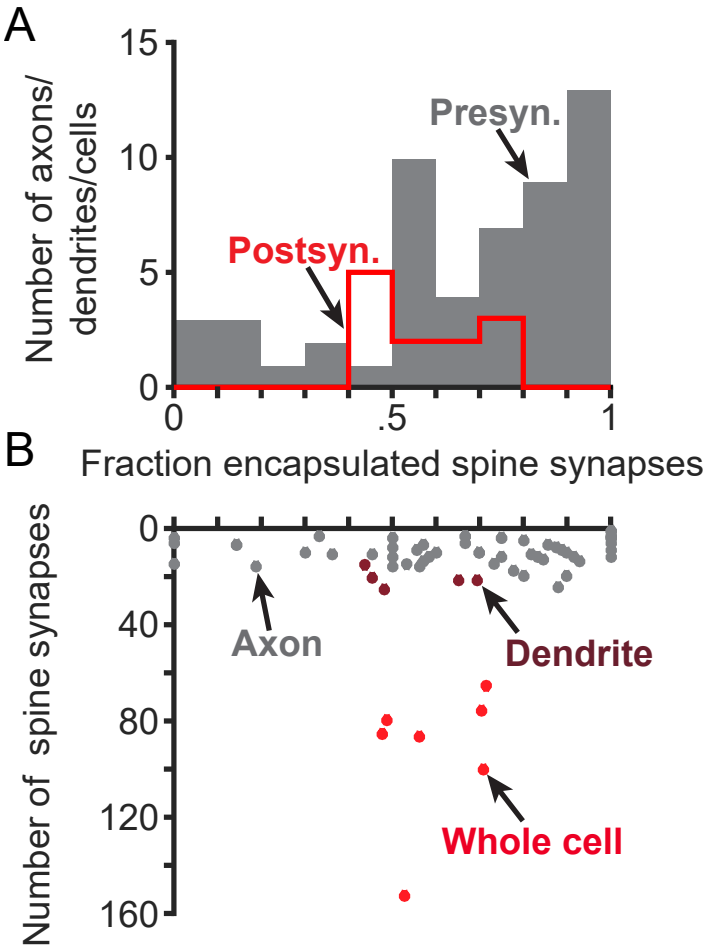

Fig. 4.26: **Occurrence of enwrapped spine synapses in the turtle dorsal cortex.**
(A) Histogram of fractions of enwrapped spine synapses (only including spine synapses) formed by axons (Presyn., grey) and onto dendrites or cells (Postsyn., red). **(B)** Scatter plot shows the absolute number of spine synapses for each investigated process.

frequent for a subset of axons (37.7% of axons established more than 80% of enwrapped spine synapses). This result indicates that at the level of presumably efficient synapses, a subset of axons exist showing a certain specificity for the described form of enwrapped synapses in turtle. Notably, none of these synaptic structural features were found in the mouse piriform cortex besides thorny structures of spines being enwrapped by presynaptic boutons, so called spinules (documented in mouse hippocampus, see [Spacek and Harris, 2004, Westrum and Blackstad, 1962]). However, the complete enwrapping of spines is also seen in mammalian hippocampal mossy fibers (described in [Hamlyn, 1961, Chicurel and Harris, 1992]) and retinal ganglion axons in thalamus lateral geniculate nucleus (LGN) (described in [Morgan et al., 2016, Spacek and Lieberman, 1974]).

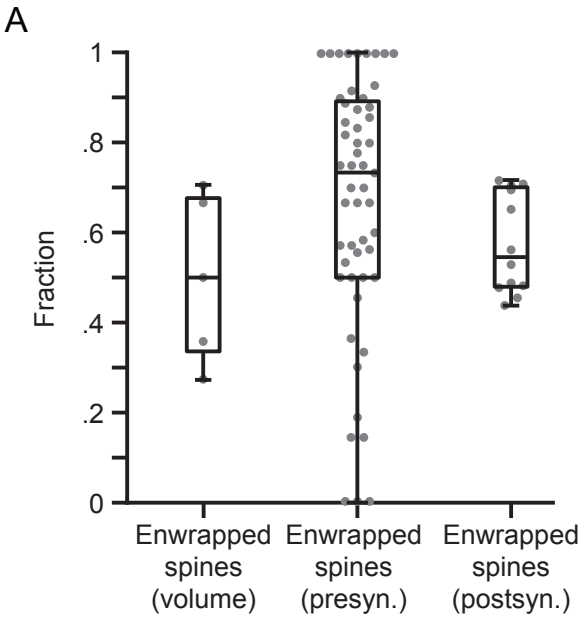

Fig. 4.27: **Enwrapped spine synapses in comparison with 'classical' dendritic spine head synapses.**
Boxplot of the fraction of enwrapped spine synapses with regard to spine synapses exclusively (first column). Fractions of the investigated presynaptic (second column) and postsynaptic (third column) processes which were comparable on average (ANOVA multiple comparison test, $p>0.36$ for each pairwise comparison).
Grey dots represent single measurements.

5 Discussion

A layered organization of the cerebral cortex is exclusively found in reptiles and mammals [Fournier et al., 2015]. In the mammalian cerebral cortex, the majority of axons are selective with regard to their postsynaptic target structure [Colonnier, 1968]. In particular, excitatory pyramidal cells form most of their synapses onto dendritic spine heads. The axonal specificity most likely affects the underlying mechanism of cortical signal computation and revealing its connectivity rules might be crucial to understand general cortical operating principles.

One of the questions addressed in this work was whether this axonal specificity is a phenomenon found in the mouse piriform and turtle dorsal cortex.

Therefore, serial block-face scanning electron microscopy was used to acquire four nanoliter-scale datasets from the turtle dorsal and mouse piriform cortex. The results indicate that the majority of axons in turtle dorsal cortex do not select their synaptic targets specifically, e.g. dendritic spine heads, shafts, cell bodies, etc. Furthermore, the results revealed that, globally, cortical axons in both species encounter the postsynaptic structure classes at similar frequencies which was measured by geometric proximity. Locally, however, mouse piriform cortex axons show specificities for subcellular targets while turtle dorsal cortex axons showed none of these highly specific innervations. Besides the lack of axonal specificity, axons forming synaptic boutons which enwrap dendritic spines were frequently observed in the turtle dorsal cortex and the investigation revealed a subset of axons forming such synapses preferentially.

Structurally similar synapses are also found in the mammalian hippocampus and studies showed that their synaptic signal transmission is highly efficienct and timed precisely [Maccaferri et al., 1998].

In summary, the work presented here provides new insights into the single synapse resolution connectivity of three-layered cortices in reptiles and mammals and revealed substantial differences in the circuit implementation.

5.1 Dendritic spine head and shaft innervation

The axons of mammalian excitatory pyramidal cells form the majority of their synapses onto dendritic spine heads, which is one of the most prominent features of the circuit pattern in the mammalian cerebral cortex [Colonnier, 1968, Megıas et al., 2001]. This dendritic spine head specificity in mammalian cortices was reproduced several times in the field of 3D EM neuroscience [Kasthuri et al., 2015, Landers et al., 2011] and was used in this work to classify excitatory MPCtx axons without having the location and morphology information of its neuron. Furthermore, this frequency of dendritic spine head synapses in the mouse piriform cortex was on average 91.0 ± 10.7% (mean ± SD). In comparison, inhibitory neurons (INs), e.g. Martinotti cells, are reported to form only 70% of their synapses on dendritic shaft locations [Wang et al., 2004]. Therefore, it is more challenging to classify cortical inhibitory axons. One approach was to measure the synapses that are not formed onto dendritic spine heads for a given axon.

For the four presumably inhibitory axon populations in the mouse piriform cortex, less than 20% of the synapses were formed on dendritic spine heads (see Figure 4.14A).

The reconstructions in the first dataset of the turtle dorsal cortex (L3) revealed that the wiring principle of specific innervation as observed in the mammalian cortex is not obeyed by turtle cortical axons. The datasets from turtle dorsal cortex L2 and L1 confirmed this lack of axon preference for dendritic spine heads and shafts and

supported the assumption that cortical excitatory axons in turtle cannot be identified by their synaptic target distribution. Since the two datasets of turtle dorsal cortex L2 and L1 were acquired from different animals, it is unlikely that the the measured effect was an outlier result due to an individual animal.

Reptiles and mammals share a common ancestor which most likely already had a cerebral cortex [Naumann and Laurent, 2017]. Beyond the same three-layered cytoarchitecture, the turtle dorsal and mouse piriform cortex share several macroscopic characteristics. First, ascending fibers in both cortices innervate the superficial portion of layer 1. Second, the cortical inhibitory neurons (INs) receive higher synapse densitied by these fibers than the principal cells. Third, functional recordings in both cortices demonstrated feedforward and feedback inhibition [Suzuki and Bekkers, 2012]. This work gives first insights into the cellular connectivity and suggests that several aspects of the underlying wiring are different despite the mentioned similarities. One might speculate that turtles could have lost this axonal specificity since it is present in birds which are direct descendants of dinosaurs (feature of dendritic spine head and shaft specificity is observed in [Kornfeld et al., 2017]). Alternatively, this feature of axonal specificity may have evolved independently in mammals and birds.

The 3D SBEM technique used in this study is limited with regard to the volume that can be obtained in reasonable time scales. A key step was to detect and establish ultrastructural or locally confined features. These features might be able to identify the origin of axons (e.g. thalamic innervation by multiple spine head innervation by single boutons) and dendrites (spine density) without the need of confirming the origin by whole cell reconstructions. The measurement of the local synapse distribution pattern of axons (ratio of dendritic spine head and shaft synapses) might be used as such a feature. This patter might classify the putative type (being excitatory or inhibitory) of

axons. Since an axon does not change its excitatory or inhibitory modality it should be valid beyond the volume boundaries.

5.1.1 Effect of PLASS on excitatory axon synapse distributions

A recent study in medial entorhinal cortex (MEC) of rats [Schmidt et al., 2017] found a PLASS of pyramidal cell (PC) axons which show a high frequency of dendritic shaft synapses proximal to the cell body followed by excitatory synapses formed on dendritic spine heads. This finding might be interfering with the method of classification (25th - 75th percentile) if PLASS is a wiring mechanism also found in the piriform cortex (PCtx). The results in this work are demonstrating this dichotomy of dendritic spine head and shaft synapses (in mouse piriform cortex >85% of all axons formed >75% or <25% of their synapses on dendritic spine heads, see Figure 4.11) and if PCs in the PCtx sort their synapses according to the proposed PLASS, the measurement results in this work would be a conservative demonstration of the axonal specificity. In addition, PLASS was measured at a distance of >120 µm from its originating cell body in the rat medial entorhinal cortex. Therefore, the probability is further reduced that the synapse sorting was measured in the turtle and mouse L2 datasets as observed in this work.

5.2 Innervation specificity of subcellular structures - phenotype of inhibitory neurons

Peters' rule of wiring postulates that synapses are formed in correlation with the spatial proximity of a given pre- and postsynaptic process [Peters and Feldman, 1976]. A random wiring solely based on geometric proximity might constitute a random wiring

principle which was tested in cortices of both species. In this work, we hypothesize that specific innervations are driven by other mechanisms than proximity or apposition of two neuronal processes. The novel approach of single synapse resolution electron microscopy based Connectomics finally allows to address this question.

In the mammalian cortex, it is established that classes of interneurons exhibit specific innervation of subcellular structures, e.g. Basket cells specifically innervate the perisomatic region of PCs (described by [Szentágothai, 1973]) and Chandelier cells specifically innervate PC axon initial segments (described by [Somogyi, 1977]). Axon innervation profiles might represent the innervation phenotype of interneurons and might be used to identify axons of a certain neuron type. The confirmation of this hypothesis might be interpreted as a direct contradiction to Peters' rule at least for these types of inhibitory neurons. Exceptions like the double bouquet cell innervating the cell bodies of PCs and INs, dendritic spine heads and shafts [Somogyi et al., 1983] would represent a class of INs which follows a random wiring rule and innervates structures according to its geometric availability. One has to point out that the selection approach used here introduces a bias which was partially corrected for by discarding the seeding synapse (see Figure 4.14). In addition, the measured specificities of axon populations tend to include all kinds of axons, e.g. cell body preferring axons contained in the population of apical dendrite seeded axons and vice versa, further diluting the measured axon subcellular innervation profiles. These measured specificities of mouse piriform cortex L2 axons were demonstrated in this work despite the described dilution of axon populations. This dilution of axon populations emphasises the need to further investigate subpopulations of axons exhibiting specific innervation. This work demonstrated that populations of axons in the turtle dorsal cortex specifically innervate dendritic spines by enwrapping them (see Figure 4.27).

The functional similarity (feedforward and feedback inhibition) shown in both cortices is potentially implemented by specific inhibitory wiring in case of the mouse piriform cortex. A study performed in the Laurent laboratory using a gene expression atlas of two reptilian species (turtle and lizard), suggest that the transcriptomic signature of GABAergic neurons already existed in the common ancestors of reptiles and mammals [Tosches et al., in revision]. Considering the phenotype of specific innervation to be a characteristic of INs in combination with the finding of the conserved GABAergic neurons in amniotes led to the naive expectation that the turtle cortex exhibits an inhibitory wiring phenotype that might be similarly specific as demonstrated in mammalian cortices. However, the results in this work indicate that turtle cortical INs have lost that feature of specific wiring or it was derived evolutionary *de novo* in mammals. In addition, this finding raises the question how the turtle cortex implements the functional feedforward and feedback inhibition.

The demonstrated specificity of mouse piriform cortex axons are contradictive to random wiring principles solely based on geometric proximity. However, the innervation pattern suggest specific synapse formation that overcomes geometric apposition. In contrast, the majority of turtle cortical axons seem to randomly innervate their proximal surrounding and are therefore obeying the postulated wiring rule based on geometric proximity.

5.3 Mouse piriform cortex semilunar neurons

The excitatory semilunar (SL) cells in the PCtx show differences in morphology and electrophysiological properties. Studies suggest that they are involved in a separate neuronal circuit when compared to PCs (SL cells receiving stronger afferent input [Suzuki and Bekkers, 2012]). SL cells were further investigated in this work. First, morphological criteria [Haberly, 1983] were used and a total of three cells were identified

in the low resolution mouse piriform cortex dataset (out of 500 investigated neurons) and two were further investigated having their AISs contained in the high resolution dataset. The results demonstrate that the two SL cells are not the target of specific innervation. Out of 15 AIS-seeded axons (identified by synapses formed on SL AISs), a single axon alone exhibited a strong specificity for AISs (84 out of 89 synapses formed on AISs see Figure 4.18B) and this axon originated most likely from a Chandelier cell that are known to innervate AISs in a neuron type specific pattern (see review [Bekkers and Suzuki, 2013]). Furthermore, the 13 axons seeded from the two SL cell bodies did not show any cell body innervation specificity, having on average 7.3 ± 0.7% (mean ± SD) of their synapses formed on cell bodies. Again a single axon showed a preference for cell bodies (12 out of 16 synapses formed on cell bodies). This result was surprising since both the SL cells and PCs are described as being the target of cell body innervating INs (see review [Suzuki and Bekkers, 2012]). Obviously, this finding has to be considered carefully since the number of cells and axons measured here was critically small.

Interestingly, the dendritic spine head and shaft specificity was present in 19 out of the 28 axons (>75% or <25% of their synapses are formed on dendritic spine heads). A highly speculative interpretation might be that SL cells possess circuit pattern features of old cortices by not being innervated specifically at the various subcellular structures which assumes that old cortices did not possess subcellular-specific axon innervation features. Despite this missing specific innervation, the majority of axons seeded from SL cells maintained their specificity for dendritic spine heads and shafts.

5.4 Large boutons in both turtle dorsal cortex and mammalian hippocampus

This work focused not solely on skeleton reconstruction and synapse identification, but also on ultrastructural differences between the mouse piriform and turtle dorsal cortex were examined. Such structural features can be used as labels which might specifically identify classes of processes as already mentioned. One structural difference was the investigated enwrapped spine synapse sharing a close structural resemblance to mossy fibers which emerge from the granule cells of the dentate gyrus. The 'giant' boutons formed by mossy fibers are described in their function as being able to generate large currents and potentials postsynaptically [Maccaferri et al., 1998]. Furthermore, the boutons formed by retinal ganglion axons in mammalian thalamus [Morgan et al., 2016] are structurally similar and enwrap multiple dendritic spines of thalamocortical neurons. However, the afore mentioned study did not reach a conclusion about whether those 'giant' boutons were preferentially formed by axons or rather received by dendrites. Also, corticothalamic axons from the somatosensory 'barrel' cortex form 'giant' boutons in the rodent thalamus [Hoogland et al., 1991]. Clear reports about similar enwrapped dendritic spine structures in the mammalian six-layered neocortex or the forebrain of birds were not found. In addition, no study was found reporting a similar synapse structure in the mammalian piriform cortex. There are several morphological distinct differences to the synapse Calyx of Held which most prominently forms a giant synapse on a single cell body [Held, 2011] and is substantially larger in diameter compared to the observed enwrapped spines (10 - 30 µm, see [Ryugo et al., 2006]).

The results presented in this work (see Figure 4.27) demonstrate an equal rate of occurrence of enwrapped spine synapses compared to 'classic' dendritic spine head synapses. In addition, there are indications that a subpopulation of axons preferentially

forms the enwrapped type of spine synapse rather than the 'classical' dendritic spine head synapse. These structurally peculiar synapses are reported multiple times in subcortical structures like thalamus and hippocampus which are considered to be an ancient type of cortex. A highly speculative hypothesis would be that old cortices might have a necessity for such synapses performing signal transmission in a highly reliable and precisely timed manner. If this kind of synapse transmission was lost during evolutionary development of isocortex in mammals, one might speculate that the specific wiring in the six-layered cortex is a mechanism which replaced this necessity.

5.5 Olfactory cortex in turtles

Reviews about the mammalian piriform and reptilian dorsal cortex [Fournier et al., 2015] presented various similarities which were a driving incentive for this work. The sensory modalities which are mainly processed in the two cortices are different. In the piriform cortex, olfactory sensory information is processed and in the turtle dorsal cortex, visual sensory information is processed. Studies in the 1980s injected tracers into the olfactory bulb (OB) of turtles which labelled the superficial third of the molecular layers in the lateral cortex of both hemispheres. These regions are considered to be the analogs to the mammalian primary olfactory cortex [Desan, 1988, Skeen et al., 1984] (see also introduction Figure 2.4). The lateral cortex in turtles also consists of three layers and since the cortical architecture is more similar across regions in reptiles, there is a notion that the turtle brain might perform a similar or even a general computation on different sensory inputs [Naumann et al., 2015].

Determining the wiring phenotype in this part of the turtle brain might clarify how the wiring for different sensory modality processing is implemented. Therefore, the turtle lateral cortex might be the region of interest for a prospective research project. In addition, such an experiment would clarify whether the turtle brain obeys cortex wide

wiring rules.

5.6 3D EM-based Connectomics

With larger 3D EM volumes, the tasks of manual skeleton reconstruction and especially volume contouring are prohibitively time consuming [Helmstaedter, 2013] and similar analysis will only be possible with semi- and/or ideally fully automated volume reconstructions at feasible time scales. Attempts of semi-automated reconstruction are currently performed in the Helmstaedter laboratory [Berning et al., 2015, Staffler et al., 2017] and dense reconstruction might potentially give precise insights with regard to the composition of postsynaptic targets in the proximity of a given axon. In addition, densely reconstructed neuropil might also predict synaptic strength of connected pairs of neurons in terms of number of synapses and the total synaptic contact area.

One also has to point out that spine density measurement is simple and time-efficient in labeled light microcopy data, but it gets very time consuming and therefore costly in larger volumes of 3D high resolution EM data using manual annotation. Furthermore, light microscopy data only allows for the investigation of labeled boutons which are opposed to neuronal processes. This measurement requires sparse labeling due to the limited spatial resolution. In contrast, the acquired EM data allows to precisely resolve chemical synapses and identify the postsynaptic target class, e.g. cell body, dendritic spine head and shaft, etc.

5.7 Conclusion and outlook

A century ago, researcher often assumed that complex structures evolved by addition of new and/or more sophisticated parts [Edinger and Rand, 1908, Kappers, 1908]. However, most modern studies favor an alternative theory which argues that brains evolved by altering parts which were already present in a common ancestor [Johnston, 1923]. In this context, three-layered cortices are often considered to be 'simpler' due to the smaller number of layers but also with respect to their computation when compared to six-layered cortices [Fournier et al., 2015, Shepherd, 2011]. The notion here is that understanding 'simpler' cortices generate basic processing unit templates which might eventually be used to describe processing units of six-layered cortex. These comparisons might eventually help to understand the processing in human cortex mechanistically.

For the first time, this work gave insights into the single synapse resolution connectivity of three-layered cortices in mammals and reptiles and indicated that the wiring mechanism might be fundamentally different despite the functional and cytoarchitectural similarities. In addition, the results underline the necessity of measuring connectomes using 3D electron-microscopy which is currently the only tool providing sufficient spatial resolution over a sufficiently large scale to gather information about neuronal circuits information of neuronal circuits.
The findings reported in this work need to be verified in control experiments accounting for inter-individual variation. The wiring specificity comparison across mammalian and reptilian species are required to calibrate the inter-species variation within these classes. As mentioned, the wiring specificity comparison to other three-layered cortices, like the mammalian hippocampus and the reptilian lateral cortex, might be prospective studies to determine the inter-cortical variance within a species.

High resolution volume EM remains a fast developing field and mapping larger neuronal volumes within reduced time scales will become more feasible. With the development of fully automated reconstructions, it will become possible for projects to acquire volumes containing the whole extent of cortices. Such experiments would be able to measure the entirety of synapses (synaptome [DeFelipe, 2010]) formed on and by neurons to describe neuronal circuit units more precisely. Overall, connectomics may play a vital role and its developments might eventually help to understand the human brain.

List of Figures

List of Tables

6 Bibliography

[Aboitiz and Montiel, 2015] Aboitiz, F. and Montiel, J. F. (2015). Olfaction, navigation, and the origin of isocortex. *Frontiers in neuroscience*, 9:402.

[Ashida and Carr, 2011] Ashida, G. and Carr, C. E. (2011). Sound localization: Jeffress and beyond. *Current opinion in neurobiology*, 21(5):745–751.

[Balaram and Kaas, 2014] Balaram, P. and Kaas, J. H. (2014). Towards a unified scheme of cortical lamination for primary visual cortex across primates: insights from neun and vglut2 immunoreactivity. *Frontiers in neuroanatomy*, 8:81.

[Bar et al., 2000] Bar, I., de Rouvroit, C. L., and Goffinet, A. M. (2000). The evolution of cortical development. an hypothesis based on the role of the reelin signaling pathway. *Trends in neurosciences*, 23(12):633–638.

[Bekkers and Suzuki, 2013] Bekkers, J. M. and Suzuki, N. (2013). Neurons and circuits for odor processing in the piriform cortex. *Trends in neurosciences*, 36(7):429–438.

[Benshalom and White, 1986] Benshalom, G. and White, E. L. (1986). Quantification of thalamocortical synapses with spiny stellate neurons in layer iv of mouse somatosensory cortex. *Journal of Comparative Neurology*, 253(3):303–314.

[Berning et al., 2015] Berning, M., Boergens, K. M., and Helmstaedter, M. (2015). SegEM: efficient image analysis for high-resolution connectomics. *Neuron*, 87(6):1193–1206.

[Betzig et al., 2006] Betzig, E., Patterson, G. H., Sougrat, R., Lindwasser, O. W., Olenych, S., Bonifacino, J. S., Davidson, M. W., Lippincott-Schwartz, J., and Hess, H. F. (2006). Imaging intracellular fluorescent proteins at nanometer resolution. *Science*, 313(5793):1642–1645.

[Binzegger et al., 2004] Binzegger, T., Douglas, R. J., and Martin, K. A. (2004). A quantitative map of the circuit of cat primary visual cortex. *Journal of Neuroscience*, 24(39):8441–8453.

[Blanton et al., 1987] Blanton, M. G., Shen, J. M., and Kriegstein, A. R. (1987). Evidence for the inhibitory neurotransmitter γ-aminobutyric acid in aspiny and sparsely spiny nonpyramidal neurons of the turtle dorsal cortex. *Journal of Comparative Neurology*, 259(2):277–297.

[Bloom and Aghajanian, 1968] Bloom, F. E. and Aghajanian, G. K. (1968). Fine structural and cytochemical analysis of the staining of synaptic junctions with phosphotungstic acid. *Journal of ultrastructure research*, 22(5-6):361–375.

[Bock et al., 2011] Bock, D. D., Lee, W.-C. A., Kerlin, A. M., Andermann, M. L., Hood, G., Wetzel, A. W., Yurgenson, S., Soucy, E. R., Kim, H. S., and Reid, R. C. (2011). Network anatomy and in vivo physiology of visual cortical neurons. *Nature*, 471:177–182.

[Boergens et al., 2017] Boergens, K. M., Berning, M., Bocklisch, T., Bräunlein, D., Drawitsch, F., Frohnhofen, J., Herold, T., Otto, P., Rzepka, N., Werkmeister, T., Werner, D., Wiese, G., Wissler, H., and Helmstaedter, M. (2017). webknossos: efficient online 3d data annotation for connectomics. *Nature Methods*, 14:691–694.

[Bohland et al., 2009] Bohland, J. W., Wu, C., Barbas, H., Bokil, H., Bota, M., Breiter, H. C., Cline, H. T., Doyle, J. C., Freed, P. J., Greenspan, R. J., et al. (2009). A

proposal for a coordinated effort for the determination of brainwide neuroanatomical connectivity in model organisms at a mesoscopic scale. *PLoS computational biology*, 5(3):e1000334.

[Borst and Helmstaedter, 2015] Borst, A. and Helmstaedter, M. (2015). Common circuit design in fly and mammalian motion vision. *Nature Neuroscience*, 18(8):1067.

[Braitenberg, 1978] Braitenberg, V. (1978). Cortical architectonics: general and areal. *Architectonics of the cerebral cortex*, pages 443–465.

[Braitenberg and Schüz, 1998] Braitenberg, V. and Schüz, A. (1998). Cortical architectonics. In *Cortex: Statistics and Geometry of Neuronal Connectivity*, pages 135–137. Springer.

[Brecht and Sakmann, 2002] Brecht, M. and Sakmann, B. (2002). -dynamic representation of whisker deflection by synaptic potentials in spiny stellate and pyramidal cells in the barrels and septa of layer 4 rat somatosensory cortex. *The Journal of physiology*, 543(1):49–70.

[Briggman and Bock, 2012] Briggman, K. L. and Bock, D. D. (2012). Volume electron microscopy for neuronal circuit reconstruction. *Current opinion in neurobiology*, 22:154–161.

[Briggman et al., 2011] Briggman, K. L., Helmstaedter, M., and Denk, W. (2011). Wiring specificity in the direction-selectivity circuit of the retina. *Nature*, 471(7337):183.

[Brodmann, 1909] Brodmann, K. (1909). *Vergleichende Lokalisationslehre der Grosshirnrinde in ihren Prinzipien dargestellt auf Grund des Zellenbaues*. Barth.

[Brox et al., 2004] Brox, A., Puelles, L., Ferreiro, B., and Medina, L. (2004). Expression of the genes emx1, tbr1, and eomes (tbr2) in the telencephalon of xenopus laevis

confirms the existence of a ventral pallial division in all tetrapods. *Journal of Comparative Neurology*, 474(4):562–577.

[Bullock, 1984] Bullock, T. H. (1984). Comparative neuroscience holds promise for quiet revolutions. *Science*, 225(4661):473–478.

[Butler, 1994] Butler, A. B. (1994). The evolution of the dorsal pallium in the telencephalon of amniotes: cladistic analysis and a new hypothesis. *Brain Research Reviews*, 19(1):66–101.

[Carrera et al., 2008] Carrera, I., Ferreiro-Galve, S., Sueiro, C., Anadón, R., and Rodríguez-Moldes, I. (2008). Tangentially migrating gabaergic cells of subpallial origin invade massively the pallium in developing sharks. *Brain research bulletin*, 75(2-4):405–409.

[Chang et al., 2017] Chang, J.-B., Chen, F., Yoon, Y.-G., Jung, E. E., Babcock, H., Kang, J. S., Asano, S., Suk, H.-J., Pak, N., Tillberg, P. W., et al. (2017). Iterative expansion microscopy. *Nature methods*, 14(6):593.

[Chen et al., 2015] Chen, F., Tillberg, P. W., and Boyden, E. S. (2015). Expansion microscopy. *Science*, page 1260088.

[Chicurel and Harris, 1992] Chicurel, M. E. and Harris, K. M. (1992). Three-dimensional analysis of the structure and composition of ca3 branched dendritic spines and their synaptic relationships with mossy fiber boutons in the rat hippocampus. *Journal of comparative neurology*, 325(2):169–182.

[Cobos et al., 2001] Cobos, I., Puelles, L., and Martínez, S. (2001). The avian telencephalic subpallium originates inhibitory neurons that invade tangentially the pallium (dorsal ventricular ridge and cortical areas). *Developmental biology*, 239(1):30–45.

[Colombe et al., 2004] Colombe, J. B., Sylvester, J., Block, J., and Ulinski, P. S. (2004). Subpial and stellate cells: two populations of interneurons in turtle visual cortex. *Journal of Comparative Neurology*, 471(3):333–351.

[Colombe and Ulinski, 1997] Colombe, J. B. and Ulinski, P. S. (1997). Anatomical organization of feedforward pathways in cortical microcircuits. In *Computational Neuroscience*, pages 605–608. Springer.

[Colonnier, 1968] Colonnier, M. (1968). Synaptic patterns on different cell types in the different laminae of the cat visual cortex. an electron microscope study. *Brain research*, 9(2):268–287.

[Connors and Kriegstein, 1986] Connors, B. W. and Kriegstein, A. (1986). Cellular physiology of the turtle visual cortex: distinctive properties of pyramidal and stellate neurons. *Journal of Neuroscience*, 6(1):164–177.

[Cosans and Ulinski, 1990] Cosans, C. E. and Ulinski, P. S. (1990). Spatial organization of axons in turtle visual cortex: Intralamellar and interlamellar projections. *Journal of Comparative Neurology*, 296(4):548–558.

[Davila et al., 1999] Davila, J. C., Padial, J., Andreu, M. J., and Guirado, S. (1999). Calbindin-d28k in cortical regions of the lizard psammodromus algirus. *The Journal of comparative neurology*, 405(1):61–74.

[De Vivo et al., 2017] De Vivo, L., Bellesi, M., Marshall, W., Bushong, E. A., Ellisman, M. H., Tononi, G., and Cirelli, C. (2017). Ultrastructural evidence for synaptic scaling across the wake/sleep cycle. *Science*, 355(6324):507–510.

[DeFelipe, 2010] DeFelipe, J. (2010). From the connectome to the synaptome: an epic love story. *Science*, 330(6008):1198–1201.

[Denk and Horstmann, 2004] Denk, W. and Horstmann, H. (2004). Serial block-face scanning electron microscopy to reconstruct three-dimensional tissue nanostructure. *PLoS biology*, 2:e329.

[Denk et al., 1990] Denk, W., Strickler, J. H., Webb, W. W., et al. (1990). Two-photon laser scanning fluorescence microscopy. *Science*, 248(4951):73–76.

[Desan, 1984] Desan, P. H. (1984). *The organization of the cerebral cortex of the pond turtle, Pseudemys scripta elegans*. PhD thesis, Harvard University.

[Desan, 1988] Desan, P. H. (1988). Organization of the cerebral cortex in turtle. In *The forebrain of reptiles*, pages 1–11. Karger Publishers.

[Douglas and Martin, 2007] Douglas, R. J. and Martin, K. A. (2007). Mapping the matrix: the ways of neocortex. *Neuron*, 56(2):226–238.

[Dugas-Ford and Ragsdale, 2015] Dugas-Ford, J. and Ragsdale, C. W. (2015). Levels of homology and the problem of neocortex. *Annual review of neuroscience*, 38:351–368.

[Dugas-Ford et al., 2012] Dugas-Ford, J., Rowell, J. J., and Ragsdale, C. W. (2012). Cell-type homologies and the origins of the neocortex. *Proceedings of the National Academy of Sciences*, 109(42):16974–16979.

[Eberle et al., 2015] Eberle, A., Mikula, S., Schalek, R., Lichtman, J., Tate, M. K., and Zeidler, D. (2015). High-resolution, high-throughput imaging with a multibeam scanning electron microscope. *Journal of microscopy*, 259(2):114–120.

[Edinger and Rand, 1908] Edinger, L. and Rand, H. W. (1908). The relations of comparative anatomy to comparative psychology. *Journal of Comparative Neurology*, 18(5):437–457.

[Ekstrand et al., 2001] Ekstrand, J. J., Domroese, M. E., Johnson, D. M., Feig, S. L., Knodel, S. M., Behan, M., and Haberly, L. B. (2001). A new subdivision of anterior piriform cortex and associated deep nucleus with novel features of interest for olfaction and epilepsy. *Journal of Comparative Neurology*, 434(3):289–307.

[Fournier et al., 2015] Fournier, J., Müller, C. M., and Laurent, G. (2015). Looking for the roots of cortical sensory computation in three-layered cortices. *Current opinion in neurobiology*, 31:119–126.

[Fournier et al., 2018] Fournier, J., Müller, C. M., Schneider, I., and Laurent, G. (2018). Spatial information in a non-retinotopic visual cortex. *Neuron*, 97(1):164–180.

[Freund and Buzsáki, 1996] Freund, T. F. and Buzsáki, G. (1996). Interneurons of the hippocampus. *Hippocampus*, 6(4):347–470.

[Frost et al., 1985] Frost, W. N., Castellucci, V. F., Hawkins, R. D., and Kandel, E. R. (1985). Monosynaptic connections made by the sensory neurons of the gill-and siphon-withdrawal reflex in aplysia participate in the storage of long-term memory for sensitization. *Proceedings of the National Academy of Sciences*, 82(23):8266–8269.

[Grillner, 2003] Grillner, S. (2003). The motor infrastructure: from ion channels to neuronal networks. *Nature Reviews Neuroscience*, 4(7):573.

[Grinvald et al., 1999] Grinvald, A., Shoham, D., Shmuel, A., Glaser, D., Vanzetta, I., Shtoyerman, E., Slovin, H., Wijnbergen, C., Hildesheim, R., and Arieli, A. (1999). In-vivo optical imaging of cortical architecture and dynamics. In *Modern techniques in neuroscience research*, pages 893–969. Springer.

[Grothe et al., 2010] Grothe, B., Pecka, M., and McAlpine, D. (2010). Mechanisms of sound localization in mammals. *Physiological reviews*, 90(3):983–1012.

[Haberly, 1983] Haberly, L. B. (1983). Structure of the piriform cortex of the opossum. i. description of neuron types with golgi methods. *Journal of Comparative Neurology*, 213(2):163–187.

[Haberly, 2001] Haberly, L. B. (2001). Parallel-distributed processing in olfactory cortex: new insights from morphological and physiological analysis of neuronal circuitry. *Chemical senses*, 26(5):551–576.

[Haberly and Bower, 1984] Haberly, L. B. and Bower, J. M. (1984). Analysis of association fiber system in piriform cortex with intracellular recording and staining techniques. *Journal of neurophysiology*, 51(1):90–112.

[Haberly and Bower, 1989] Haberly, L. B. and Bower, J. M. (1989). Olfactory cortex: model circuit for study of associative memory? *Trends in neurosciences*, 12(7):258–264.

[Haberly and Presto, 1986] Haberly, L. B. and Presto, S. (1986). Ultrastructural analysis of synaptic relationships of intracellularly stained pyramidal cell axons in piriform cortex. *Journal of Comparative Neurology*, 248(4):464–474.

[Haberly and Price, 1977] Haberly, L. B. and Price, J. L. (1977). The axonal projection patterns of the mitral and tufted cells of the olfactory bulb in the rat. *Brain research*, 129(1):152–157.

[Haberly and Price, 1978] Haberly, L. B. and Price, J. L. (1978). Association and commissural fiber systems of the olfactory cortex of the rat. i. systems originating in the piriform cortex and adjacent areas. *Journal of Comparative Neurology*, 178(4):711–740.

[Hagiwara et al., 2012] Hagiwara, A., Pal, S. K., Sato, T. F., Wienisch, M., and Murthy, V. N. (2012). Optophysiological analysis of associational circuits in the olfactory cortex. *Frontiers in neural circuits*, 6:18.

[Hagmann et al., 2010] Hagmann, P., Cammoun, L., Gigandet, X., Gerhard, S., Grant, P. E., Wedeen, V., Meuli, R., Thiran, J.-P., Honey, C. J., and Sporns, O. (2010). Mr connectomics: principles and challenges. *Journal of neuroscience methods*, 194(1):34–45.

[Hale, 2014] Hale, M. E. (2014). Mapping circuits beyond the models: integrating connectomics and comparative neuroscience. *Neuron*, 83(6):1256–1258.

[Hall et al., 2008] Hall, B. et al. (2008). *Strickberger's evolution*. Jones & Bartlett Learning.

[Hall and Ebner, 1970] Hall, W. C. and Ebner, F. F. (1970). Thalamotelencephalic projections in the turtle (pseudemys scripta). *Journal of Comparative Neurology*, 140(1):101–122.

[Hamlyn, 1961] Hamlyn, L. (1961). Electron microscopy of mossy fibre endings in ammon's horn. *Nature*, 190(4776):645.

[Hayworth et al., 2006a] Hayworth, K., Kasthuri, N., Schalek, R., and Lichtman, J. (2006a). Automating the collection of ultrathin serial sections for large volume tem reconstructions. *Microscopy and Microanalysis*, 12(S02):86.

[Hayworth et al., 2006b] Hayworth, K., Kasthuri, N., Schalek, R., and Lichtman, J. (2006b). Automating the collection of ultrathin serial sections for large volume tem reconstructions. *Microscopy and Microanalysis*, 12(S02):86.

[Hayworth et al., 2015] Hayworth, K. J., Xu, C. S., Lu, Z., Knott, G. W., Fetter, R. D., Tapia, J. C., Lichtman, J. W., and Hess, H. F. (2015). Ultrastructurally smooth

thick partitioning and volume stitching for large-scale connectomics. *Nature methods*, 12(4):319–322.

[Held, 2011] Held, H. (2011). *Die centrale gehörleitung*. Universitätsbibliothek Johann Christian Senckenberg.

[Hell and Wichmann, 1994] Hell, S. W. and Wichmann, J. (1994). Breaking the diffraction resolution limit by stimulated emission: stimulated-emission-depletion fluorescence microscopy. *Optics letters*, 19(11):780–782.

[Helmstaedter, 2013] Helmstaedter, M. (2013). Cellular-resolution connectomics: challenges of dense neural circuit reconstruction. *Nature methods*, 10(6):501.

[Helmstaedter et al., 2011] Helmstaedter, M., Briggman, K. L., and Denk, W. (2011). High-accuracy neurite reconstruction for high-throughput neuroanatomy. *Nature neuroscience*, 14(8):1081–1088.

[Helmstaedter et al., 2013] Helmstaedter, M., Briggman, K. L., Turaga, S. C., Jain, V., Seung, H. S., and Denk, W. (2013). Connectomic reconstruction of the inner plexiform layer in the mouse retina. *Nature*, 500(7461):168.

[Helmstaedter et al., 2008] Helmstaedter, M., Staiger, J. F., Sakmann, B., and Feldmeyer, D. (2008). Efficient recruitment of layer 2/3 interneurons by layer 4 input in single columns of rat somatosensory cortex. *Journal of Neuroscience*, 28(33):8273–8284.

[Herculano-Houzel, 2009] Herculano-Houzel, S. (2009). The human brain in numbers: a linearly scaled-up primate brain. *Frontiers in human neuroscience*, 3:31.

[Hildebrand and Shepherd, 1997] Hildebrand, J. G. and Shepherd, G. M. (1997). Mechanisms of olfactory discrimination: converging evidence for common principles across phyla. *Annual review of neuroscience*, 20(1):595–631.

[Hoogland et al., 1991] Hoogland, P., Wouterlood, F., Welker, E., and Van der Loos, H. (1991). Ultrastructure of giant and small thalamic terminals of cortical origin: a study of the projections from the barrel cortex in mice using phaseolus vulgaris leuco-agglutinin (pha-l). *Experimental brain research*, 87(1):159–172.

[Hua et al., 2015] Hua, Y., Laserstein, P., and Helmstaedter, M. (2015). Large-volume en-bloc staining for electron microscopy-based connectomics. *Nature communications*, 6:7923.

[Huang et al., 2013] Huang, S., Huganir, R. L., and Kirkwood, A. (2013). Adrenergic gating of hebbian spike-timing-dependent plasticity in cortical interneurons. *Journal of Neuroscience*, 33(32):13171–13178.

[Hubel and Wiesel, 1963] Hubel, D. H. and Wiesel, T. (1963). Shape and arrangement of columns in cat's striate cortex. *The Journal of physiology*, 165(3):559–568.

[Igarashi et al., 2012] Igarashi, K. M., Ieki, N., An, M., Yamaguchi, Y., Nagayama, S., Kobayakawa, K., Kobayakawa, R., Tanifuji, M., Sakano, H., Chen, W. R., et al. (2012). Parallel mitral and tufted cell pathways route distinct odor information to different targets in the olfactory cortex. *Journal of Neuroscience*, 32(23):7970–7985.

[Jain et al., 2010] Jain, V., Bollmann, B., Richardson, M., Berger, D. R., Helmstaedter, M. N., Briggman, K. L., Denk, W., Bowden, J. B., Mendenhall, J. M., Abraham, W. C., et al. (2010). Boundary learning by optimization with topological constraints. In *Computer Vision and Pattern Recognition (CVPR), 2010 IEEE Conference on*, pages 2488–2495. IEEE.

[Jarvis, 2009] Jarvis, E. D. (2009). *Evolution of the Pallium in Birds and Reptiles*, pages 1390–1400. Springer Berlin Heidelberg, Berlin, Heidelberg.

[Jeffress, 1948] Jeffress, L. A. (1948). A place theory of sound localization. *Journal of comparative and physiological psychology*, 41(1):35.

[Jiang et al., 2015] Jiang, X., Shen, S., Cadwell, C. R., Berens, P., Sinz, F., Ecker, A. S., Patel, S., and Tolias, A. S. (2015). Principles of connectivity among morphologically defined cell types in adult neocortex. *Science*, 350(6264):aac9462.

[Joesch et al., 2010] Joesch, M., Schnell, B., Raghu, S. V., Reiff, D. F., and Borst, A. (2010). On and off pathways in drosophila motion vision. *Nature*, 468(7321):300.

[Johnson and Leon, 2000] Johnson, B. A. and Leon, M. (2000). Odorant molecular length: one aspect of the olfactory code. *Journal of Comparative Neurology*, 426(2):330–338.

[Johnston, 1923] Johnston, J. (1923). Further contributions to the study of the evolution of the forebrain. v. survey of forebrain morphology. *Journal of Comparative Neurology*, 36(2):143–192.

[Johnston, 1915] Johnston, J. B. (1915). The cell masses in the forebrain of the turtle, cistudo carolina. *Journal of Comparative Neurology*, 25(5):393–468.

[Jones, 1984] Jones, E. G. (1984). Basket cells. *Cellular components of the cerebral cortex*, pages 309–336.

[Kaas, 1997] Kaas, J. H. (1997). Topographic maps are fundamental to sensory processing. *Brain research bulletin*, 44(2):107–112.

[Kappers, 1908] Kappers, C. (1908). Eversion and inversion of the dorso-lateral wall in different parts of the brain. *Journal of Comparative Neurology*, 18(4):433–436.

[Kasthuri et al., 2015] Kasthuri, N., Hayworth, K. J., Berger, D. R., Schalek, R. L., Conchello, J. A., Knowles-Barley, S., Lee, D., Vázquez-Reina, A., Kaynig, V., Jones,

T. R., et al. (2015). Saturated reconstruction of a volume of neocortex. *Cell*, 162(3):648–661.

[Kebschull et al., 2016] Kebschull, J. M., da Silva, P. G., Reid, A. P., Peikon, I. D., Albeanu, D. F., and Zador, A. M. (2016). High-throughput mapping of single-neuron projections by sequencing of barcoded rna. *Neuron*, 91(5):975–987.

[Klausberger and Somogyi, 2008] Klausberger, T. and Somogyi, P. (2008). Neuronal diversity and temporal dynamics: the unity of hippocampal circuit operations. *Science*, 321(5885):53–57.

[Knott et al., 2008] Knott, G., Marchman, H., Wall, D., and Lich, B. (2008). Serial section scanning electron microscopy of adult brain tissue using focused ion beam milling. *The Journal of neuroscience : the official journal of the Society for Neuroscience*, 28:2959–2964.

[Köppl and Carr, 2008] Köppl, C. and Carr, C. E. (2008). Maps of interaural time difference in the chicken's brainstem nucleus laminaris. *Biological cybernetics*, 98(6):541–559.

[Kornfeld et al., 2017] Kornfeld, J., Benezra, S. E., Narayanan, R. T., Svara, F., Egger, R., Oberlaender, M., Denk, W., and Long, M. A. (2017). Em connectomics reveals axonal target variation in a sequence-generating network. *Elife*, 6.

[Kosaka, 1980] Kosaka, T. (1980). The axon initial segment as a synaptic site: ultrastructure and synaptology of the initial segment of the pyramidal cell in the rat hippocampus (ca3 region). *Journal of neurocytology*, 9(6):861–882.

[Kriegstein and Connors, 1986] Kriegstein, A. R. and Connors, B. W. (1986). Cellular physiology of the turtle visual cortex: synaptic properties and intrinsic circuitry. *Journal of Neuroscience*, 6(1):178–191.

[Kristan and Katz, 2006] Kristan, W. B. and Katz, P. (2006). Form and function in systems neuroscience. *Current Biology*, 16(19):R828 – R831.

[Krogh, 1929] Krogh, A. (1929). The progress of physiology. *American Journal of Physiology–Legacy Content*, 90(2):243–251.

[Landers et al., 2011] Landers, M., Knott, G., Lipp, H., Poletaeva, I., and Welker, E. (2011). Synapse formation in adult barrel cortex following naturalistic environmental enrichment. *Neuroscience*, 199:143 – 152.

[Larkum, 2013] Larkum, M. (2013). A cellular mechanism for cortical associations: an organizing principle for the cerebral cortex. *Trends in neurosciences*, 36(3):141–151.

[Larkum et al., 2008] Larkum, M. E., Watanabe, S., Lasser-Ross, N., Rhodes, P., and Ross, W. N. (2008). Dendritic properties of turtle pyramidal neurons. *Journal of neurophysiology*, 99(2):683–694.

[Li et al., 2008] Li, C., Wu, X.-C., Rieppel, O., Wang, L.-T., and Zhao, L.-J. (2008). An ancestral turtle from the late triassic of southwestern china. *Nature*, 456(7221):497.

[Lipson, 1998] Lipson, S. (1998). H. lipson nd ds tannhauser, optical physics.

[Litaudon et al., 2003] Litaudon, P., Amat, C., Bertrand, B., Vigouroux, M., and Buonviso, N. (2003). Piriform cortex functional heterogeneity revealed by cellular responses to odours. *European Journal of Neuroscience*, 17(11):2457–2461.

[Maccaferri et al., 1998] Maccaferri, G., Tóth, K., and McBain, C. J. (1998). Target-specific expression of presynaptic mossy fiber plasticity. *Science*, 279(5355):1368–1371.

[Mancilla et al., 1998] Mancilla, J. G., Fowler, M., and Ulinski, P. S. (1998). Responses of regular spiking and fast spiking cells in turtle visual cortex to light flashes. *Visual neuroscience*, 15(5):979–993.

[Marder and Bucher, 2007] Marder, E. and Bucher, D. (2007). Understanding circuit dynamics using the stomatogastric nervous system of lobsters and crabs. *Annu. Rev. Physiol.*, 69:291–316.

[Marin-Padilla, 1971] Marin-Padilla, M. (1971). Early prenatal ontogenesis of the cerebral cortex (neocortex) of the cat (felis domestica). a golgi study. *Zeitschrift für Anatomie und Entwicklungsgeschichte*, 134(2):117–145.

[Marr, 1982] Marr, D. (1982). *Vision: A Computational Investigation Into.* WH Freeman.

[Masu et al., 1995] Masu, M., Iwakabe, H., Tagawa, Y., Miyoshi, T., Yamashita, M., Fukuda, Y., Sasaki, H., Hiroi, K., Nakamura, Y., Shigemoto, R., et al. (1995). Specific deficit of the on response in visual transmission by targeted disruption of the mgiur6 gene. *Cell*, 80(5):757–765.

[McAlpine and Grothe, 2003] McAlpine, D. and Grothe, B. (2003). Sound localization and delay lines–do mammals fit the model? *Trends in neurosciences*, 26(7):347–350.

[McGill et al., 1978] McGill, R., Tukey, J. W., and Larsen, W. A. (1978). Variations of box plots. *The American Statistician*, 32(1):12–16.

[Megıas et al., 2001] Megıas, M., Emri, Z., Freund, T., and Gulyas, A. (2001). Total number and distribution of inhibitory and excitatory synapses on hippocampal ca1 pyramidal cells. *Neuroscience*, 102(3):527–540.

[Métin et al., 2007] Métin, C., Alvarez, C., Moudoux, D., Vitalis, T., Pieau, C., and Molnár, Z. (2007). Conserved pattern of tangential neuronal migration during forebrain development. *Development*, 134(15):2815–2827.

[Mikula, 2016] Mikula, S. (2016). Progress towards mammalian whole-brain cellular connectomics. *Frontiers in neuroanatomy*, 10.

[Molowny et al., 1972] Molowny, A., Lopez, C., and Marin, F. (1972). Cytoarchitectonic study of the cerebral cortex in reptiles. i. areas and cortical nucleus in lacerta galloti, chalcides viridanus and tarentola mauritanica. *Trabajos del Instituto Cajal de investigaciones biologicas*, 64:125.

[Morgan et al., 2016] Morgan, J. L., Berger, D. R., Wetzel, A. W., and Lichtman, J. W. (2016). The fuzzy logic of network connectivity in mouse visual thalamus. *Cell*, 165(1):192–206.

[Mountcastle, 1978] Mountcastle, V. (1978). An organizing principle for cerebral function: the unit module and the distributed system. *The mindful brain*.

[Naumann and Laurent, 2017] Naumann, R. and Laurent, G. (2017). Function and evolution of the reptilian cerebral cortex.

[Naumann et al., 2015] Naumann, R. K., Ondracek, J. M., Reiter, S., Shein-Idelson, M., Tosches, M. A., Yamawaki, T. M., and Laurent, G. (2015). The reptilian brain. *Current Biology*, 25(8):R317.

[Nelson, 1970] Nelson, G. J. (1970). Outline of a theory of comparative biology. *Systematic Zoology*, 19(4):373–384.

[Northcutt, 1981] Northcutt, R. G. (1981). Evolution of the telencephalon in nonmammals. *Annual review of neuroscience*, 4(1):301–350.

[Osten and Margrie, 2013] Osten, P. and Margrie, T. W. (2013). Mapping brain circuitry with a light microscope. *Nature methods*, 10(6):515.

[Paxinos and Franklin, 2008] Paxinos, G. and Franklin, K. (2008). *The Mouse Brain in Stereotaxic Coordinates*. Elsevier Academic Press.

[Peikon et al., 2014] Peikon, I. D., Gizatullina, D. I., and Zador, A. M. (2014). In vivo generation of dna sequence diversity for cellular barcoding. *Nucleic acids research*, 42(16):e127–e127.

[Peters and Feldman, 1976] Peters, A. and Feldman, M. L. (1976). The projection of the lateral geniculate nucleus to area 17 of the rat cerebral cortex. i. general description. *Journal of neurocytology*, 5(1):63–84.

[Peters et al., 1983] Peters, A., Miller, M., and Kimerer, L. (1983). Cholecystokinin-like immunoreactive neurons in rat cerebral cortex. *Neuroscience*, 8(3):431–448.

[Peters and Payne, 1993] Peters, A. and Payne, B. R. (1993). Numerical relationships between geniculocortical afferents and pyramidal cell modules in cat primary visual cortex. *Cerebral Cortex*, 3(1):69–78.

[Peters et al., 1968] Peters, A., Proskauer, C. C., and Kaiserman-Abramof, I. R. (1968). The small pyramidal neuron of the rat cerebral cortex: the axon hillock and initial segment. *The Journal of cell biology*, 39(3):604–619.

[Poo and Isaacson, 2009] Poo, C. and Isaacson, J. S. (2009). Odor representations in olfactory cortex:"sparse" coding, global inhibition, and oscillations. *Neuron*, 62(6):850–861.

[Poo and Isaacson, 2011] Poo, C. and Isaacson, J. S. (2011). A major role for intracortical circuits in the strength and tuning of odor-evoked excitation in olfactory cortex. *Neuron*, 72(1):41–48.

[Puelles et al., 2013] Puelles, L., Harrison, M., Paxinos, G., and Watson, C. (2013). A developmental ontology for the mammalian brain based on the prosomeric model. *Trends in neurosciences*, 36(10):570–578.

[Puelles et al., 2000] Puelles, L., Kuwana, E., Puelles, E., Bulfone, A., Shimamura, K., Keleher, J., Smiga, S., and Rubenstein, J. L. (2000). Pallial and subpallial derivatives in the embryonic chick and mouse telencephalon, traced by the expression of the genes dlx-2, emx-1, nkx-2.1, pax-6, and tbr-1. *Journal of Comparative Neurology*, 424(3):409–438.

[Ragan et al., 2012] Ragan, T., Kadiri, L. R., Venkataraju, K. U., Bahlmann, K., Sutin, J., Taranda, J., Arganda-Carreras, I., Kim, Y., Seung, H. S., and Osten, P. (2012). Serial two-photon tomography for automated ex vivo mouse brain imaging. *Nature methods*, 9(3):255.

[Ramón y Cajal, 1952] Ramón y Cajal, S. (1952). 1909–1911 histologie du système nerveux de l'homme et des vertébrés. *Maloine, Paris*, 2:862–867.

[Rees et al., 2017] Rees, C. L., Moradi, K., and Ascoli, G. A. (2017). Weighing the evidence in peters' rule: does neuronal morphology predict connectivity? *Trends in neurosciences*, 40(2):63–71.

[Regidor and Poch, 1988] Regidor, J. and Poch, L. (1988). Histochemical analysis of the lizard cortex: an acetylcholinesterase, cytochrome oxidase and nadph-diaphorase study. In *The Forebrain of Reptiles*, pages 77–84. Karger Publishers.

[Reid and Alonso, 1995] Reid, R. C. and Alonso, J.-M. (1995). Specificity of monosynaptic connections from thalamus to visual cortex. *Nature*, 378(6554):281.

[Reiner, 1991] Reiner, A. (1991). A comparison of neurotransmitter-specific and neuropeptide-specific neuronal cell types present in the dorsal cortex in turtles with

those present in the isocortex in mammals: Implications for the evolution of isocortex; pp. 73–82. *Brain, behavior and evolution*, 38(2-3):73–82.

[Reiner, 1993] Reiner, A. (1993). Neurotransmitter organization and connections of turtle cortex: implications for the evolution of mammalian isocortex. *Comparative Biochemistry and Physiology Part A: Physiology*, 104(4):735–748.

[Reiner and Beinfeld, 1985] Reiner, A. and Beinfeld, M. C. (1985). The distribution of cholecystokinin-8 in the central nervous system of turtles: an immunohistochemical and biochemical study. *Brain research bulletin*, 15(2):167–181.

[Reiner et al., 2004] Reiner, A., Perkel, D. J., Bruce, L. L., Butler, A. B., Csillag, A., Kuenzel, W., Medina, L., Paxinos, G., Shimizu, T., Striedter, G., et al. (2004). Revised nomenclature for avian telencephalon and some related brainstem nuclei. *Journal of Comparative Neurology*, 473(3):377–414.

[Rockland and Pandya, 1979] Rockland, K. S. and Pandya, D. N. (1979). Laminar origins and terminations of cortical connections of the occipital lobe in the rhesus monkey. *Brain research*, 179(1):3–20.

[Rollenhagen et al., 2007] Rollenhagen, A., Sätzler, K., Rodríguez, E. P., Jonas, P., Frotscher, M., and Lübke, J. H. (2007). Structural determinants of transmission at large hippocampal mossy fiber synapses. *Journal of Neuroscience*, 27(39):10434–10444.

[Rust et al., 2006] Rust, M. J., Bates, M., and Zhuang, X. (2006). Sub-diffraction-limit imaging by stochastic optical reconstruction microscopy (storm). *Nature methods*, 3(10):793.

[Ryugo et al., 2006] Ryugo, D., Montey, K., Wright, A., Bennett, M., and Pongstaporn, T. (2006). Postnatal development of a large auditory nerve terminal: the endbulb of held in cats. *Hearing research*, 216:100–115.

[Sanides and Sanides, 1972] Sanides, F. and Sanides, D. (1972). The "extraverted neurons" of the mammalian cerebral cortex. *Anatomy and Embryology*, 136(3):272–293.

[Sarma et al., 2011] Sarma, A. A., Richard, M. B., and Greer, C. A. (2011). Developmental dynamics of piriform cortex. *Cerebral Cortex*, 21(6):1231–1245.

[Schalek et al., 2011] Schalek, R., Kasthuri, N., Hayworth, K., Berger, D., Tapia, J., Morgan, J., Turaga, S., Fagerholm, E., Seung, H., and Lichtman, J. (2011). Development of high-throughput, high-resolution 3d reconstruction of large-volume biological tissue using automated tape collection ultramicrotomy and scanning electron microscopy. *Microscopy and Microanalysis*, 17(S2):966.

[Schmidt et al., 2017] Schmidt, H., Gour, A., Straehle, J., Boergens, K. M., Brecht, M., and Helmstaedter, M. (2017). Axonal synapse sorting in medial entorhinal cortex. *Nature*, advance online publication.

[Shapley and Xing, 2013] Shapley, R. M. and Xing, D. (2013). Local circuit inhibition in the cerebral cortex as the source of gain control and untuned suppression. *Neural Networks*, 37:172–181.

[Shepherd, 2011] Shepherd, G. M. (2011). The microcircuit concept applied to cortical evolution: from three-layer to six-layer cortex. *Frontiers in neuroanatomy*, 5:30.

[Shepherd and Svoboda, 2005] Shepherd, G. M. and Svoboda, K. (2005). Laminar and columnar organization of ascending excitatory projections to layer 2/3 pyramidal neurons in rat barrel cortex. *Journal of Neuroscience*, 25(24):5670–5679.

[Shipley and Ennis, 1996] Shipley, M. T. and Ennis, M. (1996). Functional organization of olfactory system. *Developmental Neurobiology*, 30(1):123–176.

[Skeen et al., 1984] Skeen, L., Pindzola, R., and Schofield, B. (1984). Tangential organization of olfactory, association, and commissural projections to olfactory cortex in a species of reptile (trionyx spiniferus), bird (aix sponsa), and mammal (tupaia glis). *Brain, behavior and evolution*, 25(4):206—216.

[Smith et al., 1980] Smith, L. M., Ebner, F. F., and Colonnier, M. (1980). The thalamocortical projection in pseudemys turtles: a quantitative electron microscopic study. *Journal of Comparative Neurology*, 190(3):445–461.

[Somogyi, 1977] Somogyi, P. (1977). A specific 'axo-axonal'interneuron in the visual cortex of the rat. *Brain research*, 136(2):345–350.

[Somogyi et al., 1982] Somogyi, P., Freund, T., and Cowey, A. (1982). The axo-axonic interneuron in the cerebral cortex of the rat, cat and monkey. *Neuroscience*, 7(11):2577–2607.

[Somogyi et al., 1983] Somogyi, P., Kisvarday, Z., Martin, K., and Whitteridge, D. (1983). Synaptic connections of morphologically identified and physiologically characterized large basket cells in the striate cortex of cat. *Neuroscience*, 10(2):261–294.

[Sosulski et al., 2011] Sosulski, D. L., Bloom, M. L., Cutforth, T., Axel, R., and Datta, S. R. (2011). Distinct representations of olfactory information in different cortical centres. *Nature*, 472(7342):213.

[Spacek and Harris, 2004] Spacek, J. and Harris, K. M. (2004). Trans-endocytosis via spinules in adult rat hippocampus. *Journal of Neuroscience*, 24(17):4233–4241.

[Spacek and Lieberman, 1974] Spacek, J. and Lieberman, A. (1974). Ultrastructure and three-dimensional organization of synaptic glomeruli in rat somatosensory thalamus. *Journal of anatomy*, 117(Pt 3):487.

[Sporns et al., 2005] Sporns, O., Tononi, G., and Kötter, R. (2005). The human connectome: a structural description of the human brain. *PLoS computational biology*, 1(4):e42.

[Staffler et al., 2017] Staffler, B., Berning, M., Boergens, K. M., Gour, A., van der Smagt, P., and Helmstaedter, M. (2017). SynEM: Automated synapse detection for connectomics. *eLife*, 6:e26414.

[Stettler and Axel, 2009] Stettler, D. D. and Axel, R. (2009). Representations of odor in the piriform cortex. *Neuron*, 63(6):854–864.

[Stokes and Isaacson, 2010] Stokes, C. C. and Isaacson, J. S. (2010). From dendrite to soma: dynamic routing of inhibition by complementary interneuron microcircuits in olfactory cortex. *Neuron*, 67(3):452–465.

[Striedter, 2006] Striedter, G. F. (2006). Précis of principles of brain evolution. *Behavioral and Brain Sciences*, 29(1):1–12.

[Striedter, 2016] Striedter, G. F. (2016). Evolution of the hippocampus in reptiles and birds. *Journal of Comparative Neurology*, 524(3):496–517.

[Suárez et al., 2006] Suárez, J., Dávila, J. C., Real, M. á., Guirado, S., and Medina, L. (2006). Calcium-binding proteins, neuronal nitric oxide synthase, and gaba help to distinguish different pallial areas in the developing and adult chicken. i. hippocampal formation and hyperpallium. *Journal of Comparative Neurology*, 497(5):751–771.

[Suzuki and Bekkers, 2007] Suzuki, N. and Bekkers, J. M. (2007). Inhibitory interneurons in the piriform cortex. *Clinical and Experimental Pharmacology and Physiology*, 34(10):1064–1069.

[Suzuki and Bekkers, 2012] Suzuki, N. and Bekkers, J. M. (2012). Microcircuits mediating feedforward and feedback synaptic inhibition in the piriform cortex. *Journal of Neuroscience*, 32(3):919–931.

[Szentágothai, 1973] Szentágothai, J. (1973). Synaptology of the visual cortex. In *Visual Centers in the Brain*, pages 269–324. Springer.

[Takemura et al., 2013] Takemura, S.-y., Bharioke, A., Lu, Z., Nern, A., Vitaladevuni, S., Rivlin, P. K., Katz, W. T., Olbris, D. J., Plaza, S. M., Winston, P., Zhao, T., Horne, J. A., Fetter, R. D., Takemura, S., Blazek, K., Chang, L.-A., Ogundeyi, O., Saunders, M. A., Shapiro, V., Sigmund, C., Rubin, G. M., Scheffer, L. K., Meinertzhagen, I. A., and Chklovskii, D. B. (2013). A visual motion detection circuit suggested by drosophila connectomics. *Nature*, 500:175–181.

[Titze and Denk, 2013] Titze, B. and Denk, W. (2013). Automated in-chamber specimen coating for serial block-face electron microscopy. *Journal of microscopy*, 250(2):101–110.

[Tollis et al., 2015] Tollis, M., Hutchins, E. D., and Kusumi, K. (2015). Reptile genomes open the frontier for comparative analysis of amniote development and regeneration. *International Journal of Developmental Biology*, 58(10-11-12):863–871.

[Turaga et al., 2010] Turaga, S. C., Murray, J. F., Jain, V., Roth, F., Helmstaedter, M., Briggman, K., Denk, W., and Seung, H. S. (2010). Convolutional networks can learn to generate affinity graphs for image segmentation. *Neural computation*, 22(2):511–538.

[Ulinski, 1990] Ulinski, P. S. (1990). The cerebral cortex of reptiles. In *Comparative Structure and Evolution of Cerebral Cortex, Part I*, pages 139–215. Springer.

[Ulinski and Nautiyal, 1988] Ulinski, P. S. and Nautiyal, J. (1988). Organization of retinogeniculate projections in turtles of the genera pseudemys and chrysemys. *Journal of Comparative Neurology*, 276(1):92–112.

[Varshney et al., 2011] Varshney, L. R., Chen, B. L., Paniagua, E., Hall, D. H., and Chklovskii, D. B. (2011). Structural properties of the caenorhabditis elegans neuronal network. *PLoS computational biology*, 7(2):e1001066.

[Wang et al., 2004] Wang, Y., Toledo-Rodriguez, M., Gupta, A., Wu, C., Silberberg, G., Luo, J., and Markram, H. (2004). Anatomical, physiological and molecular properties of martinotti cells in the somatosensory cortex of the juvenile rat. *The Journal of physiology*, 561(1):65–90.

[Westrum and Blackstad, 1962] Westrum, L. E. and Blackstad, T. W. (1962). An electron microscopic study of the stratum radiatum of the rat hippocampus (regio superior, ca 1) with particular emphasis on synaptology. *Journal of Comparative Neurology*, 119(3):281–309.

[White and Hersch, 1982] White, E. L. and Hersch, S. M. (1982). A quantitative study of thalamocortical and other synapses involving the apical dendrites of corticothalamic projection cells in mouse smi cortex. *Journal of neurocytology*, 11(1):137–157.

[White and Keller, 1987] White, E. L. and Keller, A. (1987). Intrinsic circuitry involving the local axon collaterals of corticothalamic projection cells in mouse smi cortex. *Journal of Comparative Neurology*, 262(1):13–26.

[White and Peters, 1993] White, E. L. and Peters, A. (1993). Cortical modules in the posteromedial barrel subfield (sml) of the mouse. *Journal of Comparative Neurology*, 334(1):86–96.

[White et al., 1986] White, J. G., Southgate, E., Thomson, J. N., and Brenner, S. (1986). The structure of the nervous system of the nematode caenorhabditis elegans. *Philosophical transactions of the Royal Society of London. Series B, Biological sciences*, 314:1–340.

[Wilson and Sullivan, 2011] Wilson, D. A. and Sullivan, R. M. (2011). Cortical processing of odor objects. *Neuron*, 72(4):506–519.

[Zheng et al., 2017] Zheng, Z., Lauritzen, J. S., Perlman, E., Robinson, C. G., Nichols, M., Milkie, D., Torrens, O., Price, J., Fisher, C. B., Sharifi, N., et al. (2017). A complete electron microscopy volume of the brain of adult drosophila melanogaster. *bioRxiv*, page 140905.

7 Acknowledgements

Zuallererst möchte ich meiner Mutter Annette Bastians für ihre Unterstützung in allen Lebenslagen danken, die wesentlich zu meinem bisherigen Lebensweg beigetragen hat! Sie war immer für mich da und stand mit Rat und Tat bereit, wann immer es nötig war.

I am feeling very grateful to many people who played a role in the completion of this thesis:

First and foremost, I want to thank Prof. Dr. Moritz Helmstaedter for his patience, constant support and guidance throughout the course of my PhD and for the opportunity to work in a great atmosphere. He has been the driving influence throughout the project and was the major motivating factor and coordinator of this work presented here.

Furthermore, this work would not have been possible without an intense collaboration with Kevin Börgens who welcomed me in the lab, taught and showed me all the little invaluable tricks for the methods used in this work. He also became a good friend and was supporting me in various ways during the whole project.

Special thanks to Philip Laserstein who supported me throughout the lab work and gave me very helpful feedback on this manuscript. He also became a good friend, a fast running buddy and he was supporting me in all difficult times during the whole project.

I want to thank the members of my thesis committee, Prof. Gilles Laurent and Prof. Dr. Ilona Grunwald Kadow for good discussions and great suggestions during the TAC meetings, helping to drive the project to the right direction.

I want to thank Benjamin Kachel for his incredible friendship, his uplifting motivational talks and his very helpful feedback to this manuscript.

I want to thank Fabian Isensee for his warm friendship, his support during difficult times and his feedback to this manuscript.

I want to thank Manuel Berning for his warm welcome in the lab, the many great discussions and the help in all questions related to the computational part of this work which is a strong understatement. He also became a good friend and we spent a lot of exciting moments during the project.

I want to thank Jakob Strähle for being a good friend, great discussions and the feedback on this manuscript.

I want to thank Anjali Gour for all the fruitful discussion and the insights to her project.

I want to thank Benedikt Staffler for his very helpful feedback on this manuscript.

All other members in the lab I want to thank whole heartily for generating a nice atmosphere and interesting scientific environment.

Ich danke Wolfgang Bastians für alle Unterstützung, die ich von ihm erfahren habe in allen schweren Zeiten. Ebenso danke ich ihm für alle tollen Momente, die wir bereits gemeinsam hatten.

Ich bedanke mich bei meiner gesamten Familie, die mich stets unterstützt und mich auf meinem Lebensweg begleitet hat.

Außerdem möchte ich mich bei all meinen Freunden bedanken: Manuel Schmelzle, Timo Eipperle, Oliver Kern, Pascal Gieß, Katharina Haase, Liesa-Marie Schreiber, Kira Gabe, Bianca Paulus, die mich auf den verschiedenen Abschnitten meines Lebens begleitet, unterstützt und geprägt haben.

8 List of author contributions

Philipp Alexander Bastians generated all data and prepared all figures if not stated otherwise.

Heiko Wissler (Department of Connectomics, Max Planck Institute for Brain Research, Frankfurt, Germany) generated the data visualization in Figure 4.1B, Figure 4.2B, Figure 4.3, Figure 4.4, Figure 4.6, Figure 4.7, and Figure 4.18.

Manuela Klinkmann (Department of Neural Systems, Max Planck Institute for Brain Research, Frankfurt, Germany) perfused the animal used for SBEM data acquistion of turtle dorsal cortex L3.

Dr. Silke Haverkamp (Max Planck Institute for Brain Research, Frankfurt, Germany) kindly provided the TEM data for Figure 4.21 and Figure 4.23.

Catharina Schilt and **Gongsun Nam** (Max Planck Institute for Brain Research, Frankfurt, Germany) prepared, stained the turtle cortex tissue and acquired the TEM data shown in Figure 4.21 and Figure 4.23.

Stephan Junek (Max Planck Institute for Brain Research, Frankfurt, Germany) post-processed the acquired TEM data shown in Figure 4.21 and Figure 4.23.

Christian Müller (Department of Neural Systems, Max Planck Institute for Brain Research, Frankfurt, Germany) perfused the animal used for TEM data acquisition shown in Figure 4.21 and Figure 4.23.

A. Brandt, **M. Nonnenbroich**, **L. Bezzenberger**, and **R. Hülse** (Department of Connectomics, Max Planck Institute for Brain Research, Frankfurt, Germany) volume reconstructed the neurons, dendrites and axons shown in Figure 4.3, Figure 4.6, and Figure 4.7B.

9 List of Publications

Conferences

2017	Munich Winter Conference on Stress, 19.-21.03.2017 Garmisch-Partenkirchen, Germany **Connectomics of Three-Layered Reptilian and Mammalian Cortices**
2017	Connectomics Conference, 9.-12.04.2016 Berlin, Germany **Comparative Analysis of Local Circuits in Three-Layered Sensory Cortices**
2016	Society for Neuroscience Conference, 12.-16.11.2016 San Diego, United States **Comparative Analysis of Local Circuits in Six- and Three-Layered Sensory Cortices**
2016	High-Resolution Circuit Reconstruction Conference, 10.-13.04.2016 Janelia Research Campus, United States (abstract rejected) **Connectomics of Three-Layered Reptilian and Mammalian Cortices Cortices**
2014	Society for Neuroscience Conference, 15.-19.11.2014 Washington DC, United States **Comparative Analysis of Local Circuits in Six- and Three-Layered Sensory Cortices**

2014 | Connectomics Conference, 7.-10.09.2014

Berlin, Germany

Comparative Analysis of Local Circuits in Six- and Three-Layered Sensory Cortices